

NOVEL INFRARED LASER TISSUE FUSION LAPAROSCOPIC DEVICE DESIGNS
USING TRANSPARENT MATERIALS AND REAL-TIME OPTICAL FEEDBACK

by

Woheeb Muhammad Saeed

A dissertation submitted to the faculty of
The University of North Carolina at Charlotte
in partial fulfillment of the requirements
for the degree of Doctor of Philosophy in
Optical Science and Engineering

Charlotte

2024

Approved by:

Dr. Nathaniel Fried

Dr. Tino Hofmann

Dr. Yasin Raja

Dr. Didier Dreau

ABSTRACT

WOHEEB MUHAMMAD SAEED. Novel Infrared Laser Tissue Fusion Laparoscopic Device Designs using Transparent Materials and Real-time Optical Feedback.
(Under the direction of DR. NATHANIEL M. FRIED)

Conventional suture ligation of vascular tissues during surgery is time consuming and skill intensive. Alternative techniques require hemostasis through mechanical clips or sutures, which leave foreign objects in the body and disrupt the procedure through the need to exchange instruments. In recent years, energy-based devices, such as ultrasonic (US) and radiofrequency (RF) electrosurgical based technologies, have been used for rapid and efficient blood vessel ligation. These devices expedite numerous labor-intensive surgical procedures (including lobectomy, nephrectomy, gastric bypass, splenectomy, thyroidectomy, hysterectomy, and colectomy). However, both US and RF devices have limitations, including potential for unacceptably large collateral thermal damage zones, with thermal spread averaging greater than 1 mm. This lack of specificity prevents the use of these devices for delicate surgical procedures performed in confined spaces (such as prostatectomy). These device jaws take a long time to cool down to normal body temperature between successive procedures and may also cause thermal damage to healthy tissue through unintended heat conduction from contact with the device jaws.

A novel alternative method using near-infrared (IR) lasers for vessel ligation may eliminate some of these limitations of conventional energy-based devices. In this study, two real-time optical feedback systems are explored along with transparent jaw designs for sealing and bisection of blood vessels. This thesis begins with an introduction and theory of tissue optics followed by the methods used for the study. Chapter four describes the use of tissue autofluorescence as a real-time optical feedback system. The fifth chapter details the testing and comparison, both

experimentally and computationally, of quartz and sapphire optical materials. These materials are transparent and bio-compatible, intended for use in the optical chamber, a critical component of the laparoscopic device jaw. Chapter 6 describes a simultaneous IR laser vessel sealing and bisection study using a quartz optical chamber suitable for integration into a laparoscopic device, and the feasibility of using the optical signal originating from the therapeutic laser and transmitted through the cut vessel, as a closed-loop, optical feedback system for immediately deactivating the IR laser upon successful vessel bisection. Chapter 7 outlines the future work. Chapter 8 summarizes the main accomplishments of this thesis.

ACKNOWLEDGEMENT

I would like to extend my heartfelt thanks to the undergraduate students in the lab, Patrick J. O'Brien, Aiden R. Restelli, Jude K. Yoshino, and Alexandria J. Traynham, for their invaluable help and support throughout this research project. Their dedication, hard work, and enthusiasm have been instrumental in the success of this work. I am also grateful to Dr. Tsing-Hua Her for generously allowing me to borrow their lab spectrometer, which was essential for conducting the experiments. I would like to express my gratitude to my fellow Ph.D. candidate, Mahfuja A. Khuda, for her invaluable insights during the simulations. Additionally, I would like to express my gratitude to the National Institute of Biomedical Imaging and Bioengineering of the National Institutes of Health, under Grant R15EB028576, for their financial support, which made this research possible. Their support has been instrumental in the completion of this project, and I am truly thankful for their contribution.

DEDICATION

To my beloved parents, Father: Muhammad Saeed and Mother: Saadat Saeed, your unwavering love, encouragement, and sacrifices have been the foundation of my journey. Your belief in me has fueled my determination, and your guidance has shaped my character. This thesis is a testament to your endless support and the values you have instilled in me. I also dedicate this work to my supervisor, Professor Dr. Nathaniel Fried, whose expertise, guidance, and mentorship have been invaluable throughout this journey. Your dedication to excellence and passion for research have inspired me to push the boundaries of knowledge. I am grateful for your unwavering support and belief in my abilities. This thesis is dedicated to you, with heartfelt gratitude and appreciation for all that you have done. Thank you.

TABLE OF CONTENTS

LIST OF TABLES	xi
LIST OF FIGURES	xii
Chapter 1 : INTRODUCTION.....	1
Chapter 2 : THEORY.....	5
2.1: Optical properties of soft tissues.....	5
2.2 Dynamic optical properties of tissue response.....	9
2.2.1 The effects of spot size variation on optical penetration depth	9
2.2.2 Dynamic tissue responses to temperature	9
2.2.3 Dynamic tissue responses to compression.....	10
Chapter 3 : METHODS	12
3.1 Anatomy of a vascular system and blood vessels.....	12
3.2 Tissue dissection	13
3.3 Burst pressure readings	13
Chapter 4 : A REAL-TIME FLUORESCENCE FEEDBACK SYSTEM FOR INFRARED LASER SEALING OF BLOOD VESSELS	16
4.1 Introduction.....	16
4.2 Methods.....	17
4.3 Results.....	20
4.3.1 System calibration.....	20

4.3.2 Non-real-time measurements	22
4.3.3 Real-time measurements	25
4.4 Discussion	28
4.5 Conclusion	33
 Chapter 5 : COMPARISON OF QUARTZ AND SAPPHIRE OPTICAL CHAMBERS FOR INFRARED LASER SEALING OF VASCULAR TISSUES USING A RECIPROCATING, SIDE-FIRING OPTICAL FIBER: SIMULATIONS AND EXPERIMENTS	
5.1 Introduction.....	34
5.2 Experimental Methods	35
5.2.1 Fiber angle polishing.....	36
5.2.2 Bottom jaw assembly	36
5.2.3 Optical beam characterization (razor blade scans and infrared beam profiler)	37
5.2.4 Reciprocating fiber experimental setup	38
5.2.5 Temperature measurements	39
5.2.7 Statistical analysis	40
5.3 Computational methods	40
5.3.1 Optical simulations	40
5.3.2 Thermal simulations.....	41
5.4 Experimental results.....	42
5.4.1 Optical characterization of side-firing fiber.....	42

5.4.2 Thermal characterization of quartz and sapphire chambers	44
5.4.3 Vessel burst pressures	46
5.5 Computational results	50
5.5.1 Optical simulations	50
5.5.2 Thermal simulations.....	51
5.6 Discussion	56
5.7 Conclusion	59
Chapter 6 : SIMULTANEOUS SEALING AND BISECTION OF PORCINE RENAL	
BLOOD VESSELS, <i>EX VIVO</i> , USING A CONTINUOUS-WAVE, INFRARED DIODE	
LASER AT 1470 NM	60
6.1 Introduction.....	60
6.2 Methods.....	60
6.2.1 Simultaneous vessel sealing and bisection studies	60
6.2.2 Optical feedback system	64
6.3 Results.....	65
6.3.1 Total fluence	65
6.3.2 Burst pressure (BP) measurements	66
6.3.3 Thermal characterization of quartz jaw	68
6.3.4 Optical Transmission Signal during Blood Vessel Ablation	68
6.4 Discussion	69

6.4.1 Vessel sealing and bisection studies	69
6.4.2 Optical signal transmission studies.....	72
6.5 Conclusion	73
Chapter 7 : FUTURE WORK.....	74
7.1 Closed loop feedback and prototype design	74
7.2 Jaw cooling	75
7.3 Optical indicator for collagen-elastin content and its relation to burst pressure strength...	76
Chapter 8 : CONCLUSION	79
REFERENCES	81
APPENDIX A : PEER REVIEWED JOURNAL ARTICLES.....	92
APPENDIX B : PEER REVIEWED CONFERENCE PROCEEDINGS.....	93

LIST OF TABLES

Table 1.1: Comparison of commercial and experimental vessel sealing and cutting techniques [24-31].....	4
Table 4.1: Increase in integrated fluorescence signal in 470-520 nm spectrum for successful and failed vessel seals	24
Table 4.2: Comparison of diffuse transmission and fluorescence optical feedback methods for IR laser vessel sealing.	32
Table 5.1: Thermocouple (TC) temperatures (°C) measured on the quartz (Q) and sapphire (S) chamber internal and external surfaces, for fixed laser parameters of 30 W for 5 s, as well as times necessary for the jaw to cool down to body temperature between applications	45
Table 5.2: Statistical comparison of results for quartz and sapphire optical chambers, with laser incident power at the tissue surface of 30 W and irradiation time of 5 s. Statistical significance between quartz and sapphire is denoted by an asterisk (*).....	48
Table 5.3: Statistical comparison of results for quartz and sapphire optical chambers, with laser incident power at the tissue surface of 30 W and irradiation time of 5 s. Statistical significance between quartz and sapphire is denoted by an asterisk (*).....	56
Table 6.1: Burst pressures (BP) of both bisected segments (S1/S2) of blood vessels for each incident power and irradiation time.....	67

LIST OF FIGURES

Figure 1.1: Prototype device with traditional 5-mm-OD Maryland style laparoscopic jaws.

Insert shows magnified view of upper and lower jaws on laparoscopic device. A thermal camera was used for temperature mapping3

Figure 2.1: Optical absorption coefficients of soft tissue components: 0.1-10 μm spectrum

[35]7

Figure 2.2: Overlapping scattering effects and the forward propagation of a larger beam

spot leading to a deeper OPD [34]10

Figure 3.1: The structure of an arteriole vessel (not drawn to scale).....13

Figure 3.2: Porcine kidney and branch of dissected vessels of various sizes [32]14

Figure 3.3: (a) Photograph of burst pressure setup, with pressure meter, syringe pump, and

iris mount; (b) Magnified diagram of iris clamp and blood vessel sample. [32].....14

Figure 3.4: Blood pressure as a function of vessel size [43]15

Figure 4.1: Absorption spectra of fluorophores found in the blood vessel wall with 340 nm

excitation wavelength marked for reference19

Figure 4.2: (A) Diagram of experimental setup used for laser sealing of blood vessels;

(B) Diagram of experimental setup used for excitation and collection of tissue fluorescence

signal. The fluorescence spectrum was acquired before and after sealing vessels19

Figure 4.3: Photons detected by the spectrometer as a function of integration time (IT).

The signal is truncated at wavelengths < 360 nm due to use of a 360 nm cut-on filter, and the

sharp peak just beyond 360 nm is an artifact of the LED source, which had a center wavelength of 340 nm, but a FWHM bandwidth of 20 nm. The signals for an IT of 3 s and 4 s are saturated near 360 nm.....21

Figure 4.4: Comparison of fluorescence spectra between native blood vessels (blue) and laser sealed blood vessels (red), using an IT of 1 s. Note that in the highlighted 470-520 nm spectrum, the sealed tissue has a signal approximately 70% higher than that of the native tissue22

Figure 4.5: Blood vessel burst pressures as a function of vessel diameter and laser parameters for the control group (5 W, 5 s) and sealing group (30 W, 5 s).....24

Figure 4.6: Representative photographs of blood vessels. (A) Native blood vessel, $d = 3.4$ mm; (B) Failed seal using 5 W for 5 s, $d = 4.2$ mm, BP = 7.5 mmHg; and (C) Successful seal using 30 W for 5 s, $d = 4.0$ mm, BP = 370 mmHg24

Figure 4.7: Successful vessel seals performed at 30 W for 5 s. The inset shows the initial decay in fluorescence signal before the increase in signal as the seal is created. The highlighted region shows that vessel seal times of 3.0 - 4.0 s provided successful seals for the majority of the vessels. Mean vessel diameter was 2.9 ± 0.4 mm and mean BP was 533 ± 121 mmHg ($n = 11$)25

Figure 4.8: Average increase in fluorescence signal of successful vessel seals shown in figure 4.726

Figure 4.9: Fluorescence signal for two vessels that experienced carbonization on the seal

zone. The signal decreases after $t = 3.5 - 4.0$ s, as the highly absorbing carbonized layer prevents photons from reaching the detector. The inset shows the clearly visible carbonized zone of tissue both on the front side (top) and backside (bottom). The vessel shown in the inset had a diameter of 2.8 mm and a BP of 463 mmHg27

Figure 4.10: Failed vessel seals performed at 5 W for 5 s. Note that the fluorescence signal decreases during initial heating before increasing again. Mean vessel diameter was 2.8 ± 0.5 mm and mean BP was 32 ± 31 mmHg ($n = 8$). At slower heating rates, indicated by the lower laser power, this decrease in signal is prolonged compared to rapid heating (inset in Figure 4.8).....28

Figure 4.11: Average change in fluorescence signal of unsuccessful vessel seals shown in figure 4.1028

Figure 5.1: Experimental setup for razor blade scans and spatial beam characterization38

Figure 5.2: The laser was connected to a side-firing fiber. Two mounts (not shown) prevented the fiber from rotating. An Arduino board was pre-programmed to a specific scan length and speed for the servo motor. The fiber was threaded through and locked down onto an arm attached to the servo motor. The servo motor was battery powered, with an external ON/OFF switch. The lower jaw consisted of steel tubing attached to quartz square tubing (25-mm-long with 2.7×2.7 [mm²] outer wall and 1.8×1.8 [mm²] inner wall). Black resin plugs sealed the optical chamber on both the proximal and distal ends, with small holes on

each end for insertion of a segment of the optical fiber (without jacket), and insertion of the thermocouple, respectively. The black plug on the distal end additionally served to absorb stray light in the forward direction. Vessel samples were compressed onto the quartz tubing using a glass slide, simulating a transparent upper jaw. (Diagram not drawn to scale)39

Figure 5.3: The initial laser beam profile exiting the optical fiber, used for both the quartz and sapphire in the Zemax computational simulations40

Figure 5.4: (A) Razor blade scans of output spatial beam profile in two orthogonal directions; (B) Image from IR beam profiler44

Figure 5.5: Representative thermocouple temperature measurements on the internal (T_{in}) and external (T_{out}) surfaces of the quartz and sapphire optical chambers, as a function of time.

All vessel sealing studies were performed with an incident laser power of 30 W at the tissue surface and a laser irradiation time of 5 s, at an infrared wavelength of 1470 nm46

Figure 5.6: Blood vessel burst pressures (BP) as a function of vessel diameter for the quartz and sapphire optical chambers. The dashed horizontal line shows the industry standard threshold of 360 mmHg (three times systolic blood pressure) for designation of a successful seal. For the quartz chamber, vessel BP averaged 883 ± 393 mmHg, with 13/13 vessels (100%) recording BPs above 360 mmHg. For the sapphire chamber, vessel BPs measured 412 ± 330 mmHg, with 10/14 vessels (64%) sealed48

Figure 5.7: Photographs of the vessels before and after sealing for sapphire and quartz.

(A–C) A 3.5 mm diameter vessel in its native state, as well as after it was sealed unsuccessfully using the sapphire chamber, showing its front side, and back side, respectively.

(D, E) A 3.3 mm diameter vessel, showing its front and back sides, respectively, after a successful seal (BP = 554 mmHg) using the sapphire chamber. (F–H) A 3.3 mm diameter vessel in its native state, as well as after it was sealed successfully (BP = 776 mmHg) using the quartz chamber, showing its front side and back side, respectively. All vessels sealed with the quartz chamber were successful. An incomplete zone of the thermal coagulation on the backside of the vessel is observed for the failed seal using the sapphire optical chamber in image (C).....49

Figure 5.8: Ray tracing showing both (left column) beam divergence through the optical chamber and (right column) output beam profile, for both quartz (top row) and sapphire (bottom row), using Zemax optical software. The location of the detector surface in the simulations is denoted by a vertical black line on the right edge of each optical chamber. Note that the quartz chamber had curved edges, due to commercial availability of square quartz tubing, while the sapphire chamber was assembled from four individual optical windows, resulting in straight edges, due to the lack of commercial availability for square sapphire tubing.....51

Figure 5.9: Monte Carlo simulations showing light transport through the quartz chamber (green) and into the tissue layer (gray). A total of 1 million light rays were used in the simulations, with 8.7% of the light rays transmitted through the tissue layer, 6.6% percent of

the light rays reflected back into the chamber, and the remaining 84.7% of the light rays absorbed in the tissue52

Figure 5.10: COMSOL thermal simulations showing the temperature profile on the external surface of the quartz chamber (with plugs inserted on both ends) at different time points of $t = 0$ s (start of laser irradiation), $t = 3.25$ s (during laser irradiation), $t = 5$ s (after laser de-activated), and $t = 22$ s (after 16 s of cooling).....54

Figure 5.11: External temperature (in Kelvin) of the quartz chamber as a function of time. Laser is activated at $t = 0$ s and de-activated at $t = 5$ s. The highest temperature was 351 K (77.85°C), with cooling time of 16 s to reach body temperature (37°C), consistent with experimental results55

Figure 6.1: The laser was connected to a side-firing fiber. Two mounts (not shown) prevented the fiber from rotating. An Arduino board was pre-programmed to a specific scan length and speed for the servo motor. The fiber was threaded through and locked down onto an arm attached to the servo motor. The servo motor was battery powered, with an external ON/OFF switch. The lower jaw consisted of steel tubing attached to quartz square tubing (25-mm-long with 2.7 x 2.7 mm OD and 1.8 x 1.8 mm ID). Black resin plugs sealed the optical chamber on proximal and distal ends, with small holes on each end for insertion of the bare optical fiber (with jacket removed), and insertion of the micro-thermocouple, respectively. The black plug on the distal end additionally served to absorb stray light in the forward direction. Vessel samples were compressed onto the quartz tubing using a glide slide, simulating a transparent upper jaw63

Figure 6.2: Experimental setup for acquiring the optical transmission signal during continuous-wave laser ablation of compressed porcine renal blood vessels. (Left top inset) Start of formation of a carbon layer on the tissue surface during laser irradiation. (Right top inset) Formation of a hollow crater during irradiation65

Figure 6.3: (A) Photograph of a vessel after bisection using 59 W for 5 s. A fascia layer is visible and the vessel was easily detached by pulling uniformly from both sides. (d = 3.2 mm, BP1: 460 mmHg, BP2: 776 mmHg). (B) Photograph of a vessel after bisection using 59 W for 6 s. A clean cut is shown (d = 3.5 mm, BP1: 1160 mmHg, BP2: 372 mmHg). (C) Comparison of laser incident power and irradiation times for each data set.

Laser irradiation times shorter than 5 s resulted in tissue cutting, but not sealing, presumably due to insufficient thermal conduction and thermal spread during the laser treatment time.

Laser incident powers less than 41 W failed to produce a full-thickness cut, due to insufficient irradiance67

Figure 6.4: Optical transmission signal as a function of time during CW laser tissue ablation and (inset) the representative tissue sample (d = 3.2 mm).....69

Figure 6.5: Ray tracing showing beam divergence through the quartz chamber and (right column) output beam profile, using Zemax optical software. The location of the detector surface in the simulations is denoted by a vertical black line on the right edge of each optical chamber70

Figure 7.1: Diagram of the proposed laparoscopic device with quartz jaws and optical feedback system. The therapeutic, reciprocating, side-firing, optical fiber is housed in the

bottom fixed jaw, while a linear array of four photodiodes and a neutral density filter for
diagnostic feedback, is housed in the upper, hinged, active jaw74

Chapter 1 : INTRODUCTION

Suture ligation of blood vessels during surgery can be time-consuming and skill-intensive. Energy-based electrosurgical and ultrasonic devices have recently replaced the use of sutures and mechanical clips (which leave foreign objects in the body) for many surgical procedures providing rapid hemostasis during surgery. About 80% of the 15 million laparoscopic surgical procedures performed globally each year utilize these energy-based surgical devices [1]. These devices are primarily used for the sealing and cutting of blood vessels and vascular tissue bundles. These instruments first compress the blood vessel and collapse the vessel's internal lumen. The devices then denature connective tissue proteins in the blood vessels to seal the lumen in order to withstand systolic (120 mm Hg) and hypertensive (180 mm Hg) blood pressures and restrict blood flow. Finally, the devices then bisect the blood vessel or vascular tissue bundle, thus enabling hemostatic seals, while also clearing a path forward during laparoscopic surgery for the surgeon to reach the diseased tissue to be removed.

Currently, the two most common energy-based instruments used in operating rooms to seal and bisect blood vessels are ultrasonic (US) and radiofrequency (RF) devices. Ultrasonic technology uses a vibrating tip to coagulate and cut blood vessels. The US technology utilizes frictional energy which is generated through a linear piezoelectric crystal driven at a high vibration frequency (up to 55 kHz). These high-frequency US waves are absorbed by the vascular tissue, which seals (~20 kHz) and cuts (~ 55 kHz) in the specified areas [2]. Once absorbed, the mechanical energy is converted into heat, which is the mechanism that denatures the proteins in the blood vessel, causing a seal at low frequencies or vaporization of tissue at higher frequencies [2]. The ultrasonic scalpel has two jaws: an upper jaw that linearly oscillates and a lower jaw that is stationary and is used only to provide pressure to clamp the vessel in place.

Radiofrequency technology (e.g. LigaSure device), achieves hemostasis through the use of bipolar radiofrequency (RF) energy at a frequency of 473 kHz [3]. These devices generate an alternating electrical current passed through both sides of the blood vessel, providing resistive or Ohmic heating, and resulting in thermal coagulation of the vessels. The RF device has two jaws; the vessel is clamped between these two jaws and the electrical current is passed through the blood vessel. After the blood vessel has transformed sufficient electrical current to heat through Ohmic heating, a mechanical blade is deployed to bisect the seal [3]. The LigaSure device is considered the current leader in the RF technology space due to its semi-automated process which operates using real-time feedback. The real-time feedback system, which is integrated into the LigaSure device, is called TissueFect™ sensing technology. TissueFect™ is designed to monitor the change in electrical impedance of the tissue in real time during procedures [4].

Both US and RF devices are used to expedite numerous surgical procedures, such as lobectomy [5,6], nephrectomy [7], gastric bypass [8-10], splenectomy [11,12], thyroidectomy [13-18], hysterectomy [19], and colectomy [20-23]. However, both technologies have two main limitations (Table 1.1). One major limitation is the potential to create an undesirably large collateral zone of thermal damage and tissue necrosis [24-26]. Second, their long sealing times and cooling times of the metallic jaws in between successive applications prolong surgery as well.

An infrared (IR) laser with a 1470 nm wavelength is currently being tested as an alternative energy source for blood vessel sealing applications. Because of their precise focusing capabilities and rapid heating, near IR lasers may eliminate these limitations and become a more efficient tool for surgical procedures [31-33]. The IR laser was used successfully during preliminary studies to denature proteins in the blood vessels and seal the lumen in order to withstand systolic (120 mm Hg) and hypertensive (180 mm Hg) blood pressures and restrict blood flow (Figure 1.1).

Furthermore, in previous studies, an optical diffuse transmission signal was measured to obtain real-time, closed-loop, feedback to indicate successful vessel seal endpoints during surgery [35]. This non-destructive technique was successfully correlated with traditional burst pressure measurements for seal strength verification. Moreover, in a previous work, ex vivo benchtop sealing and bisection of blood vessels, in a two-step, sequential approach was performed [33].

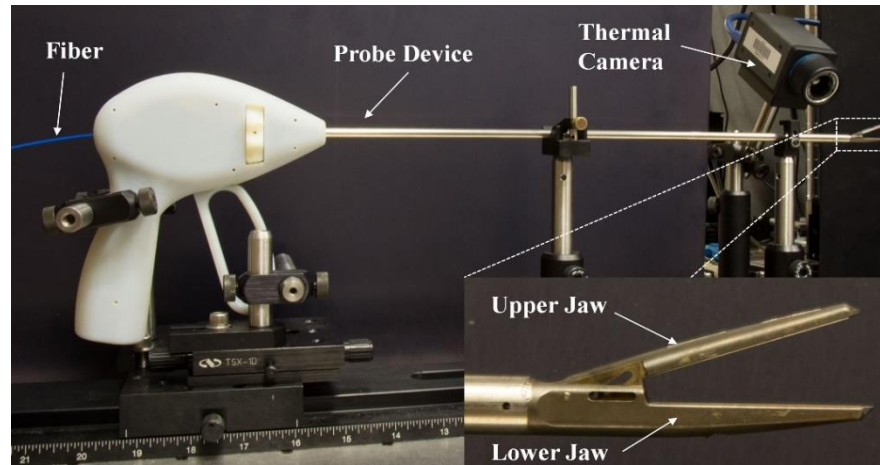


Figure 1.1: Prototype device with traditional 5-mm-OD laparoscopic jaws. Insert shows magnified view of upper and lower jaws on laparoscopic device. A thermal camera was used for temperature mapping.

Although the above-mentioned feedback technique successfully indicated vessel seals, it still has limitations as described in detail later in this thesis. This thesis describes the real-time change in tissue fluorescence as an alternative to the diffuse optical signal transmission technique as a feedback system during vessel sealing. This thesis also investigates the use of quartz and sapphire materials for constructing a transparent optical chamber for the laparoscopic device to avoid the overflow of laser energy in the case of smaller diameter vessels and to increase the surgical field of view. This thesis describes the feasibility of simultaneous IR laser vessel sealing and bisection in a single-step approach, using a transparent optical chamber that could be

integrated into a laparoscopic device. Moreover, the use of transmitted optical signal during vessel bisection as a real-time closed loop optical feedback system is also investigated. A prototype of the final laparoscopic device is proposed as well.

Table 1.1: Comparison of commercial and experimental vessel sealing and cutting techniques [24-31].

Device	US Energy	RF Energy	Vessel Ligation (clips)	Laser
Time to seal a blood vessel (s)	~ 5	~ 7	~ 51	~ 1
Cut without external blade	✓	×	×	✓
Thermal damage zone (mm)	2.7 ± 0.7	2.0 ± 0.4	NA	1.0 ± 0.4
Real-time feedback	✓	✓	×	✓
Need for safety glasses	×	×	×	✓
Mean vessel burst pressure (mmHg)	~ 200	~ 740	~ 720	~ 1300

Chapter 2 : THEORY

2.1: Optical properties of soft tissues

Light interacts with biological tissues in four major processes: reflection, refraction, absorption, and scattering. The extent of each of these interactions varies depending on the composition of the tissue. Reflection of light can be classified into two categories: specular and diffuse reflection. Specular reflection occurs when light interacts with a “glossy” or optically smooth surface. The surface can be considered optically smooth if the surface roughness of the interface is on the order of or less than the wavelength of light which is interacting with it. These specular reflections can be quantified using Fresnel equations, which depend on the index of refraction (n). Diffuse reflection occurs when light interacts with a surface which has a surface roughness greater than that of the wavelength of light interacting with it.

Absorption is the complete transfer of energy from an incident photon to the material. When an infrared photon is absorbed by a material, the molecules in the material vibrate and generally transform the energy into heat. There are specific wavelengths which can be absorbed by a material. In soft tissues, the absorption spectrum is determined by the type of cells the soft tissue is comprised of and the concentration of water in the soft tissue. The probability of the event that a photon is absorbed in the layer (unit path length) of soft tissue is defined as the absorption coefficient, μ_a (cm^{-1}), which varies with wavelength (Figure 2.1). When attempting to couple light into soft tissue and convert the optical energy into heat, a wavelength should be chosen corresponding to a high absorption coefficient. When absorption is the main interaction between the light and the material, and the absorption coefficient is much greater than the scattering coefficient ($\mu_a \gg \mu_s$), the propagation of the light through the tissue can be accurately modeled

using Beer's Law of attenuation. Beer's Law states that the rate of decrease in direct intensity of collimated light, if incident on a homogenous medium of thickness (x), is proportional to the intensity of the incident light.

$$-\frac{dI}{dx} \propto I \quad 2.1$$

In order to make these two quantities equal, the absorption coefficient must be used as a proportionality constant. Therefore, it can be stated as:

$$-\frac{dx}{dI} = \frac{1}{\mu_a I} \quad 2.2$$

Integrating the above equation results in:

$$-\int dx = \int \frac{1}{\mu_a I} dI \quad 2.3$$

$$-x\mu_a = \ln \frac{I_t}{I_o} \quad 2.4$$

$$I_t = I_o e^{-\mu_a x} \quad 2.5$$

where I_o is the initial intensity of the incoming light (W/cm^2) and I_t is the intensity of light transmitted at a tissue depth or thickness of x (cm).

When light is incident on a biological material, and the light is absorbed and then re-radiated at angles, it is referred to as scattered light. The total amount of scattering which occurs in the material is predicted by the probability of a scattering event occurring, which is referred to as a scattering coefficient, μ_s (cm^{-1}). The scattering coefficient is defined as:

$$\mu_s = \sigma_s N \quad 2.6$$

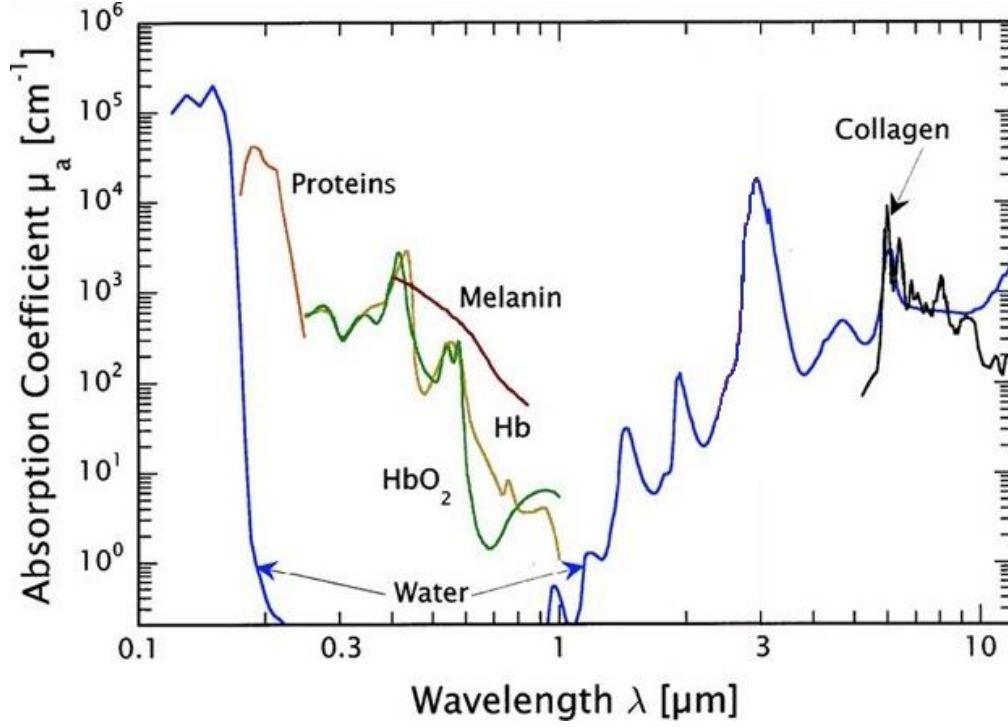


Figure 2.1: Optical absorption coefficients of soft tissue components: 0.1-10 μm spectrum [35].

where σ_s is the effective scattering cross section (cm^2) and N is the number of scatterers per unit volume (cm^{-3}). The summation of the scattering μ_s and the absorption μ_a is known as the total attenuation coefficient, μ_t . The mean free path (cm) between interaction events is given by the reciprocal of the total attenuation coefficient, $\frac{1}{\mu_t}$. When absorption does not dominate over scattering, Beers law can be written as:

$$I_t = I_o e^{-\mu_t x} \quad 2.7$$

The spatial distribution of the intensity of the scattered light is generated as a function of the size and shape of the inhomogeneities in the medium. The angular dependence of the scattering of light can be determined by the Henyey-Greenstein phase function, which is a photon transport equation, and is used to describe a material where $\mu_s \gg \mu_a$ hence;

$$p(\cos \theta) = \frac{1 - g^2}{2(1 + g^2 - 2g \cos \theta)^{3/2}} \quad 2.8$$

where p is the probability of light scattering in a certain direction and g is the anisotropy factor ($-1 \leq g \leq 1$). The anisotropy factor is the average cosine of the scattering angle. If the anisotropy factor is 1 or -1 then the light is observed as ballistic and is fully forward scattering or fully backward scattering, respectively. If the anisotropy factor is zero the scattering is isotropic. Most soft tissues have an anisotropy factor between 0.7 and 0.98 [37]. Light is primarily forward scattering when propagating through soft tissues. Another parameter measured is the attenuation of scattered light with depth in tissue, which is defined as the effective attenuation coefficient.

$$\mu_{eff} = \sqrt{3\mu_a(\mu_a + \mu'_s)} \quad 2.9$$

where μ'_s is the reduced scattering coefficient and considers the direction of the scatterers via the anisotropy factor.

$$\mu'_s = \mu_s(1 - g) \quad 2.10$$

The optical penetration depth (OPD) is a measure of how far light will propagate through the tissue before the intensity of the laser beam is reduced to $1/e$ (37%) of its initial value. It is simply calculated as the inverse of the effective attenuation coefficient, and OPD is given by the symbol, δ (cm).

$$\delta = \frac{1}{\mu_{eff}} \quad 2.11$$

Absorption and scattering coefficients of biological samples can be approximated theoretically from the known sample composition and are also found experimentally with available look up tables. These values refer to the laser tissue interaction as a static process. However,

dynamic changes in these values can occur under certain conditions (e.g. thermal coagulation or carbonization).

2.2 Dynamic optical properties of tissue response

2.2.1 The effects of spot size variation on optical penetration depth

Light, incident on soft tissue penetrates into the tissue as determined by its optical properties. However, for highly scattering materials $\mu_s \gg \mu_a$, the size of the collimated beam can change the OPD. A smaller beam width is associated with an increase in scattering, thus creating a shallower OPD. As the collimated beam width is increased, the scattering propagation of each photon has a greater possibility to propagate in the forward direction, which in turn creates a larger OPD, as observed in Figure 2.2 [34]. There is a greater probability of scattering effects overlapping in a forward propagation formation with a larger beam than that of a smaller beam. However, there is an upper limit to this relationship between beam width and OPD. There is a point at which the beam becomes so large that the scattering in the medium is saturated and the OPD will no longer increase with beam expansion. This value is achieved with a 5-12 mm beam width [38].

2.2.2 Dynamic tissue responses to temperature

Biological tissue samples can also have a dynamic response to light. When the incident flux of light on the tissue alters the cellular makeup of the tissue, then Beer's law no longer holds. There are five main classifications of dynamic light-tissue interactions: photochemical, photoablation, plasma induced ablation, photodisruption, and photothermal. This thesis will focus primarily on photothermal effects of light-tissue interactions, where light is converted into heat inside soft tissues. An example of a photothermal interaction is a high-power laser beam interacting

with a biological sample over a period of time. The high-power laser beam will, over time, fundamentally alter the protein structure in the tissue if the temperature of the tissue rises above approximately 60° C [39].

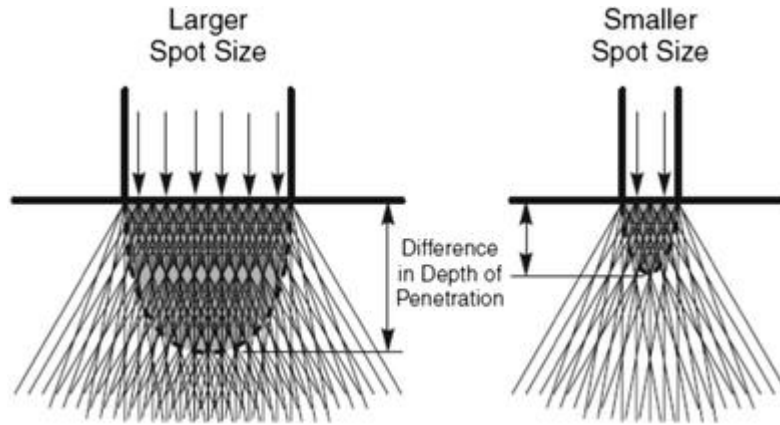


Figure 2.2: Overlapping scattering effects and the forward propagation of a larger beam spot leading to a deeper OPD [34].

The protein structure undergoes thermal denaturation (coagulation) which directly affects the optical properties of the tissue, where the most predominant change is observed in a significant increase in the scattering coefficient. When laser irradiation causes temperatures greater than 100°C, the process of vaporization begins, where the water in the soft tissue starts to form gas bubbles. These bubbles and the rapid change in the tissue volume causes thermal decomposition. If the tissue is heated much greater than 100°C then carbonization may occur, where carbon atoms are released and charring occurs on the tissue surface [39]. In this paper, the laser-tissue interaction will be in the form of a high power, near-IR laser, interacting with porcine blood vessels harvested from kidneys.

2.2.3 Dynamic tissue responses to compression

The laparoscopic jaws of an energy-based device are used to compress the tissues during a procedure. This compression causes the tissue width to increase by approximately 50% of its

original diameter [14]. Furthermore, biological tissue properties also change in response to compression [66]. During compression, a decrease in reflectance an increase in transmittance, absorption and scattering coefficients was reported. These effects are due to the shape changes of cellular components, index-mismatch reduction, and the increased scatterer and absorber concentration during compression.

Chapter 3 : METHODS

3.1 Anatomy of a vascular system and blood vessels

The human body's vascular network is considered a closed system. The closed system ensures that blood flows from the heart through arteries to specific organs and then travels back to the heart through the veins, completing the system. Vessels are tubular in shape and contain an internal lumen for blood flow. Blood vessels have five main classifications, based on size and function: the aorta, arteries, arterioles, capillaries, and veins. The following studies focus on sealing (the act of permanently fusing the lumen of the vessel) and cutting (the act of bisecting a vessel) of the arterioles, which range in size from 1 to 5 mm diameter. Arterioles are considered soft tissue composed of several different cellular layers (Figure 3.1).

There are three main layers in an arteriole: first, the inner most layer located next to the lumen, which is called the tunica intima and consists of endothelial cells, having a diameter on the order of 10 μm and making up about 11% of the vessel wall; second, the middle layer, which is known as the tunica media, and consists mostly of smooth muscle cells with an average cell diameter of 20 μm . This is generally the thickest layer in the vessel and makes up about 56% of the vessel wall. Third, the outer most layer known as the tunica externa consists primarily of collagen fibers which have a diameter of around 10 μm and make up about 33% of the vessel wall [40]. Knowledge of the structural makeup of the blood vessels enables us to compare like blood vessels and use similar coefficients which match a similar structural composition such as human aorta or porcine vessels.

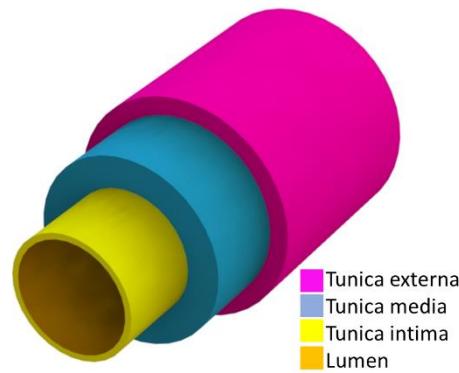


Figure 3.1: The structure of an arteriole vessel (not drawn to scale).

3.2 Tissue dissection

Porcine renal blood vessels were used for all preliminary laboratory studies. Fresh porcine kidney pairs were obtained, and renal blood vessels were then dissected, cleaned of fat, and stored in physiological saline prior to use. Through careful dissection it was possible to surgically expose the entire vascular tree for each kidney, providing multiple vessels with a wide range of diameters for testing. During preliminary studies, blood vessels were categorized as small (1-2 mm), medium (2-4 mm), and large (4-6 mm) samples (Figure 3.2).

3.3 Burst pressure readings

Vessel burst pressure measurements were used as the primary indicator of success. The burst pressure setup consisted of a pressure meter (Model 717 100 G, Fluke, Everett, WA), infusion pump (Cole Parmer, Vernon Hills, IL), and an iris clamp as a standard method for measuring vessel seal burst strength (Figure 3.3) [41-42]. The lumen of the vessel was placed over a cannula attached to the infusion pump. An iris was then closed to seal the vessel onto the cannula. De-ionized water was infused at a rate of 100 ml/hr and the pressure was measured with a pressure gauge. The maximum pressure (mmHg) achieved when the vessel seal bursts was then recorded.

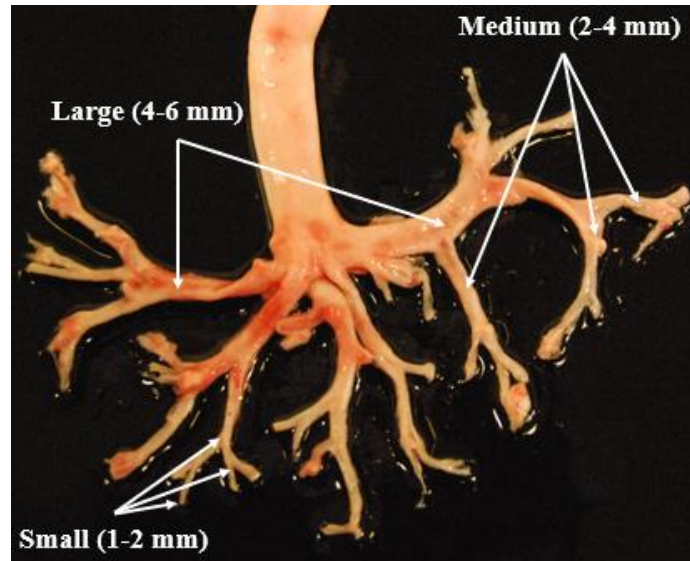


Figure 3.2: Porcine kidney and branch of dissected vessels of various sizes [32].

Blood pressure through a vessel varies with the size of the vessel. The pressure of the arterioles are between 40 mmHg and 100 mmHg (Figure 3.4). To quantify a successful seal, an industry standard threshold was used which quantifies systolic blood pressure slightly higher than average. In general, a seal is considered successful if the seal can withstand a pressure of three times systolic blood pressure (120 mmHg), equating to 360 mmHg. This overestimation for seal strength accounts for any anomaly of high blood pressure that may occur during surgery and provides a large safety margin for classifying a successful seal.

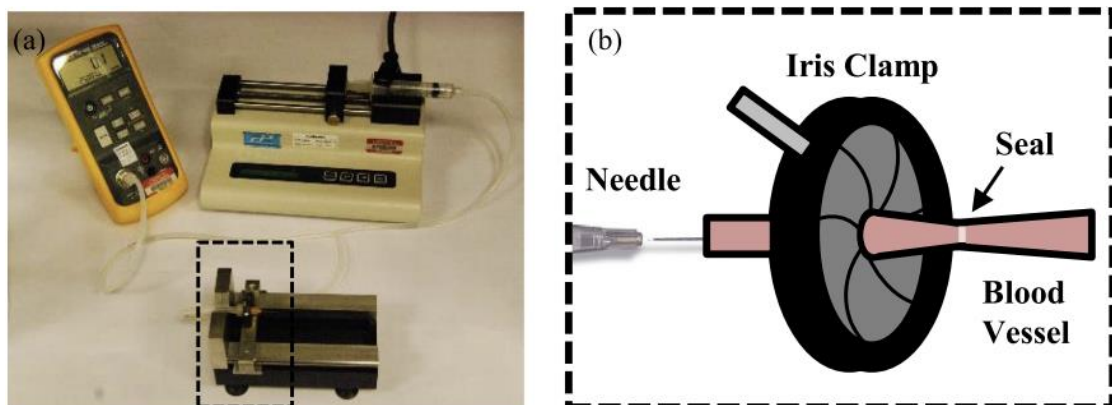


Figure 3.3: (a) Photograph of burst pressure setup, with pressure meter, syringe pump, and iris mount; (b) Magnified diagram of iris clamp and blood vessel sample. [32].

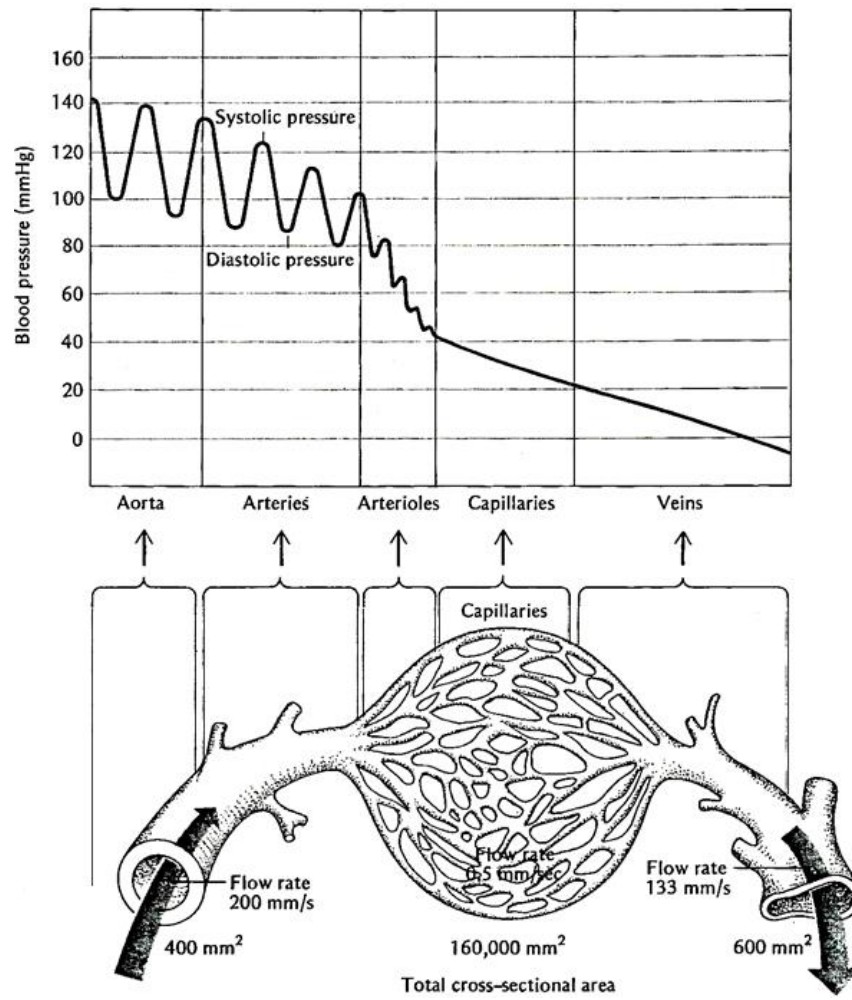


Figure 3.4: Blood pressure as a function of vessel size [43].

Chapter 4 : A REAL-TIME FLUORESCENCE FEEDBACK SYSTEM FOR INFRARED LASER SEALING OF BLOOD VESSELS

4.1 Introduction

It is common for conventional energy-based devices to incorporate real-time feedback in the form of either electrical impedance or temperature sensors [44-46]. Such feedback enables the surgeon to evaluate in real-time whether a blood vessel or vascular tissue bundle has been successfully sealed and may also serve as a closed feedback loop for automating energy delivery, thus saving valuable operating room time.

Several previous studies have also reported optical diagnostic approaches to differentiate between native and thermally sealed tissue for RF tissue fusion [47-50]. However, some of these studies relied on relatively complex feedback methods. In a previous study in the lab, simple and inexpensive alternative technique, using a real-time, diffuse optical transmission method during IR laser vessel sealing, was demonstrated. The method measured a reduced optical signal after vessel sealing, due to increased light scattering during tissue coagulation [35].

While the aforementioned feedback technique effectively identified vessel seals, It also has limitations that are discussed later in this chapter. This chapter explores differences in ultraviolet (UV) light induced fluorescence in blood vessel walls between native and thermally sealed vessels as a potential alternative, real-time, closed-loop, optical feedback technique for IR laser sealing of blood vessels.

4.2 Methods

Samples of renal arteries were obtained as described in chapter 3. For the initial non-real-time experiments, a total of 20 vessels ($n = 10$ in each arm, sealing or control) were used, ranging in outer diameter (OD) from 2.3 - 4.3 mm and with a mean diameter of 3.0 ± 0.6 mm. For the real-time experiments, a total of 19 vessels ($n = 11$ for sealing, or $n = 8$ for control) were used with OD ranging from 2.3 - 4.3 mm and with mean diameter of 2.8 ± 0.5 mm. Another two vessels were used to show the effect of tissue carbonization on fluorescence signal during real-time measurements.

All of the experiments were conducted using a 45-Watt diode laser with a central wavelength of 1470 nm (BrightLase, QPC Lasers, Sylmar, CA). Beer's law can be used to estimate the optical penetration depth, $\delta = 0.4$ mm, of 1470 nm radiation, because water is the major absorber of laser radiation in the near-IR to mid-IR spectrum and soft tissues are primarily composed of water (60 - 80%). Additionally, this optical penetration depth closely matches the compressed blood vessel thickness in the experimental benchtop set up of 0.4 mm, which allows for more effective energy deposition in the tissue. In group 1, for thermal coagulation and sealing, the laser was operated in long pulse mode with a pulse duration of 5 s, and an incident power of 30 W at the tissue surface, using 10 vessels and 11 vessels for the non-real time and real-time measurements, respectively. In group 2 (control), the laser was operated at 5 W for 5 s, providing tissue coagulation, but failed seals. These laser parameters were based on previous studies [35].

Fluorophores present in connective tissues are responsible for the fluorescence signal at specific wavelengths. The list of fluorophores along with their absorption spectra present in an arteriole vessel is shown in Figure 4.1 [51]. As mentioned in chapter 3, collagen and elastin make

up almost half of vessel walls, consequently they are selected as potential markers to observe the change for fluorescence spectrum. The optimal excitation wavelength for both collagen and elastin occurs near the UV wavelength of 340 nm, corresponding to an absorption peak absorption of both collagen and elastin [52]. Hence, an inexpensive, compact, light emitting diode (LED) (M340F4, Thorlabs, Newton, NJ) with a center wavelength of 340 nm, bandwidth of 20 nm (FWHM), and incident power of 0.1 mW, was used to induce tissue fluorescence in the compressed blood vessel walls. The LED spectrum rapidly decreased in the range of 369-374 nm, with no emission beyond 374 nm.

A UV-VIS spectrometer (AvaSpec-3648-USB2, Avantes, Lafayette, CA) was used to detect fluorescence and was sensitive across a wavelength range of 174 - 1100 nm. A diagram of the experimental setup for IR laser sealing of blood vessels is shown in Figure 4.2A. This setup was intended to mimic the tissue contact aspects of a surgical instrument while providing control over experimental variables that may impact results. The IR laser radiation was delivered through a 550- μ m-core, low-OH, silica optical fiber patch cable, with high-power SMA905 connectors on each end. The fiber output beam was collimated using a plano-convex lens. A second, cylindrical lens converted the circular beam to a linear beam, that measured 1 mm width by 12 mm length. This spatial beam profile provided a uniform distribution of laser power in a linear beam aligned perpendicular to the vessel length to provide a narrow, but full-width thermal coagulation zone and sealing of the vessel for a strong seal. Each vessel sample was sandwiched between a front glass slide and a back, metal faceplate with a glass slide insert. A gap stop of 0.4 mm was chosen in the setup to match the approximate optical penetration depth of the laser energy in the tissue for uniform heating and sealing of the vessel. Infrared laser energy was applied either at 30 W for 5 s to create a successful thermal seal or 5 W for 5 s to create a failed seal (control).

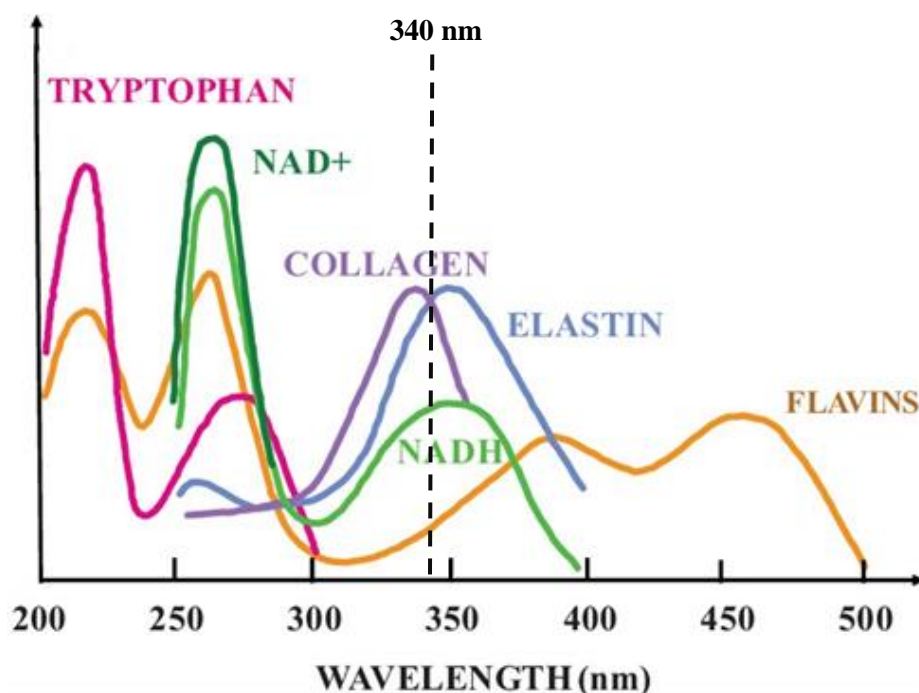


Figure 4.1: Absorption spectra of fluorophores found in the blood vessel wall with 340 nm excitation wavelength marked for reference.

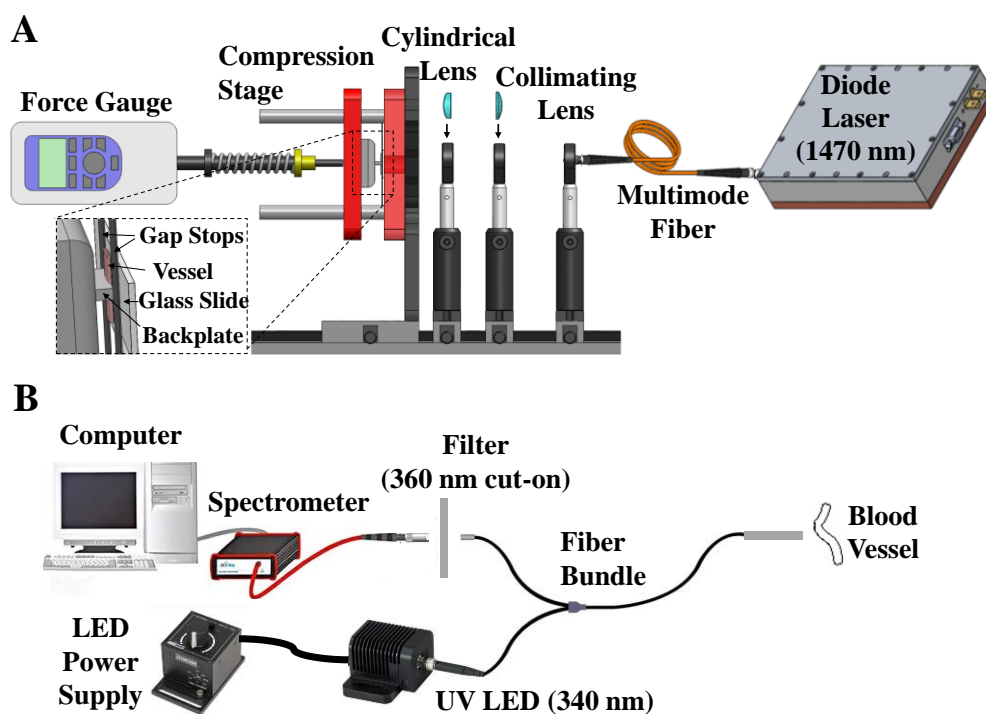


Figure 4.2: (A) Diagram of experimental setup used for laser sealing of blood vessels; (B) Diagram of experimental setup used for excitation and collection of tissue fluorescence signal. The fluorescence spectrum was acquired before and after sealing vessels.

The experimental setup for excitation and collection of the tissue fluorescence signal is shown in Figure 4.2B. A Y-shaped fiber bundle (RP22, Thorlabs), composed of seven 200- μm -core, high-OH, fibers was used. The central excitation fiber was split and connected to the LED, while the detection outer ring of six fibers was connected to the spectrometer. A long-pass filter with 360 nm cut-on wavelength (20CGA-360, Newport, Irvine, CA) rejected diffusely reflected excitation light. The blood vessel was compressed between two optical windows (WG11010R-A, Thorlabs) to mimic compression of the vessel between the jaws of a vessel sealing device. The distance between excitation fiber tip and vessel surface was fixed at 1.5 mm, including the 1 mm thickness of the window.

After completion of IR laser vessel sealing, industry standard destructive burst pressure (BP) measurements were conducted to determine seal strengths with the set up explained in chapter 3. Statistical analysis was performed to compare blood vessel diameter, increase in integrated fluorescence signal, and vessel burst pressures between the control (5 W, 5 s) and seal groups (30 W, 5 s). A two-tailed t-test was used with values of $p < 0.05$ considered to be statistically significant.

4.3 Results

4.3.1 System calibration

Fluorophores present in connective tissues are responsible for the fluorescence signal at specific wavelengths. The major proteins targeted for this study were the connective tissue proteins, collagen and elastin, found in the blood vessel wall. Hence, to induce fluorescence from these proteins inside the tissue, a 340 nm LED was used. It was also important to select an integration time (IT) for the spectrometer to capture desired photon counts for potential use as a

real-time optical feedback system. Preliminary studies were carried out for this purpose. Fig. 4.3 shows the number of photons detected in the fluorescence signal at different integration times. An IT greater than 1 s was judged too slow for use in a real-time feedback system. An IT of 100 ms yielded photon counts too low for consistent detection. An IT of 1 s was selected for non-real-time experiments, balancing a sufficiently high photon count with rapid ITs. The sharp peak just beyond 360 nm is an artifact of the LED source, which had a center wavelength of 340 nm but FWHM bandwidth of 20 nm, with a small percentage (1.8%) of diffusely reflected light from the tissue at wavelengths greater than 360 nm. The signal is also truncated for shorter wavelengths less than 360 nm, due to the presence of a 360 nm cut-on filter. Note that the peak signals near 360 nm were saturated for ITs of 3 s and 4 s.

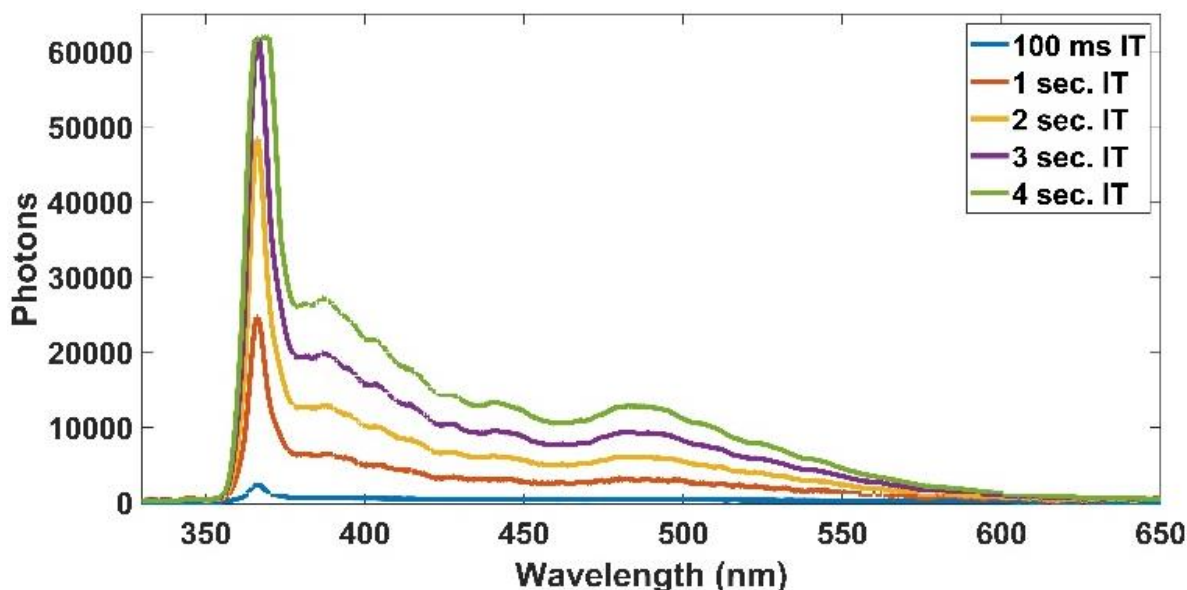


Figure 4.3: Photons detected by the spectrometer as a function of integration time (IT). The signal is truncated at wavelengths < 360 nm due to use of a 360 nm cut-on filter, and the sharp peak just beyond 360 nm is an artifact of the LED source, which had a center wavelength of 340 nm, but a FWHM bandwidth of 20 nm. The signals for an IT of 3 s and 4 s are saturated near 360 nm.

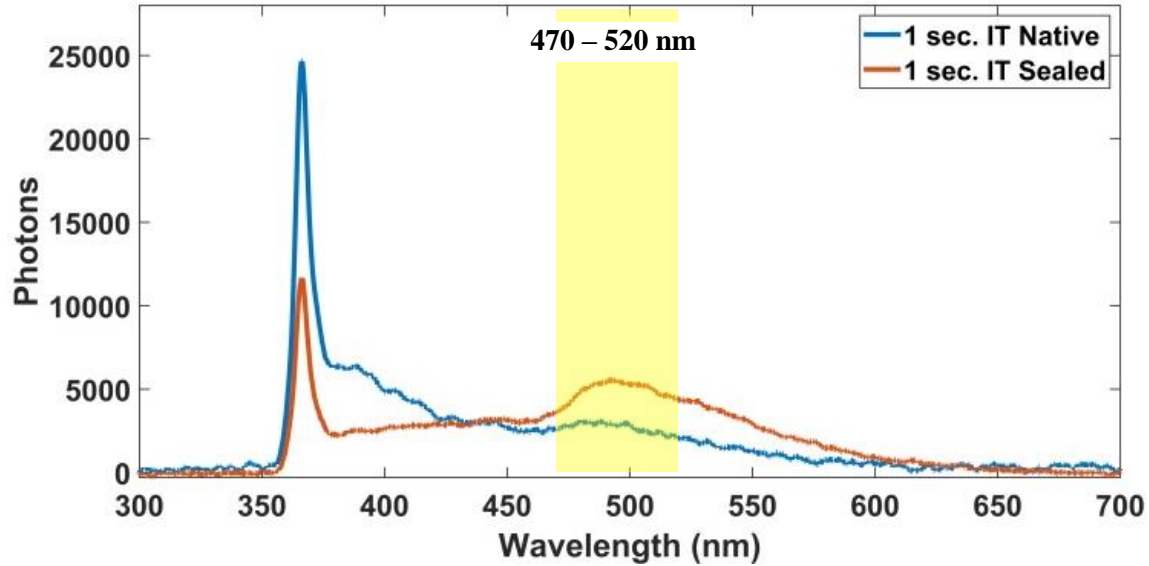


Figure 4.4: Comparison of fluorescence spectra between native blood vessels (blue) and laser sealed blood vessels (red), using an IT of 1 s. Note that in the highlighted 470–520 nm spectrum, the sealed tissue has a signal approximately 70% higher than that of the native tissue.

In Fig. 4.4, the fluorescence spectra of native blood vessels and laser sealed blood vessels are shown for an IT of 1 s. An increase in fluorescence signal in the highlighted 470–520 nm spectrum is observed, representative of a shift in the peak from 380 nm to 490 nm, upon laser sealing. In the 470–520 nm spectrum of interest, the sealed tissue emits a mean fluorescence signal $71 \pm 25\%$ higher than for the native tissue. Consequently, the 470–520 nm spectral range was selected for comparison of fluorescence between native, coagulated (5 W, 5 s), and sealed (30 W, 5 s) vessels.

4.3.2 Non-real-time measurements

Fig. 4.5 shows a scatter plot of burst pressure data for all vessels tested ($n = 20$), with criteria for success (360 mmHg), hypertensive blood pressure (180 mmHg), and systolic blood pressure (120 mmHg) dashed lines indicated for reference. The BPs for all coagulated tissues (5 W, 5 s) were below systolic blood pressure (120 mmHg), while BPs for all sealed vessels (30 W,

5 s) were more than three times higher than systolic blood pressure, satisfying the criteria for a successful seal.

The relatively large range observed in vessel BPs for successful seals (Fig. 4.5) is common, and has been previously reported during laboratory testing of both conventional RF and US devices and IR laser studies [30], [32], [35], [53-57]. This feature may be due in part to multiple variables including individual vessel diameter, collagen/elastin ratio, attached fatty tissue layers, and water content. For example, current clinical RF and US laparoscopic devices are used to seal a wide range of vessel sizes, ranging from 2–6 mm in diameter.

Table I summarizes these results. There was a statistically significant difference in both mean integrated fluorescence signal and mean burst pressures between failed seals (5 W for 5 s) and successful seals (30 W for 5 s) ($p < 0.05$). There was no significant difference between uncompressed vessel diameters in each group ($p > 0.05$), as planned. (It should be noted that vessel width increases by about 50% upon compression within the device jaws [14]). Successful vessel seals were judged using an industry standard of vessel BP ≥ 360 mmHg (three times systolic blood pressure). There was a $71 \pm 25\%$ increase in mean fluorescence signal between native and successfully sealed vessels as compared to only a $19 \pm 14\%$ increase in signal between native vessels and coagulated but failed vessel seals ($p < 0.05$). Sealed vessels (30 W, 5 s) also demonstrated high mean BP of 639 ± 189 mmHg. In the case of coagulated but failed vessels (5 W, 5 s), BP was only 39 ± 41 mmHg.

Figure 4.6 shows representative photographs of a native blood vessel, thermally coagulated blood vessel at 5 W for 5 s with a failed seal (BP = 7.5 mmHg), and thermally sealed blood vessel at 30 W for 5 s with a successful seal (BP = 370 mmHg).

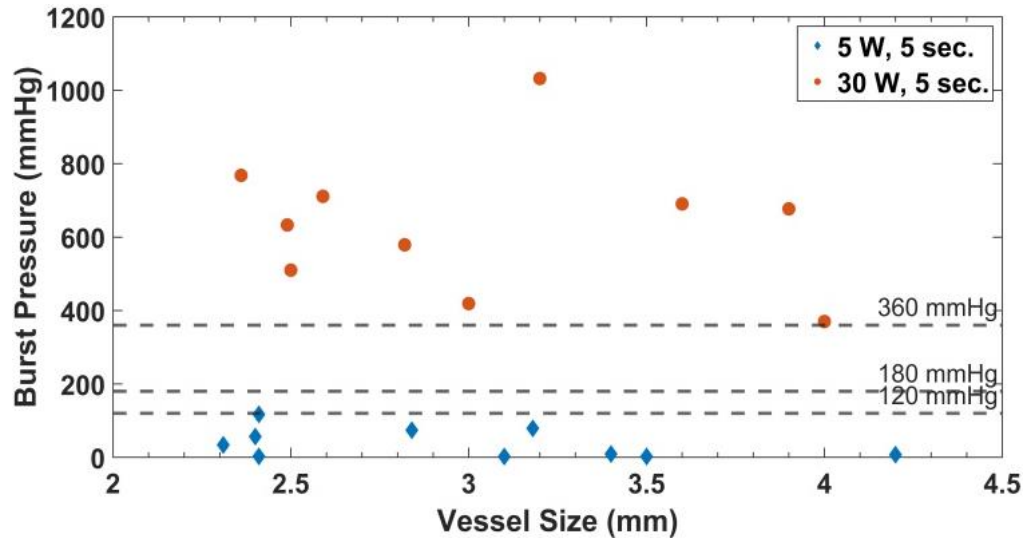


Figure 4.5: Blood vessel burst pressures as a function of vessel diameter and laser parameters for the control group (5 W, 5 s) and sealing group (30 W, 5 s).

Table 4.1: Increase in integrated fluorescence signal in 470-520 nm spectrum for successful and failed vessel seals.

Evaluation Criteria	Vessel Size (mm)	Mean BP (mmHg)	Δ Signal (%)	Sample Size (n)
Success (BP \geq 360)	3.0 ± 0.6	639 ± 189	71 ± 25	10
Failure (BP < 360)	3.0 ± 0.6	39 ± 41	19 ± 14	10
Significance	$p = 0.80$	$p = 1E-8$	$p = 2E-5$	NA

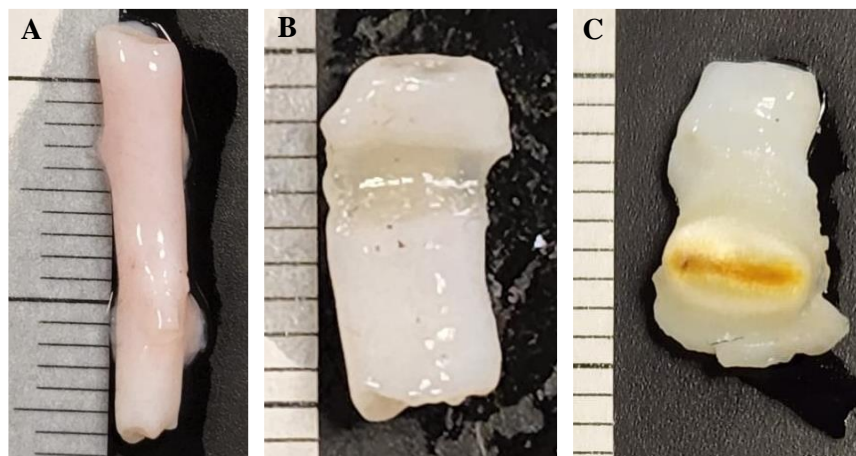


Figure 4.6: Representative photographs of blood vessels. (A) Native blood vessel, $d = 3.4$ mm; (B) Failed seal using 5 W for 5 s, $d = 4.2$ mm, BP = 7.5 mmHg; and (C) Successful seal using 30 W for 5 s, $d = 4.0$ mm, BP = 370 mmHg.

4.3.3 Real-time measurements

As a logical progression from non-real-time studies described above, real-time studies were also performed. Several adjustments to the experimental setup were necessary. First, integration time was decreased slightly from 1 s to 500 ms, thus allowing ten integrated fluorescence measurements to be acquired over the 5 s laser vessel sealing time. Second, both excitation and fluorescence were performed in reflectance mode, but on the back-side of the vessel. This setup is more practical since future clinical application would require that the diagnostic system be integrated into the upper hinged jaw of the laparoscopic vessel sealing system, while the lower fixed jaw would remain dedicated to the therapeutic, high-power IR laser delivery system. Another filter was also added to the setup before the long pass 360 nm cut off filter, to eliminate diffusely transmitted photons from the high-power, 1470 nm, therapeutic laser beam.

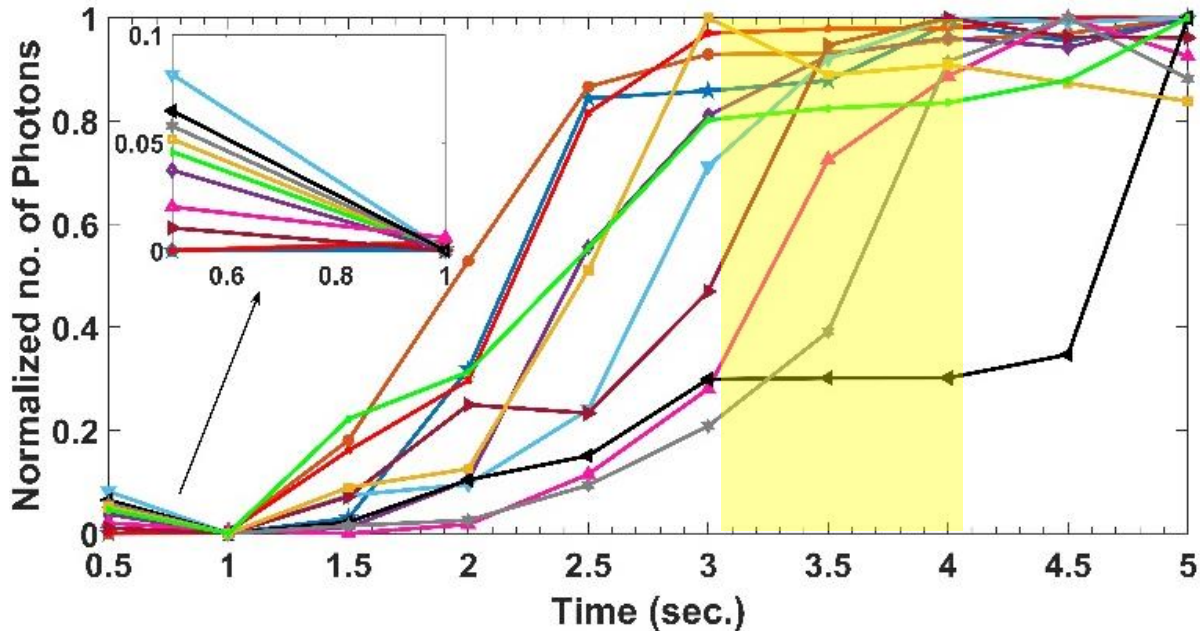


Figure 4.7: Successful vessel seals performed at 30 W for 5 s. The inset shows the initial decay in fluorescence signal before the increase in signal as the seal is created. The highlighted region shows that vessel seal times of 3.0 - 4.0 s provided successful seals for the majority of the vessels. Mean vessel diameter was 2.9 ± 0.4 mm and mean BP was 533 ± 121 mmHg ($n = 11$).

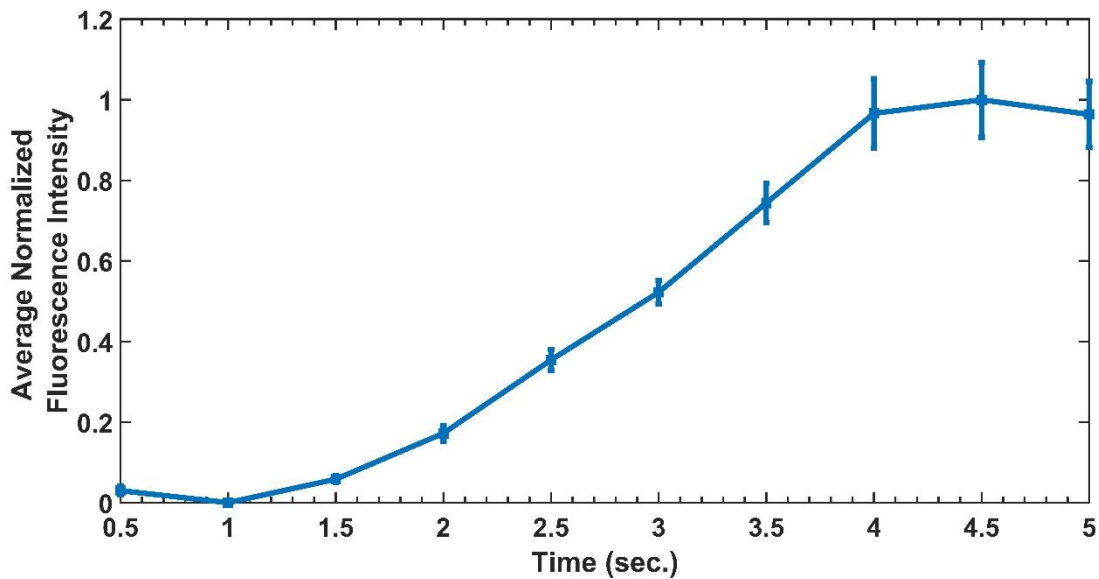


Figure 4.8: Average increase in fluorescence signal of successful vessel seals shown in figure 4.7.

Figure 4.7 plots the normalized integrated fluorescence data for successful laser vessel seals (30 W for 5 s). The inset box shows that the signal initially decreases ($t = 0.5 - 1.0$ s) before increasing and eventually reaching a plateau, corresponding to a strong vessel seal. The initial decrease in intensity can be attributed to photon absorption in water. Subsequently, as tissue denaturation starts, the signal begins to rise, eventually reaching a plateau, indicative of a vessel seal. An 80% increase in fluorescence signal from the baseline signal could serve as a threshold for indicating when a seal is sufficiently strong, for the system to immediately de-activate the laser. In this data set, the majority of vessel samples were sealed after $t = 3.0 - 4.0$ s (highlighted area), corresponding to a normalized integrated fluorescence signal above 0.8, as indicated by the plateau in the signal. Only one vessel (black line) produced a signal that was weak and slow to rise above this threshold. One observation for this data is that the vessel slipped slightly out of the holder, which resulted in misalignment of the fluorescence collection fiber bundle with the seal zone.

Figure 4.8 shows the normalized integrated fluorescence data for two successful seals (30 W for 5 s) that also experienced significant charring on both the front and back surfaces of the seal zone. This data has the characteristic initial decrease in signal ($t = 0.5 - 1.0$ s) followed by an increase in signal with sealing, similar to Figure 4.7. However, as the carbonized zone in the tissue layer is created and extends to the back-side of the vessel as well, the signal then decreases again. This sharp decay in signal was only observed in vessel seals with carbonized zones reaching the back-side of the vessel (Figure 4.8 inset), but not in normal sealed vessels without carbonization (Figure 4.7). It is likely that the highly absorbing black zone of carbonized tissue resulted in fewer photons reaching the detector. Figure 4.10 plots the normalized integrated fluorescence data for the failed seals (5 W for 5 s). Due to the lower incident power and hence slower tissue heating, the decrease in fluorescence signal as compared to the baseline signal observed in Figures 4.7 and 4.9, is extended over a longer duration, before the fluorescence signal increases with tissue coagulation.

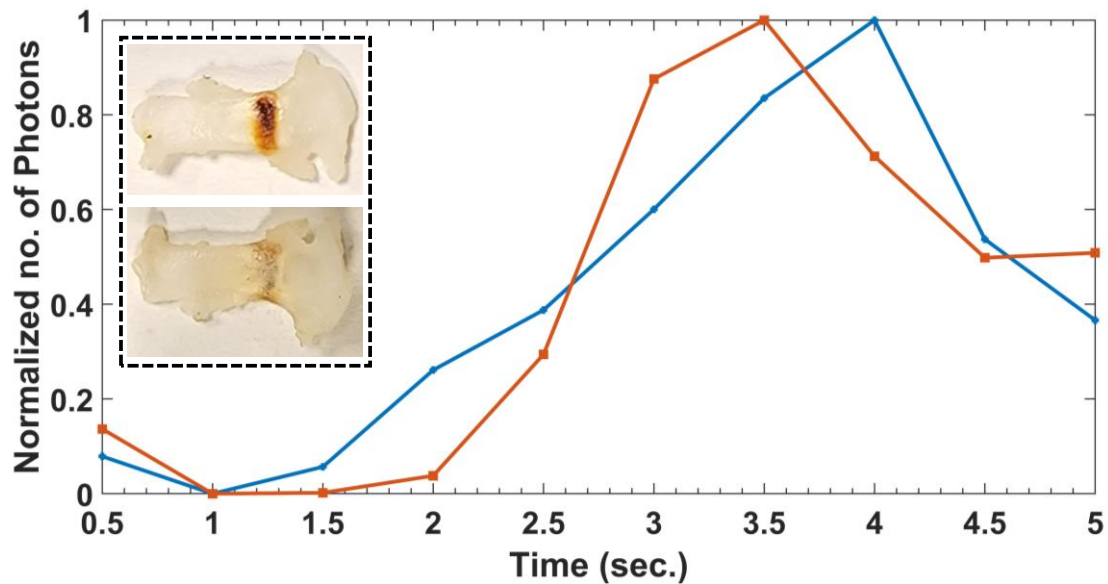


Figure 4.9: Fluorescence signal for two vessels that experienced carbonization on the seal zone. The signal decreases after $t = 3.5 - 4.0$ s, as the highly absorbing carbonized layer prevents photons from reaching the detector. The inset shows the clearly visible carbonized zone of tissue both on the front side (top) and backside (bottom). The vessel shown in the inset had a diameter of 2.8 mm and a BP of 463 mmHg.

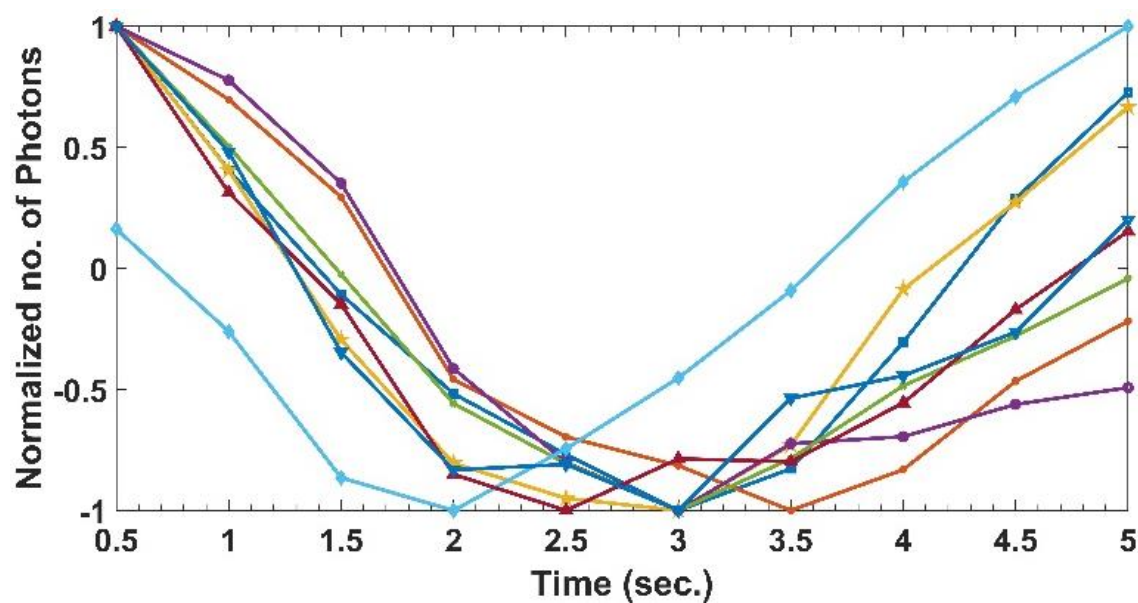


Figure 4.10: Failed vessel seals performed at 5 W for 5 s. Note that the fluorescence signal decreases during initial heating before increasing again. Mean vessel diameter was 2.8 ± 0.5 mm and mean BP was 32 ± 31 mmHg ($n = 8$). At slower heating rates, indicated by the lower laser power, this decrease in signal is prolonged compared to rapid heating (inset in Figure 4.8).

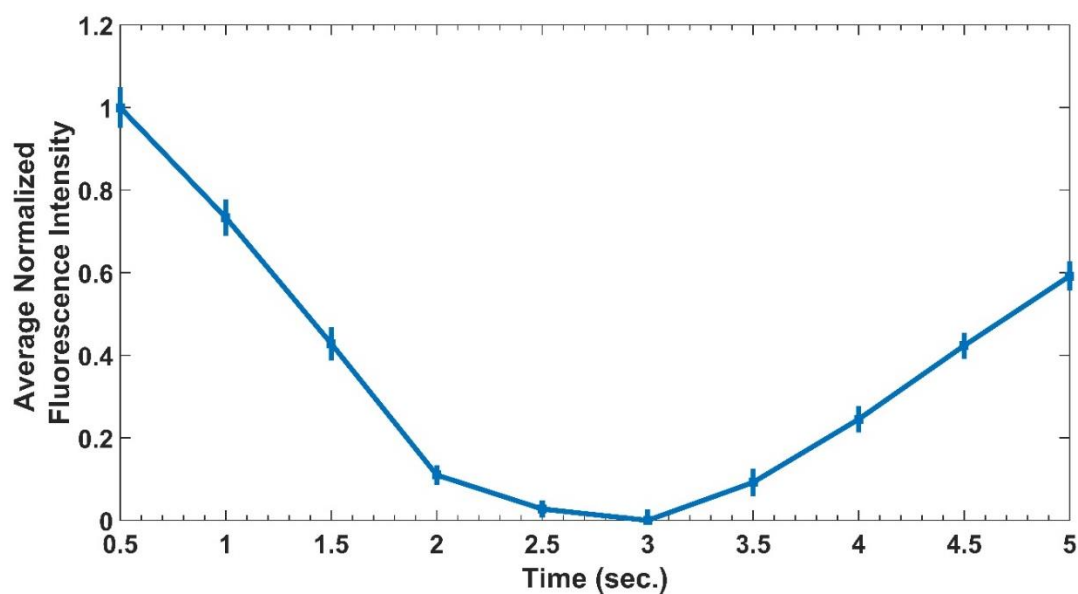


Figure 4.11: Average change in fluorescence signal of unsuccessful vessel seals shown in figure 4.10.

4.4 Discussion

The results of this study demonstrated that the change in fluorescence signal can be used as a real-time, non-destructive optical method for predicting successful vessel seals, as opposed to destructive vessel BP measurements, which although practical in the laboratory, are not clinically useful. Numerous previous studies have reported on the absorption and excitation spectrum of different fluorophores in tissues [58-64]. The fluorescence signal from blood vessel walls is dominated by collagen and elastin connective tissue proteins, which are responsible for the stiffness and elasticity of blood vessels. Multiple previous studies have reported the absorption spectrum for collagen and elastin [58-59], [63]. The optimal excitation wavelength for both collagen and elastin occurs near the UV wavelength of 340 nm [58]. Consequently, a compact, inexpensive, low-power, 340 nm LED was used for this study. Both native elastin and collagen have their highest fluorescence signal in the 390–400 nm range [62]. However, as the data in this study shows, the fluorescence peak shifts to about 490 nm upon laser thermal coagulation of blood vessels. Therefore, integration of the fluorescence signal in the spectrometer was also limited to the 470–520 nm range for these studies.

Interestingly, during the real-time studies, it was observed that the integrated fluorescence signal in the 380–420 nm spectrum decayed immediately upon laser heating and thermal coagulation of the vessel, before a sufficiently strong seal was obtained. On the contrary, in the 470–520 nm spectrum, the integrated fluorescence signal gradually increased (as shown in Fig. 4.7), correlating with the formation of a strong vessel seal.

Other tissue components, including NADH and flavins, may contribute to the fluorescence signal. However, at the excitation wavelength of 340 nm, the absorbance of NADH is about 50%

of collagen and elastin, while for flavins the absorbance is less than 10% of collagen and elastin [65].

Denaturation of collagen begins at about 65 °C, while elastin denaturation begins at a much higher temperature of 200 °C [58]. However, the vessel must experience a temperature range of 200–300 °C to achieve a successful seal, as previously reported [35], [66]. Hence, the shift in fluorescence peak is likely attributed primarily to denaturation of collagen and elastin.

The laser thermal denaturation of collagen and elastin in blood vessels corresponded to successfully sealed vessels with a $71 \pm 25\%$ increase in integrated fluorescence signal in the range of 470–520 nm. Real-time measurements also showed a gradual increase in fluorescence signal in the 470–520 nm range, eventually reaching a plateau after $t = 3.0\text{--}4.0$ s.

The observation in Fig. 4.7 that the majority of vessels reached a peak fluorescence signal after only $t = 3.0\text{--}4.0$ s is interesting for several reasons. First, a potential closed-loop optical fluorescence feedback system that automatically deactivates the laser immediately upon a successful seal, as denoted by peak fluorescence, would save time. The surgical device is activated numerous times for any given procedure, so the savings in valuable operating room time may quickly add up. Second, by reducing unnecessary laser activation time, the maximum temperature of the laparoscopic device jaws will also be correspondingly lower. In general, laparoscopic device temperatures are linearly dependent on time, and may rapidly heat up to high temperatures (up to hundreds of degrees Celsius), within a few seconds. For example, a recent study reported that maximum device temperatures ranged from 94–133 °C for RF devices and 81–350 °C for US devices [57]. However, device jaws take much longer to cool down (tens of seconds), with average cooling times of 54 s and 68 s recently reported for two different RF devices [68], so time savings in between successive applications would be even greater. Third, lower device temperatures should

in turn translate into an improved safety profile. The probability of burns will be decreased if a surgeon accidentally touches adjacent tissues with the device when operating in closely confined anatomic spaces commonly encountered during laparoscopic surgery.

A previous preliminary study in our laboratory reported use of diffuse optical transmission as a non-destructive, real-time, optical feedback system for laser sealing of blood vessels [35]. This method used a red aiming beam integrated into the high power IR laser module, to detect a decrease in transmitted signal collected by an optical fiber during laser thermal coagulation and sealing of blood vessels. Advantages of this method include fast and easy detection in a low-cost setup. Disadvantages include the need for a large core, large NA fiber to collect sufficient highly scattered light. Also, un-scattered light overflowing the vessel diameter may still erroneously contribute to the signal.

On the contrary, the real-time, fluorescence-based optical feedback system described in this study is not affected by the diameter of the blood vessels, since the measurements are performed in reflection mode on the back-side of the vessel, and with a small beam focused on the tissue, while filtering out the high-power 1470 nm therapeutic and 635 nm red aiming beams. Therefore, the difference in the fluorescence signal will remain the same even if the IR laser beam overflows the vessel when the beam is incident on blood vessels with smaller diameters.

Furthermore, in this study, a high-power light source was not required either. A central, 200- μ m-core fiber, within a 7-fiber optic bundle was used, providing 0.1 mW of excitation power to the tissue. This beam generated a sufficient fluorescence signal to be used as an optical feedback system. Moreover, a surrounding detection ring of six 200- μ m-core fibers with 0.22 NA, was used to collect the fluorescence signal with an integration time of 1 s and 500 ms in the case of non-real time and real-time measurements, respectively. There does not appear to be a need to increase the

number of fibers and/or use higher NA fibers for this feedback system to be integrated inside a standard laparoscopic device and Maryland jaw configuration for clinical applications.

Table 4.2 provides a brief comparison of the diffuse optical transmission [35] and fluorescence signal methods for potential use as real-time, optical feedback systems during IR laser sealing of blood vessels.

Some conventional electrosurgical devices use electrical impedance as an active feedback system to determine when a successful vessel seal has been achieved. However, such measurements also have limitations. For example, the electrical impedance of an organ can vary widely, based on composition such as vascular, muscle, fat, and fibrous content. Furthermore, there is not a known impedance value that guarantees a strong vessel seal. Electrosurgery in general also carries additional risks including electrical interference with implants and materials. Thermal damage due to electrical current spread also prevents use of electrosurgical devices near sensitive structures such as nerves (e.g., nerve-sparing radical prostatectomy) [69].

Table 4.2: Comparison of diffuse transmission and fluorescence optical feedback methods for IR laser vessel sealing.

Technique	Advantages	Disadvantages
Diffuse Transmission	<ul style="list-style-type: none"> • Very fast and inexpensive detector. • Low-power, low-cost red aiming beam, integrated with IR laser & same delivery fiber. 	<ul style="list-style-type: none"> • Signal varies based on amount of light overflowing vessel width. • Highly scattered light requires large-core, large NA fiber for signal.
Fluorescence	<ul style="list-style-type: none"> • Fast detection. • Strong signal using small, low NA fibers. • Low-power, low-cost UV sources. 	<ul style="list-style-type: none"> • Fiber bundle may be difficult to integrate into laparoscopic jaw. • More expensive detector. • Signal varies among vessels due to protein composition.

4.5 Conclusion

In summary, this chapter described the successful application of fluorescence of blood vessels for real-time feedback system for IR laser sealing. The tissue integrated fluorescence signal increase across the 470 - 520 nm spectrum acquired using short (1 s) integration times, was correlated with vessel burst pressure measurements. Mean integrated fluorescence signal increased by about 70% for successful seals (30 W for 5 s) versus 20% for failed seals (5 W for 5 s). A gradual increase in integrated fluorescence during real-time measurements was also observed. The signal reached a plateau after $t = 3.0 - 4.0$ s, indicating that shorter seal times than 5 s are possible. It is therefore proposed that sealing time of 3 s and 4 s will be tested in the future with the same 30 W laser.

Chapter 5 : COMPARISON OF QUARTZ AND SAPPHIRE OPTICAL CHAMBERS FOR INFRARED LASER SEALING OF VASCULAR TISSUES USING A RECIPROCATING, SIDE-FIRING OPTICAL FIBER: SIMULATIONS AND EXPERIMENTS

5.1 Introduction

A design limitation in the use of IR laser sealing and cutting is the size constraints of the standard Maryland style jaw and the 5-mm-outer-diameter (OD) shaft of laparoscopic devices. The bottom fixed jaw design will need to reflect the beam at a 90° angle and create a uniform linear beam profile, all within limited space. The top jaw, with a pivoting hinge, serves to open and close for grasping vessels and provides tissue compression during sealing. Previous laboratory studies characterized a reciprocating, side-firing, optical fiber to produce a uniform linear beam profile within a standard Maryland laparoscopic jaw design [54].

However, there are several technical limitations of this approach. First, the non-transparent, metallic jaws of the device and the limited surgical field-of-view may make accurate positioning of tissues within the jaws difficult to observe. Second, a wide range of blood vessel diameters (2-6 mm), are typically treated during surgery. Therefore, a fixed scan length for the reciprocating fiber is not desirable, as a short scan length may not provide a full-thickness seal in larger vessels. A long scan length may result in excessive laser energy being transmitted around the edges of a small vessel, in turn producing higher jaw temperatures and longer cooling times in between applications than acceptable clinically.

This chapter describes the initial testing and comparison of quartz and sapphire transparent and biocompatible materials for use in an optical chamber, a key component of the laparoscopic device jaw. This approach may enable improved visibility for positioning vascular tissues within

the laparoscopic device jaws and customization of the reciprocating fiber scan length to match the compressed width of the blood vessels. Optical and thermal characterization of the quartz and sapphire tubing was performed using both experiments and computer simulations. Infrared laser sealing of porcine renal blood vessels was also conducted to determine whether industry standard destructive vessel burst pressure (BP) measurements in the laboratory are sufficient for potential future surgical application, as judged by BP needing to exceed 360 mmHg (three times normal systolic blood pressure).

5.2 Experimental Methods

Samples of renal arteries were obtained as described in chapter 3. A similar range of vessel diameters was chosen for the quartz and sapphire treatment groups, for direct comparison. A total of $n = 13$ blood vessels with a mean, uncompressed diameter of 3.4 ± 0.7 mm, were selected for tests with the quartz chamber, while a total of $n = 14$ vessels with a diameter of 3.2 ± 0.7 mm, were used with the sapphire chamber ($p = 0.41$). A 100-Watt, 1470 nm wavelength IR diode laser (BrightLase, QPC Lasers, Sylmar, CA) was used for vessel sealing studies. The laser was operated in continuous-wave (CW) mode with incident power at the tissue surface of 30 W for 5 s, based on previous studies [35][54][70]. Laser power output was calibrated using a meter (EPM1000, Coherent, Santa Clara, CA) and detector (PM-150, Coherent). Blood vessel samples were compressed using a 0.5- mm-thick optical window locked in a clamp, to simulate a transparent active jaw. An optical coherence tomography (OCT) system (Niris, Imalux, Cleveland, OH) with 8 Fr (2.67-mm-OD) probe provided non-invasive imaging and measurement of the compressed vessel thickness to confirm consistent pressures and reproducible measurements between samples (Figure 5.2). The OCT probe was placed below the sample and optical window, to image and confirm a consistent compressed vessel thickness of 0.4 mm before tests, and then moved away

before laser activation. The OCT system operated at a center wavelength of 1310 nm, with axial and lateral resolutions of 11 and 25 μm . Images had 1.6 mm and 2.0 mm axial and lateral dimensions. The combined thickness of the compressed tissue (0.4 mm) plus optical window (0.5 mm) was less than the OCT axial scan depth of 1.6 mm, thus enabling precise measurement of the compressed vessel thickness. Vessel burst pressure measurements are also conducted as explained in chapter 3. A successful seal exceeded 360 mmHg, or three times systolic blood pressure (120 mmHg), consistent with industry laboratory destructive testing of vessel seals, *ex vivo*.

5.2.1 Fiber angle polishing

A low-OH, silica optical fiber (FG550LEC-CUSTOM, Thorlabs, Newton, NJ) with 550- μm -core, 600- μm -cladding, 1040- μm -jacket, and numerical aperture (NA) of 0.22, was used for vessel sealing studies. The proximal fiber tip, with high-power SMA905 connector, was attached to the laser. The distal fiber tip was angle polished at 50° using a fiber optic polisher (Radian™, Krelltech, Neptune City, NJ), to achieve side-firing delivery of light at a 90° angle. A value of at least 90% power reflected at a 90° angle was considered to be acceptable. (It should be noted that although integration of a micro-mirror and protective glass dome onto a standard optical fiber with axial delivery of light would produce a superior side-firing spatial beam profile, such commercial fibers are typically 2–3 mm in outer diameter, too large for placement inside the quartz or sapphire optical chambers to be integrated within a fixed jaw for our specific application.)

5.2.2 Bottom jaw assembly

The optical chamber consisted of quartz (Technical Glass Products, Painesville Township, OH) or sapphire (Guild Optical Associates, Amherst, NH) square tubing with dimensions of 1.8×1.8 [mm^2] inner dimensions (ID), 2.7×2.7 [mm^2] outer dimensions (OD), 25 mm length, and 0.45

mm wall thickness (Figure 5.2). A 3D-printed, black resin plug (RS-F2-GPBK-04, Formlabs, Durham, NC) was placed on each end of the optical chamber. The proximal end plug had a small hole to allow insertion of the optical fiber into the chamber. The distal end plug also had a small hole to allow insertion of a thermocouple, but otherwise was designed to provide fluid-tight closure and absorb stray light in the forward direction. The fiber was inserted into the quartz or sapphire tubing and clamped in place using two custom mounts, leaving 0.6 mm between the side-firing silica fiber tip and the inner walls of the tubing. The distance from fiber tip to vessel wall was measured to be 1.05 mm (air gap of 0.6 mm + quartz/sapphire wall thickness of 0.45 mm).

5.2.3 Optical beam characterization (razor blade scans and infrared beam profiler)

Two rail systems (PRL-12, Newport, Irvine, CA) were used with XYZ stages (460A-XYZ, Newport) for beam characterization. On the first rail, the side-firing fiber was clamped into place and the output beam directed towards a detector (PM100-19C, Coherent) connected to a power meter (EPM2000, Coherent). On the same rail was an XYZ stage with a plate holder (FP01, Thorlabs) holding a razor blade. To accurately simulate the distance from the fiber tip to tissue sample, the razor blade was set in front of the fiber, 1 mm from its edge. The back of the blade was 2 mm from the power meter surface. The razor blade was moved across the laser beam in 100 μm increments, and power recorded. The laser was operated at its lowest stable setting ($P = 470$ mW) and power recorded for razor blade beam characterization. An IR beam profiler (Pyrocam III, Spiricon, Logan, UT) was also used to image the beam for qualitative comparison with the razor blade results.

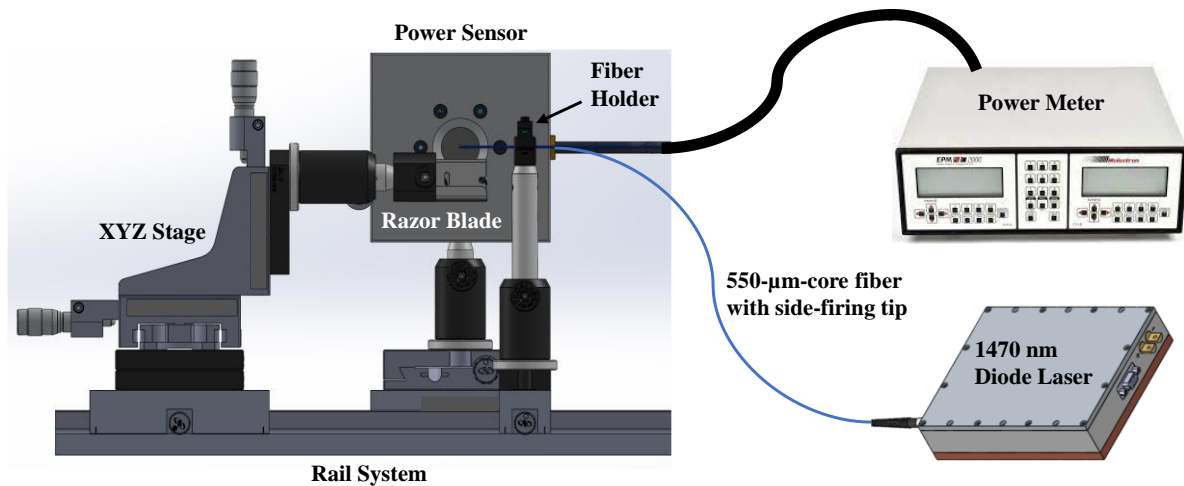


Figure 5.1: Experimental setup for razor blade scans and spatial beam characterization.

5.2.4 Reciprocating fiber experimental setup

Figure 5.1 shows the reciprocating fiber experimental setup. The laser was attached to the fiber with a high- power connector on its proximal end and had a side- firing tip on its distal end. Two custom mounts (not shown) prevented fiber rotation. A micro-controller (Uno, Arduino, Boston, MA) was pre-programmed to a specific scan length (11 mm) and speed (87 mm/s) for the servo motor (SG90, Deegoo-FPV, China). The microcontroller had a custom uploaded code that allowed the motor arm to sweep back and forth over an angle of 45° , in a step-wise manner, with a 2.5 ms delay between each step. This motion of the motor arm translated into the linear, reciprocating motion of the optical fiber, as previously reported [54]. The motor used 4.8 V, giving 1.8 kg cm in stall torque at 0.10 s per 60° . The fiber was threaded through and locked down onto the arm attached to the motor, further preventing fiber rotation. The motor was powered by a battery pack, with a circuit board enabling an external on/off switch. Blood vessels were compressed onto the quartz or sapphire chamber using a glass microscope slide, simulating a transparent active jaw.

5.2.5 Temperature measurements

Two micro-thermocouples (TC) (5TC-TT-T-36-72, Omega, Norwalk, CT) were used: one TC placed on the internal surface of the quartz or sapphire chamber and another TC placed in contact with the chamber's external surface on the opposite side to the exiting laser beam. The TC tip extended 1 mm beyond the plug, within the tubing, but beyond the laser beam path. A computer with temperature software (TracerDAQ + InstaCal, Omega) recorded TC temperatures as a function of time (Figure 5.2).

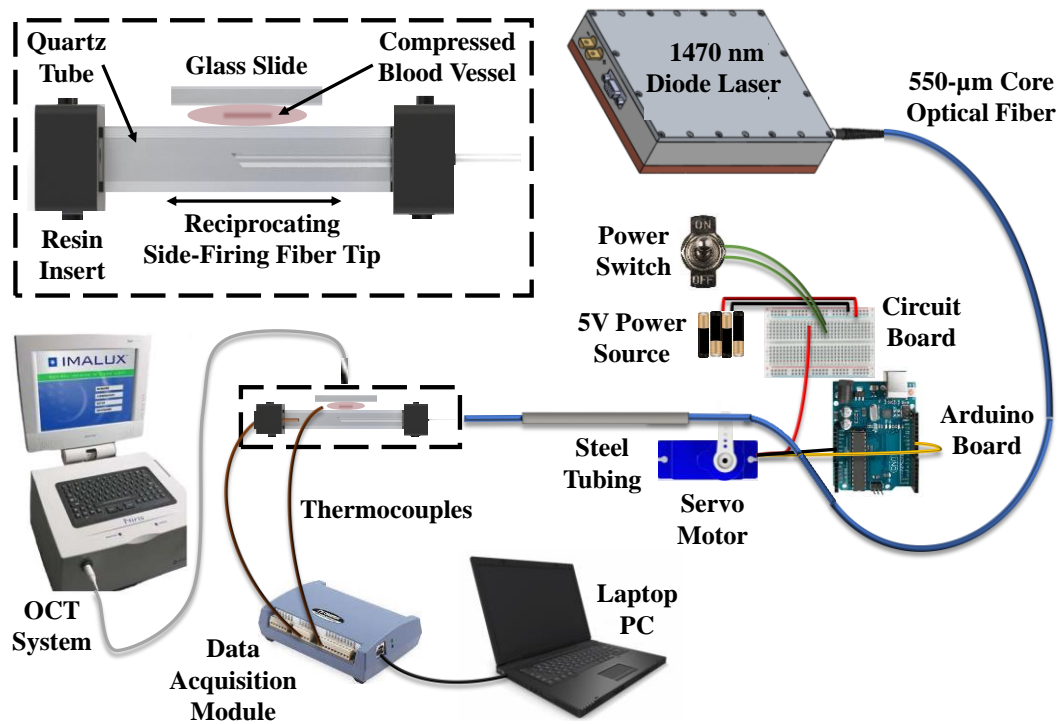


Figure 5.2: The laser was connected to a side-firing fiber. Two mounts (not shown) prevented the fiber from rotating. An Arduino board was pre-programmed to a specific scan length and speed for the servo motor. The fiber was threaded through and locked down onto an arm attached to the servo motor. The servo motor was battery powered, with an external ON/OFF switch. The lower jaw consisted of steel tubing attached to quartz square tubing (25-mm-long with 2.7×2.7 [mm²] outer wall and 1.8×1.8 [mm²] inner wall). Black resin plugs sealed the optical chamber on both the proximal and distal ends, with small holes on each end for insertion of a segment of the optical fiber (without jacket), and insertion of the thermocouple, respectively. The black plug on the distal end additionally served to absorb stray light in the forward direction. Vessel samples were compressed onto the quartz tubing using a glass slide, simulating a transparent upper jaw. (Diagram not drawn to scale)

5.2.7 Statistical analysis

A two-tailed student's t-test was used to determine differences between the quartz and sapphire chamber data groups for the following parameters: vessel diameter, burst pressure, internal peak temperature, external peak temperature, internal cooling time, and external cooling time. A value of $p < 0.05$ was considered to be statistically significant between data sets.

5.3 Computational methods

5.3.1 Optical simulations

Zemax (Ansys, Canonsburg, PA) optical simulation software was used to perform simulations of light transport through both quartz and sapphire optical chambers, using identical dimensions to the experiments (1.8×1.8 [mm²] ID, 2.7×2.7 [mm²] OD, 25 mm length, and 0.45 mm wall thickness). A simple point source option in the Zemax software was used for the simulations (Figure 5.3).

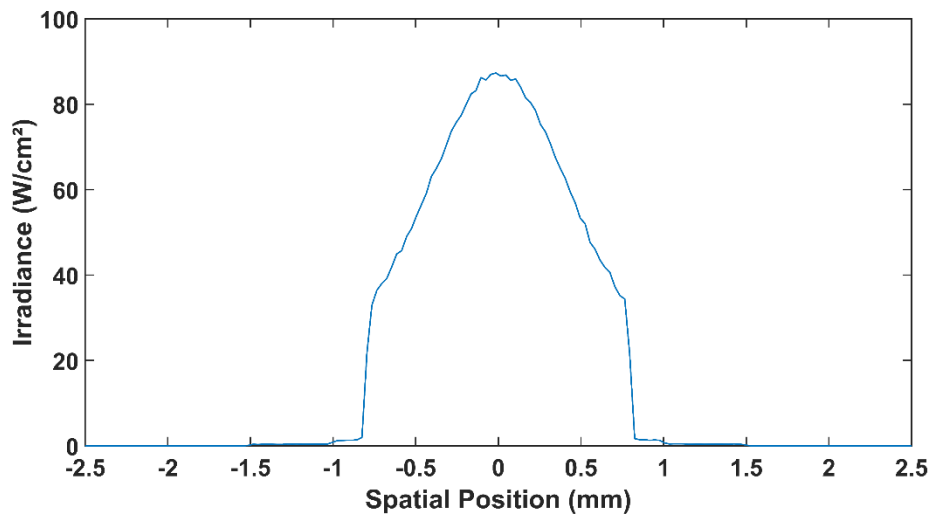


Figure 5.3: The initial laser beam profile exiting the optical fiber, used for both the quartz and sapphire in the Zemax computational simulations.

Monte Carlo (MC) simulations were also performed using Zemax software to simulate the amount of light reflected and scattered back into the quartz chamber. The amount of light reflected is of concern because it may contribute to undesirable heating within the chamber and to higher temperatures on the external surface of the chamber through thermal conduction as well. A Henyey-Greenstein bulk scattering model was used. Values for mean free path, transmission fraction, and anisotropy factor, g , were entered into Zemax for quartz. Mean free path and transmission fraction were calculated using the following formulas:

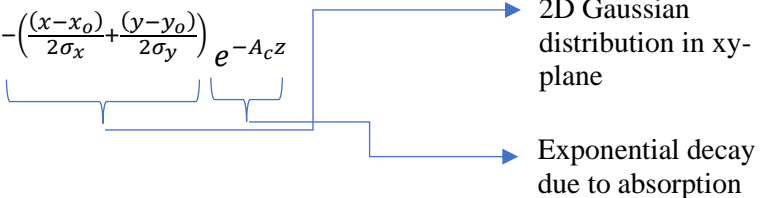
$$\text{Mean free path} = \frac{1}{\mu_a + \mu_s}$$

$$\text{Transmission fraction} = \frac{\mu_s}{\mu_a + \mu_s}$$

The following optical property values at a wavelength of 1470 nm for renal arteries were used, $\mu_s = 267 \text{ cm}^{-1}$, $\mu_a = 20.4 \text{ cm}^{-1}$, and $g = 0.875$, taken from previous literature.[6] Using the formulas above, Mean free path = 0.035 and Transmission fraction = 0.929.

5.3.2 Thermal simulations

COMSOL (Burlington, MA) simulations were performed for thermal analysis of the quartz chamber, using a reflection coefficient of 0.066 (or 6.6%). This value was chosen based on the Monte carlo simulation result, which is consistent with theoretical calculations. The differences in refractive index between quartz ($n_q = 1.445$) and air ($n_a = 1.0$) at 1470 nm [71], which yields a reflection loss of 3.3% per a surface, or a total of 6.6% for two surfaces. The laser heat source in the quartz chamber is provided by the following equation in COMSOL:

$$Q(x, y, z) = \frac{Q_o(1 - R_c)A_c}{\pi\sigma_x\sigma_y} e^{-\left(\frac{(x-x_o)^2}{2\sigma_x^2} + \frac{(y-y_o)^2}{2\sigma_y^2}\right)} e^{-A_c z}$$


2D Gaussian distribution in xy-plane

Exponential decay due to absorption

where,

Q_o = Total input power

A_c = Absorption coefficient

R_c = Reflection coefficient

Moreover, heat flux is

$$Q = h(T_{\text{ext}} - T)$$

where h = heat transfer coefficient of air, which depends on initial material temperature (T) and surrounding medium (e.g. air temperature, T_{ext}) [72]. A quartz chamber was designed in COMSOL. The simulation incorporated a laser beam directed towards the internal bottom surface of the quartz chamber (the surface that the laser beam is incident on). The laser beam was also visible on the top surface of the chamber (the side opposite to the incident laser beam surface) due to reflection from the bottom surface, which enabled tracking of the laser beam movement within the quartz chamber. To simulate the reciprocating motion of the fiber tip within the quartz chamber, the location of the light source was variable only along the y-axis using the interpolation feature in COMSOL, covering a scan length of 11 mm.

5.4 Experimental results

5.4.1 Optical characterization of side-firing fiber

Side-firing optical fibers delivered 94% of light sideways at a 90° angle, with 3.7% in the opposite direction (-90°) and 2.3% in the forward (0°) direction. Total Fresnel reflection losses for the two quartz/air interfaces measured 6%, with 94% of the side-firing light transmitted through the quartz tubing wall. This value of 6% is consistent with the calculated value for Fresnel reflection of 6.6%.

Figure 5.4 shows optical characterization of the IR laser beam exiting the distal, side-firing tip of the 550- μm -core optical fiber. The razor blade scan was performed at a 1 mm distance from the fiber, corresponding to where the blood vessel sample would be located on the external surface of the quartz tubing. The $1/e^2$ beam spot size measured approximately $600\text{ }\mu\text{m} \times 800\text{ }\mu\text{m}$. The IR beam profile was taken at a greater distance due to the limitations of the recessed detector within its window, but also showed a relatively uniform elliptical beam profile in the near field as well. The change in the output beam profile from a mixed modes pattern to an elliptical kind of Gaussian distribution after angle polishing the fiber tip to 50 degrees is likely due to several factors:

- (1) Reduction in higher order modes: Angle polishing can preferentially excite the lower order modes in the fiber, which have a more Gaussian-like intensity distribution. Higher order modes, which contribute to the mixed modes pattern, may be suppressed.
- (2) Improved mode coupling: The angle polishing process may improve the mode coupling efficiency between the input and output modes, leading to a cleaner output beam profile.
- (3) Reduction in cladding modes: Cladding modes, which can contribute to the non-Gaussian output, may be suppressed or filtered out more effectively with the angled polish.
- (4) Alignment of modes: The angled polish may help align the modes more coherently at the output, resulting in a more Gaussian-like profile.
- (5) Reduction in Fresnel reflections: The angled polish can reduce Fresnel reflections at the fiber tip, which can interfere with the mode distribution and lead to non-Gaussian patterns.

Overall, the combination of these effects likely contributes to the observed change in the output beam profile to an elliptical, clean Gaussian distribution after angle polishing the fiber tip to 50 degrees.

Using the beam dimensions measured above, it is possible to estimate the total fluence (J/cm^2) delivered to the tissue by the reciprocating beam. An incident power of 30 W was delivered for 5 s of total laser irradiation time using elliptical beam dimensions of $0.06 \text{ cm} \times 0.08 \text{ cm}$, scanned over a length of 1.1 cm. Given an average uncompressed vessel diameter of 0.32 cm, and a typical 50% increase in vessel width with compression to 0.48 cm [14], yields a correction factor of $(0.48/1.1)$, or 0.44. The rectangular beam area for the entire scan length is given by the width of the beam (0.08 cm) times the length of the scan (1.1 cm), or 0.088 cm^2 . Hence, the total fluence delivered to the tissue sample is given by $F = [(0.44) (30 \text{ W}) (5 \text{ s})]/0.088 \text{ cm}^2 = 750 \text{ J}/\text{cm}^2$.

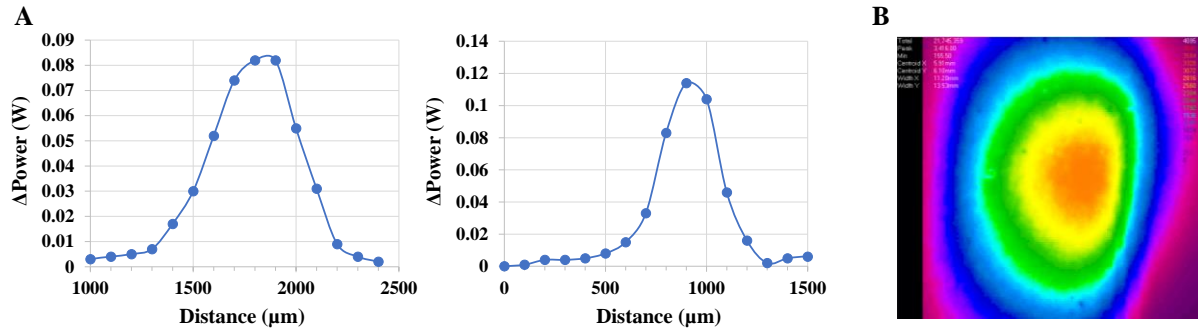


Figure 5.4: (A) Razor blade scans of output spatial beam profile in two orthogonal directions; (B) Image from IR beam profiler.

5.4.2 Thermal characterization of quartz and sapphire chambers

Table 5.1 summarizes the temperatures measured by the two thermocouples (one each on the internal and external surfaces of the quartz or sapphire chambers). The maximum temperatures measured on the internal surface of the quartz chamber ($45.4 \pm 5.8^\circ\text{C}$) were significantly lower than on the external surface ($73.8 \pm 8.4^\circ\text{C}$) ($P = 2\text{E-}4$). The maximum temperatures measured on the internal surface of the sapphire chamber ($66.1 \pm 15.5^\circ\text{C}$) were not significantly different than on the external surface of the sapphire chamber ($72.8 \pm 9.8^\circ\text{C}$) ($p = 0.20$). There was also no significant difference between the external temperatures for the quartz and sapphire chambers (p

= 0.78). However, the largest difference between the quartz and sapphire chamber studies was found in the cooling times. The cooling times for the external surface of the chamber are of interest, since these cooling times determine how long the surgeon must wait in between successive activations of the IR laser sealing device. This pause in the procedure is necessary to prevent

thermal build-up and associated damage to adjacent tissues through accidental contact with the overheated device in the confined anatomical spaces commonly encountered during laparoscopic surgery. The external surface of the quartz chamber cooled down to body temperature (37°C) in 13 ± 4 s, while the external surface of the sapphire chamber required twice as long to cool down, at 27 ± 7 s ($P= 1E-6$). There was an even larger difference in cooling times for the inside of the quartz and sapphire chambers, 4.2 ± 3.8 s and 40.0 ± 3.8 s, respectively ($P= 1E-18$), presumably due to thermal buildup inside the sapphire chamber from higher Fresnel reflection losses of light at the air/sapphire interface. Figure 5.5 shows representative temperature–time data for TCs placed on the internal and external surfaces of the quartz and sapphire optical chambers.

Table 5.1: Thermocouple (TC) temperatures (°C) measured on the quartz (Q) and sapphire (S) chamber internal and external surfaces, for fixed laser parameters of 30 W for 5 s, as well as times necessary for the jaw to cool down to body temperature between applications

	T₀ (°C)	T_{max} (°C)	ΔT (°C)	Cooling time (s) to 37 °C	Sample Size (n)
Q: TC1 (inside)	21.9 ± 0.2	45.4 ± 5.8	23.5 ± 5.8	4.2 ± 3.8	13
Q TC2 (outside)	21.0 ± 0.3	73.8 ± 8.4	52.8 ± 8.5	12.7 ± 4.3	13
S: TC1 (inside)	21.3 ± 0.4	66.1 ± 15.5	44.7 ± 15.5	40.0 ± 3.8	14
S: TC2 (outside)	21.4 ± 0.4	72.8 ± 9.8	51.4 ± 10.0	26.9 ± 6.6	14

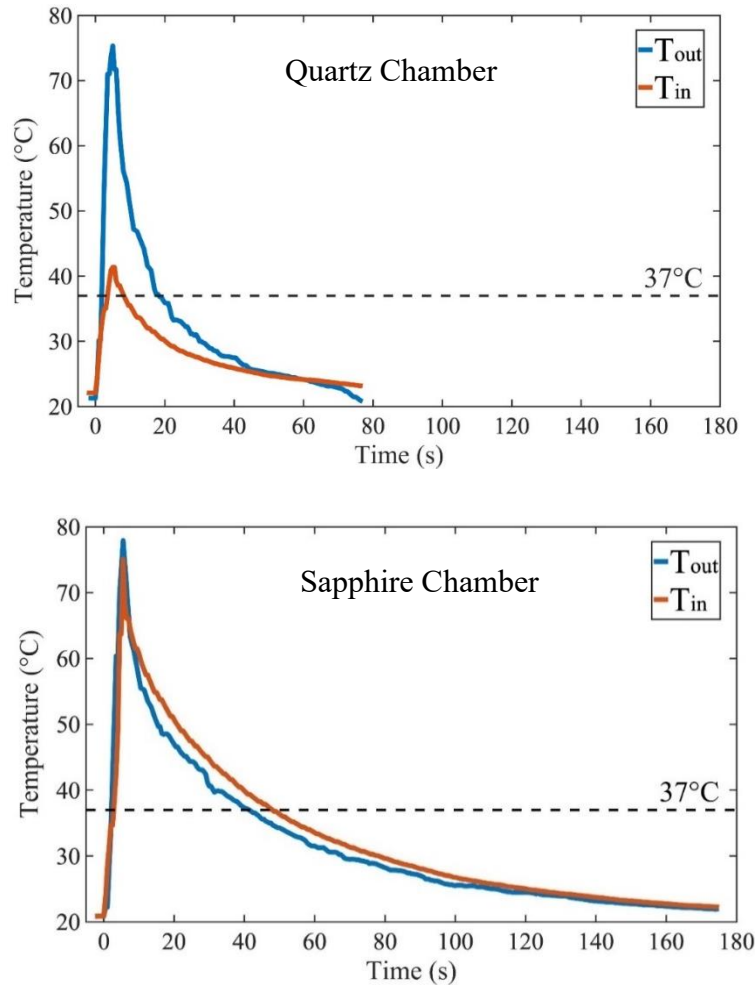


Figure 5.5: Representative thermocouple temperature measurements on the internal (T_{in}) and external (T_{out}) surfaces of the quartz and sapphire optical chambers, as a function of time. All vessel sealing studies were performed with an incident laser power of 30 W at the tissue surface and a laser irradiation time of 5 s, at an infrared wavelength of 1470 nm.

5.4.3 Vessel burst pressures

For the quartz chamber, vessel BP averaged 883 ± 393 mmHg, with 13/13 vessels (100%) achieving successful BPs above 360 mmHg. For the sapphire chamber, vessel BPs measured 412 ± 330 mmHg, with only 10/14 vessels (64%) sealed successfully (Table 5.2). This difference in burst pressures was statistically significant ($p = 0.003$). Figure 5.6 shows a scatter plot of BPs as a function of vessel diameter for quartz and sapphire chambers. As mentioned in chapter 4, it is common to observe a wide range of vessel burst pressures for successful seals during laboratory

testing with all energy-based devices (RF, US, and laser), due in part to differences among samples in vessel diameter, collagen/elastin content, attached fatty tissue layers, and water content. However, it is interesting to observe that as vessel diameter increases, the BPs achieved using the quartz chamber trend higher, while BPs for the sapphire chamber trend lower. The decreasing trend in BPs for larger vessels treated with the sapphire chamber can be explained by observed incomplete, less than full thickness seals, due to more significant heating on the front surface of the vessel sample. Thermal coagulation of soft tissues is well known to result in dynamic changes in the optical properties of tissues, specifically an increase in light scattering, which in turn results in decreased optical penetration depth and an even steeper temperature gradient with depth. The vessel sealing process for the sapphire chamber may therefore be dominated by thermal conduction from the front surface of the chamber, rather than uniform deposition of optical energy into the tissue, with this effect enhanced by the higher thermal conductivity for sapphire than quartz, as discussed further below.

Figure 5.7 shows representative blood vessels after laser treatment, for quartz and sapphire chambers. A relatively uniform and well delineated zone of thermally coagulated tissue is observed on both the front and back surfaces of blood vessels successfully sealed using both the quartz and sapphire optical chambers. However, in the vessels that failed using the sapphire chamber, as determined by low burst pressures (<360 mmHg), an incomplete thermal coagulation zone is observed on the back side of the vessel, indicating a less than full thickness seal.

Table 5.2: Statistical comparison of results for quartz and sapphire optical chambers, with laser incident power at the tissue surface of 30 W and irradiation time of 5 s. Statistical significance between quartz and sapphire is denoted by an asterisk (*).

Property	Quartz	Sapphire	P-value
Uncompressed vessel diameter (mm)	3.4 ± 0.7	3.2 ± 0.7	$P = 0.41$
Cooling times to 37 °C (s)*	12.7 ± 4.3	26.9 ± 6.6	$P = 1\text{E-}6$
Burst pressure (mmHg)*	883 ± 393	412 ± 330	$P = 0.003$
Seal Success Rate	13/13 (100%)	9/14 (64%)	

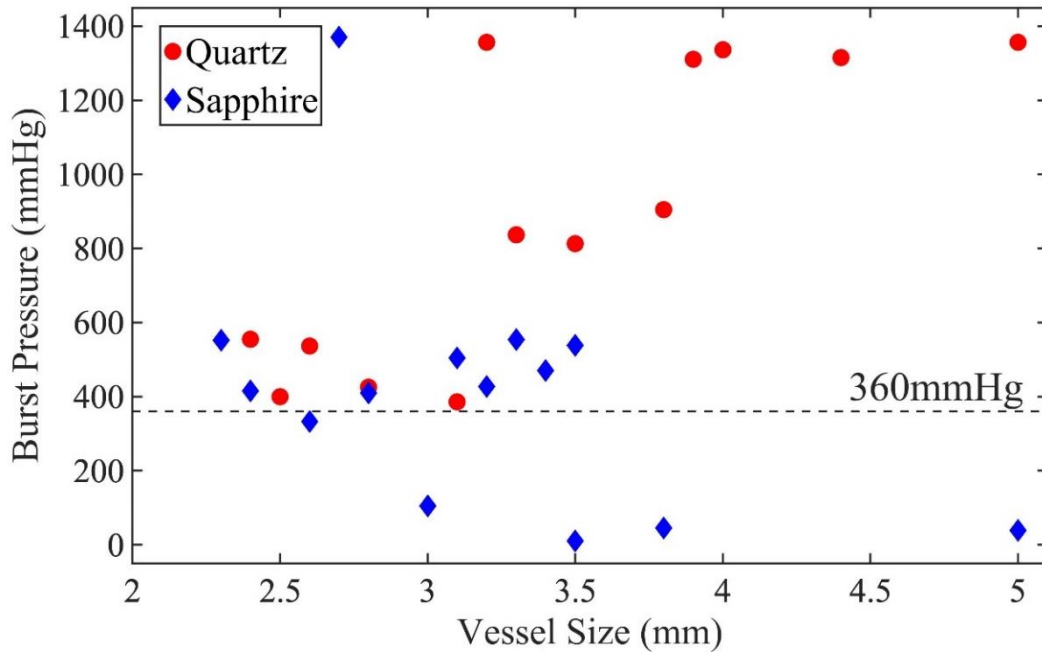


Figure 5.6: Blood vessel burst pressures (BP) as a function of vessel diameter for the quartz and sapphire optical chambers. The dashed horizontal line shows the industry standard threshold of 360 mmHg (three times systolic blood pressure) for designation of a successful seal. For the quartz chamber, vessel BP averaged 883 ± 393 mmHg, with 13/13 vessels (100%) recording BPs above 360 mmHg. For the sapphire chamber, vessel BPs measured 412 ± 330 mmHg, with 10/14 vessels (64%) sealed.

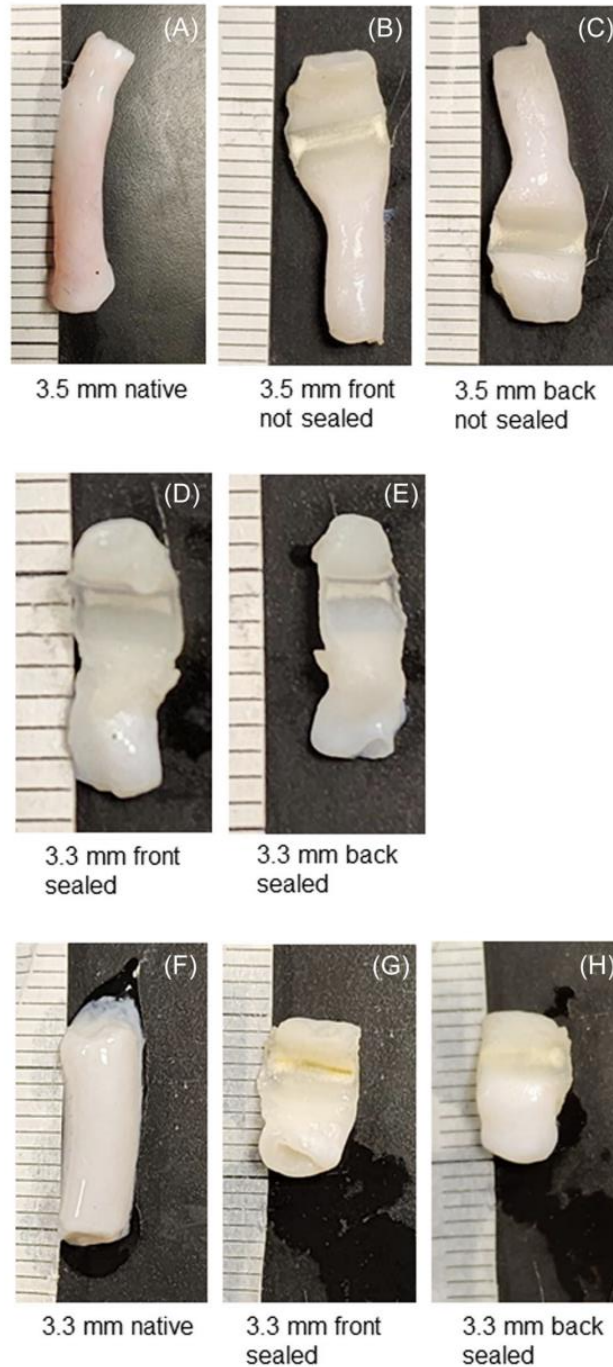


Figure 5.7: Photographs of the vessels before and after sealing for sapphire and quartz. (A–C) A 3.5 mm diameter vessel in its native state, as well as after it was sealed unsuccessfully using the sapphire chamber, showing its front side, and back side, respectively. (D, E) A 3.3 mm diameter vessel, showing its front and back sides, respectively, after a successful seal ($BP = 554 \text{ mmHg}$) using the sapphire chamber. (F–H) A 3.3 mm diameter vessel in its native state, as well as after it was sealed successfully ($BP = 776 \text{ mmHg}$) using the quartz chamber, showing its front side and back side, respectively. All vessels sealed with the quartz chamber were successful. An incomplete zone of the thermal coagulation on the backside of the vessel is observed for the failed seal using the sapphire optical chamber in image (C).

5.5 Computational results

5.5.1 Optical simulations

The spatial distribution of the laser beam exiting the chamber for quartz and sapphire is simulated in Figure 5.8. The quartz chamber had curved edges, based on the commercial availability of square quartz tubing, while the sapphire chamber was assembled from four individual optical windows, resulting in straight edges, due to the lack of commercial availability for square sapphire tubing. The wider output beam profile of quartz (3.2 mm) compared to sapphire (2.5 mm) is responsible for the larger thermal seal zone observed with the quartz chamber in experiments. This is of potential future interest because the larger seal zone (with higher irradiance in center) may enable simultaneous bisection of the vessel and thermal sealing (from lower irradiation at the ends), in a one-step process. When using a sapphire chamber with a smaller output beam profile, the seal zone was narrower, which may prohibit simultaneous bisection/sealing of vessels. The simulations also explain the narrow carbonization zone at the center of the seal using a quartz chamber. The small peaks in the output beam profile for the sapphire tubing are due to the refraction of light rays at the straight corners of the tubing.

In the computational setup for the Monte Carlo simulations (Figure 5.9), two detectors (inside and outside the quartz chamber) were strategically positioned to simulate power leaving the tissue and power re-entering the chamber, due to Fresnel reflections and diffuse reflection (back-scattered photons). A 30 W point light source was used for simulations, similar to experiments, and 1 million rays were launched into the tissue. The external detector in the simulations recorded 2.63 W, or 8.7% of input power, while the internal detector recorded 1.97 W, or 6.6% of input power. These

simulation results were consistent with predominantly forward-scattering behavior of tissue that has a high anisotropy factor ($g = 0.875$).

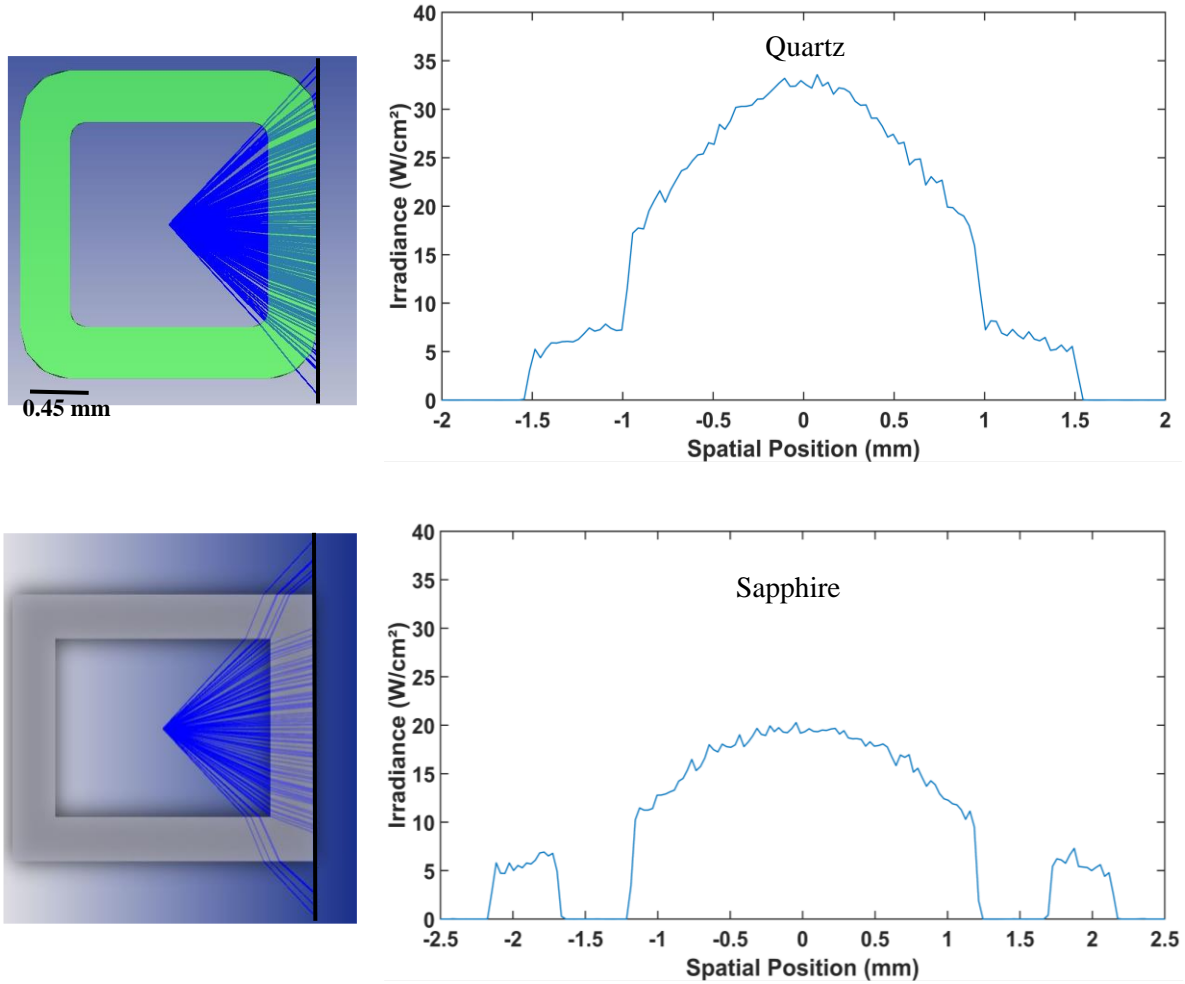


Figure 5.8: Ray tracing showing both (left column) beam divergence through the optical chamber and (right column) output beam profile, for both quartz (top row) and sapphire (bottom row), using Zemax optical software. The location of the detector surface in the simulations is denoted by a vertical black line on the right edge of each optical chamber. Note that the quartz chamber had curved edges, due to commercial availability of square quartz tubing, while the sapphire chamber was assembled from four individual optical windows, resulting in straight edges, due to the lack of commercial availability for square sapphire tubing.

5.5.2 Thermal simulations

For the thermal simulations in COMSOL, a domain point temperature probe was placed on the top surface within the scan length of the light source to measure the temperature along the scan length

of the fiber tip on the top surface. After 5 s, the laser source was turned off, similar to experiments, but the simulation continued recording surface temperatures of the quartz chamber until body temperature (37°C) was reached. Convective cooling from air played a major role in lowering the quartz chamber's temperature. Figure 5.10 shows images of the quartz chamber design and simulation results at several time points ($t = 0, 3.25, 5$, and 22 s).

Simulated results for the temperature–time response on the external surface of the quartz chamber are shown in Figure 5.11. The highest temperature was 351 K (77.85°C), with cooling time of 16 s to reach body temperature (37°C), consistent with the experimental results. The quartz chamber experienced a sharp temperature decrease after 5 s when the laser was de-activated, due to efficient heat transfer between the quartz wall and air, facilitated by the temperature gradient. As the quartz wall temperature approached ambient air temperature, the rate of heat transfer decreased, due to the reduced temperature difference between the two mediums.

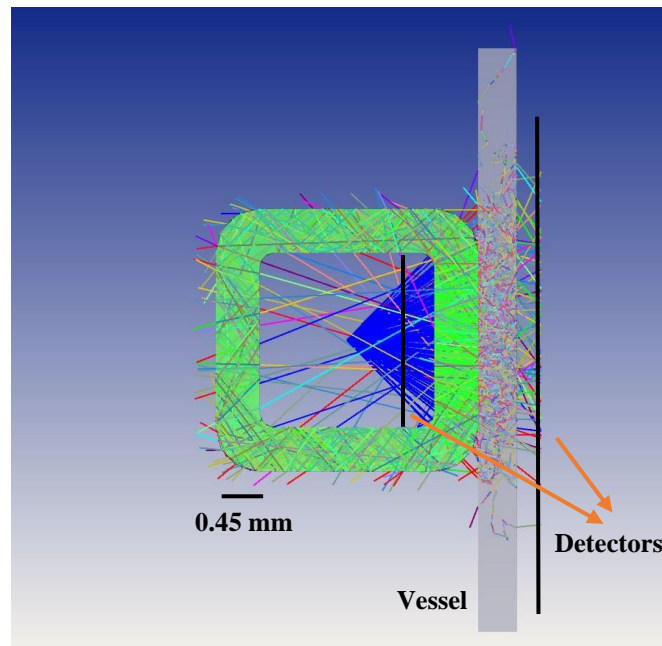
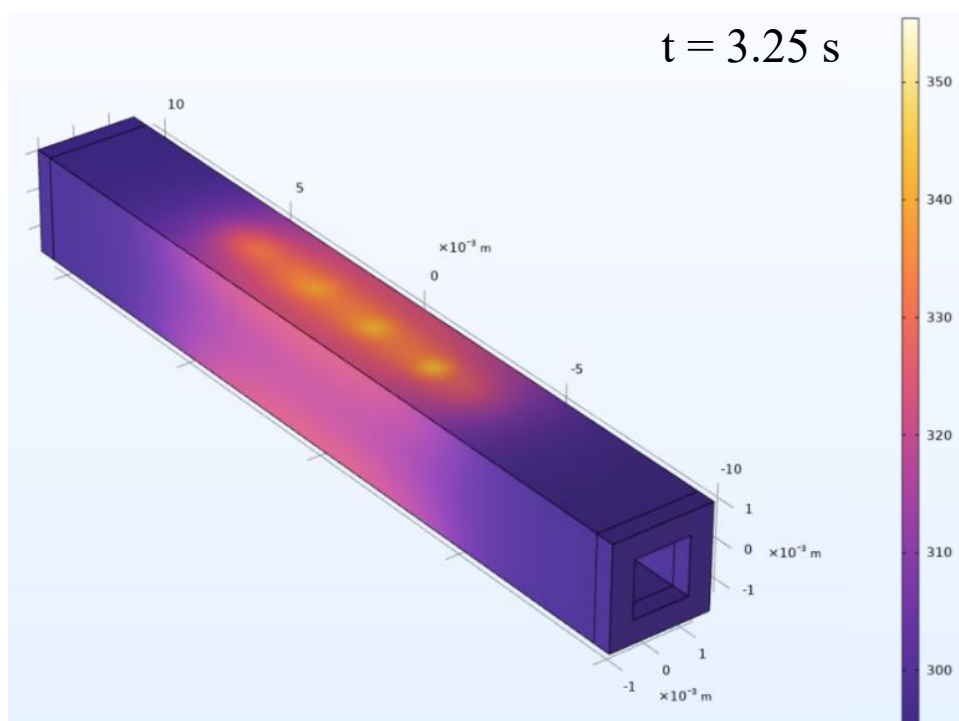
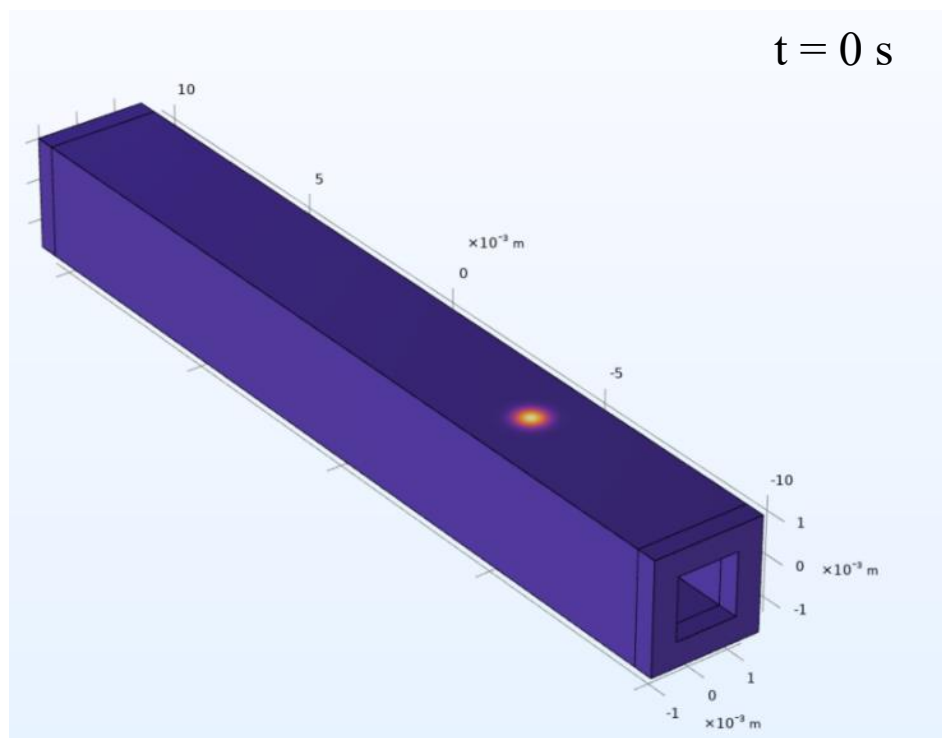


Figure 5.9: Monte Carlo simulations showing light transport through the quartz chamber (green) and into the tissue layer (gray). A total of 1 million light rays were used in the simulations, with 8.7% of the light rays transmitted through the tissue layer, 6.6% percent of the light rays reflected back into the chamber, and the remaining 84.7% of the light rays absorbed in the tissue.



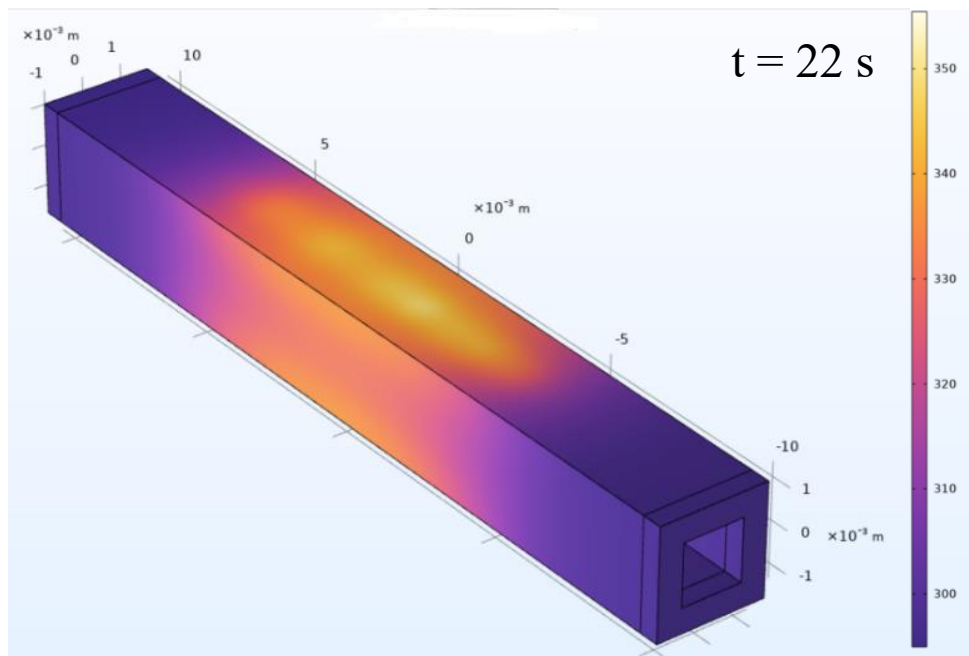
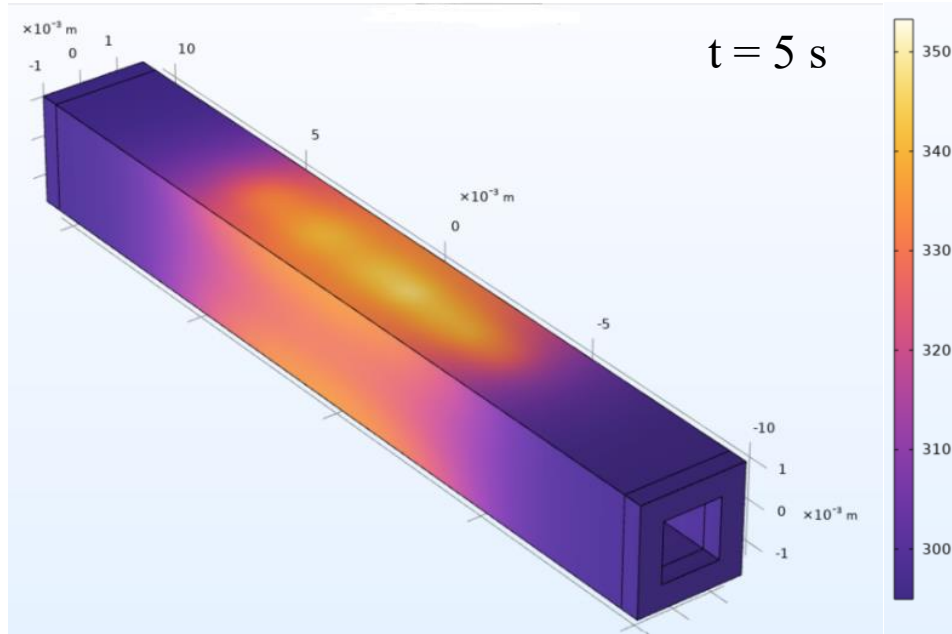


Figure 5.10: COMSOL thermal simulations showing the temperature profile on the external surface of the quartz chamber (with plugs inserted on both ends) at different time points of $t = 0$ s (start of laser irradiation), $t = 3.25$ s (during laser irradiation), $t = 5$ s (after laser de-activated), and $t = 22$ s (after 16 s of cooling).

The temperature plot in Figure 5.11 shows multiple peaks and valleys at specific time intervals. When the sensor and reciprocating laser beam locations coincided, a temperature peak resulted due to localized thermal accumulation. When the laser beam was further away from the sensor, the temperature decreased. As the sensor recorded the temperature measurement when the laser and sensor are again at the same location, subsequent temperature peaks continued to increase due to thermal buildup from previous laser heating. Furthermore, the absence of peaks and valleys in the data during the cooling phase also suggests that these fluctuations arise from interplay between the sensor and reciprocating laser beam during data acquisition.

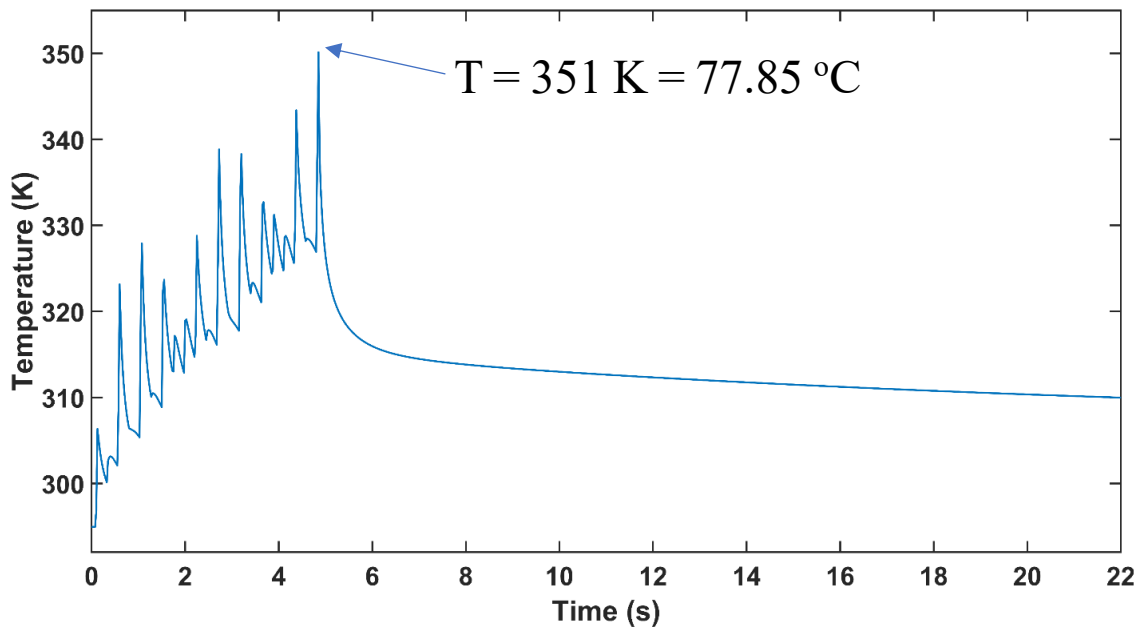


Figure 5.11: External temperature (in Kelvin) of the quartz chamber as a function of time. Laser is activated at $t = 0$ s and de-activated at $t = 5$ s. The highest temperature was 351 K (77.85°C), with cooling time of 16 s to reach body temperature (37°C), consistent with experimental results.

5.6 Discussion

This study tested quartz, an inexpensive, readily available, and optically transparent material for the optical chamber. Quartz was compared with sapphire, which is also frequently used as a component in medical optical devices, due to its optical transparency in the IR spectrum, higher melting temperature, and higher thermal conductivity (Table 5.3) [71][73].

Preliminary results demonstrated a fundamental trade-off between the optical and thermal properties when comparing quartz and sapphire. Sapphire is more robust and provides higher thermal conductivity, but at an added expense (sapphire tubing costs about ten times more than quartz tubing) and a higher refractive index ($n_s = 1.76$ vs. $n_q = 1.45$), thus leading to greater Fresnel reflection losses.

Table 5.3: Statistical comparison of results for quartz and sapphire optical chambers, with laser incident power at the tissue surface of 30 W and irradiation time of 5 s. Statistical significance between quartz and sapphire is denoted by an asterisk (*).

Property	Quartz	Sapphire
Optical transmission range (nm)	240 - 2500	150 - 5000
Refractive index, n	1.45	1.76
Reflection losses at air/medium interface (%)	3.3	7.4
Glass transition or melting temperature ($^{\circ}\text{C}$)	1200	2000
Thermal conductivity ($\text{W/m}^{\circ}\text{C}$)	1.4	32
Thermal expansion coefficient ($10^{-6}/^{\circ}\text{C}$)	0.55	5
Density (10^3 kg/m^3)	2.2	4.0
Young's modulus (GPa)	72	435

This refractive index difference translated into over two times greater reflection on the internal surface of the sapphire chamber than for the quartz chamber (7.4% vs. 3.3%). This effect in turn resulted in more heat trapped within the chamber, leading to more thermal buildup (higher peak temperatures) inside the chamber and consequently longer cooling times as well (Table 5.1). The optical reflection losses were not offset by sapphire's significantly higher thermal conductivity ($K_s = 32 \text{ W/m}^\circ\text{C}$ vs. $K_q = 1.4 \text{ W/m}^\circ\text{C}$) [71][73]. The higher thermal conductivity appears to have contributed to rapid thermal coagulation on the front side of the blood vessels, resulting in higher light scattering, decreased optical penetration depth, and consequently a steeper temperature gradient. This effect in turn translated into incomplete, less than full thickness seals, with correspondingly lower vessel burst pressures measured (Table 5.2).

It should be briefly noted that the values given for Fresnel reflection losses for both quartz and sapphire above assume normal incidence of the light rays (90°), a simplistic assumption, given that the light beam exiting the fiber is divergent ($NA = 0.22$) when incident on the quartz or sapphire chamber wall. Therefore, total Fresnel reflection losses reported here are minimum values, and are in reality much higher. Nevertheless, the significant difference in amount of reflected light between air/quartz and air/sapphire interfaces remains. The high Fresnel reflections and thermal conductivity of sapphire are responsible for the higher temperatures and longer cooling times inside the sapphire chamber, observed in the experiments.

There were concerns with self-heating of the thermocouples by the reflected laser light trapped within the optical chamber resulting in erroneous temperature values. However, these concerns were not realized, based on the close agreement observed in both peak temperatures and cooling times between the experimental and computational results. One potential novel approach to reducing Fresnel reflection and associated thermal buildup within the optical chamber may be

application of antireflection structured surfaces (ARSS) to the internal surface of the quartz or sapphire chamber [74–76]. These ARSS have been reported to have significantly higher damage thresholds than AR coatings, for use in high power laser applications. However, the additional cost and complexity of ARSS may make this approach impractical for single-use disposable medical products, such as energy-based vessel sealing surgical devices. The ARSS are also delicate and thus may be subject to damage from accidental contact with the fiber inside the optical chamber and/or constant contact with the tissue sample outside the chamber.

Regardless, the peak external chamber temperatures (74°C) and cooling times (13 s) reported in this study using a quartz chamber appear promising, especially when directly compared with those values previously reported for conventional electrosurgical (radiofrequency) and ultrasonic surgical devices in current clinical practice [77–79]. For example, a recent study reported that maximum external jaw temperatures ranged from 94°C to 133°C for RF devices and 81°C–350°C for US devices [80]. The cooling time for the quartz chamber also compares favorably with recently reported average cooling times of 54 s and 68 s for two different RF devices [81]. Furthermore, peak temperatures and cooling times for quartz may be reduced even further by more closely matching the fiber reciprocating scan length to the compressed vessel width in future studies. Several limitations of this preliminary study include (1) the difference in curvature in the corners of the quartz and sapphire tubing, based on limited commercial availability of the optical materials, (2) ex vivo tissue temperature measurements performed at room temperature as opposed to body temperature, (3) use of a fixed fiber reciprocating length to provide consistent scientific data using similar parameters for both quartz and sapphire, (4) the need to develop a fully functional active jaw for providing tissue compression in future engineering prototypes, and (5) the focus on vessel sealing as a first step before bisection of vessels can be

implemented as a second step. Nevertheless, in summary, this study demonstrated that a quartz optical chamber performed better than a sapphire chamber and conventional RF and US vessel sealing devices as well, in terms of providing lower peak temperatures and shorter cooling times, which are both critical indicators for safe and efficient clinical procedures.

5.7 Conclusion

Optical and thermal measurements were conducted comparing transparent quartz and sapphire chambers for IR laser sealing of vascular tissues. Total Fresnel reflection losses for the two material-air interfaces measured 6.6% and 14.8%, for quartz and sapphire, respectively. Peak quartz temperatures on the external surface of the quartz chamber averaged 74°C, with a time of only 13 s to cool to body temperature, compared to a cooling time of 27 s for sapphire. Computational simulations of the optical-thermal response for the quartz chamber produced peak temperatures and cooling times consistent with the experimental results. Quartz provides better optical and thermal results for use as an optical chamber than sapphire, as demonstrated by these lower Fresnel reflections, lower chamber internal temperatures, and shorter cooling times. The use of a transparent chamber will improve visibility, thus enabling more accurate visualization and placement of variable sized vessels within the device jaws for custom procedures. Future work will focus on integration of the quartz chamber into a fully functional laparoscopic device for preclinical studies.

Chapter 6 : SIMULTANEOUS SEALING AND BISECTION OF PORCINE RENAL BLOOD VESSELS, *EX VIVO*, USING A CONTINUOUS-WAVE, INFRARED DIODE LASER AT 1470 NM

6.1 Introduction

Previous experimental studies also demonstrated rapid and precise sealing and bisection of blood vessels, *ex vivo*, in a two-step, sequential approach [30]. However, the large benchtop system used standard bulk optics, which are not practical for future laparoscopic surgery in animal studies, *in vivo*. Quartz proved to be a better option as a material for transparent laparoscopic jaws as observed in chapter 5. Hence, this study utilizes a compact, square quartz optical chamber (2.7 x 2.7 x 25 mm OD). The main objectives of this chapter are two-fold, (1) to investigate the feasibility of simultaneous IR laser vessel sealing and bisection in a one-step approach, using a quartz optical chamber suitable for integration into a laparoscopic device, and (2) to test the feasibility of using the optical signal originating from the therapeutic laser and transmitted through the cut vessel, as a closed-loop, optical feedback system for immediately deactivating the IR laser upon successful vessel bisection.

6.2 Methods

6.2.1 Simultaneous vessel sealing and bisection studies

Fresh porcine kidney pairs were acquired as explained in chapter 3. A total of n=10 blood vessels, each with a similar uncompressed mean diameter of 3.2 ± 0.5 mm, 3.4 ± 0.6 mm, 3.4 ± 0.8 mm, and 3.3 ± 0.7 mm, were selected for each group of four laser power settings (41, 47, 53, and 59 W), respectively ($P = 0.84$).

A 100-Watt, 1470-nm wavelength IR diode laser (BrightLase, QPC Lasers, Sylmar, CA) was used for the vessel sealing studies. The laser was operated in continuous-wave (CW) mode with incident power of 41, 47, 53, and 59 W and irradiation time ranges of 20-21, 15-17, 10-11, and 5-6 s, respectively. Laser power output was calibrated using a power meter (EPM1000, Coherent, Santa Clara, CA) and detector (PM-150, Coherent). A high-power fiber optic shutter (SH-200-55-1470-M-O-T-BH-SP, Oz Optics, Ottawa, Canada) was connected by a fiber optic patch-cable on one end to the laser diode module, and the other end to a surgical fiber (Figure 1). The shutter enabled ramp up of the laser power output prior to initiating the procedure as well as stable power output during laser irradiation.

Blood vessel samples were compressed and fixed in place using a 0.5-mm-thick optical window locked in a clamp, to simulate a transparent surface for the upper jaw (Figure 1). An optical coherence tomography (OCT) system (Niris, Imalux, Cleveland, OH) with 2.7-mm-OD probe provided non-invasive measurement of the compressed vessel thickness to confirm consistent pressures and reproducible measurements between samples. Compressed tissue thickness was fixed at 0.4 mm to closely match the optical penetration depth of IR light in water-rich soft tissues at 1470 nm, and to provide uniform, full-thickness seals. The OCT probe was placed next to the sample and optical window, to non-invasively image the tissue thickness, and then moved away before laser activation. The OCT system operated at 1310 nm, with axial and lateral resolutions of 11 and 25 μm . Images had 1.6 mm and 2.0 mm axial and lateral dimensions. The combined thickness of the compressed tissue (0.4 mm) plus optical window (0.5 mm) was less than the OCT axial scan depth of 1.6 mm, allowing measurement of compressed vessel thickness.

A low-OH, silica optical fiber (FG550LEC-CUSTOM, Thorlabs, Newton, NJ) with 550- μm -core, 600- μm -cladding, 1040- μm -jacket, and numerical aperture of 0.22 was used. The proximal fiber tip with high-power SMA905 connector was attached to the shutter. The side-firing, angled distal fiber tip was prepared using a fiber optic polisher (Radian™, Krelltech, Neptune City, NJ), to achieve a 50° polish angle and 90° light delivery as explained in chapter 5 in detail. The output of the fiber was observed again using a beam profiler and by performing the razor blade scans in order to confirm the same output profile as observed in chapter 5.

It was made sure to keep the set up same as in comparison studies in the previous chapter. The optical chamber consisted of quartz (Technical Glass Products, Painesville Township, OH) square tubing with dimensions of 1.8 x 1.8 mm ID, 2.7 x 2.7 mm OD, 25 mm length, and 0.45 mm wall thickness. A 3D-printed, black resin plug (RS-F2-GPBK-04, Formlabs, Durham, NC) was placed on each end of the chamber (Figure 1). The proximal plug had a small hole to allow insertion of the fiber. The distal plug also had a small hole to allow insertion of a thermocouple (TC), but otherwise provided fluid-tight closure and absorbed stray light in the forward direction. The fiber was inserted into the quartz tubing and clamped in place, leaving a 0.6 mm space between the fiber tip and the inner walls of the tubing. The distance from fiber tip to vessel wall measured 1.05 mm (air gap of 0.6 mm + quartz wall thickness of 0.45 mm). Figure 6.1 shows the reciprocating, side-firing, fiber experimental setup. A high-power connector on the proximal fiber end was attached to the shutter. Two custom mounts (not shown) and steel tubing prevented the fiber from rotating and becoming misaligned. A micro-controller (Uno, Arduino, Boston, MA) was pre-programmed to a specific scan length (11 mm) and speed (87 mm/s) for the servo motor (SG90, Deegoo-FPV, China). The microcontroller had a custom uploaded code that allowed the stepper motor to sweep back and forth over an angle of 45° with a 2.5 ms delay between steps.

The motor used 4.8 V, giving 1.8 kg-cm in stall torque at 0.10 s per 60°. The fiber was threaded through and locked down onto an arm attached to the motor. The motor was powered by a battery pack, with a circuit board enabling an external on/off switch. Blood vessels were compressed onto the quartz chamber using a glass microscope slide as an optical window, simulating a transparent surface for the upper jaw. Two micro-thermocouples (5TC-TT-T-36-72, Omega, Norwalk, CT) with 125- μ m-OD were used: one TC was placed inside the quartz and another TC placed in contact with the chamber's external surface on the opposite side to the exiting laser beam. The TC tip extended 1 mm beyond the plug, within the tubing, but beyond the laser beam path. A personal computer with temperature software (TracerDAQ + InstaCal, Omega) recorded TC temperatures as a function of time (Figure 6.1).

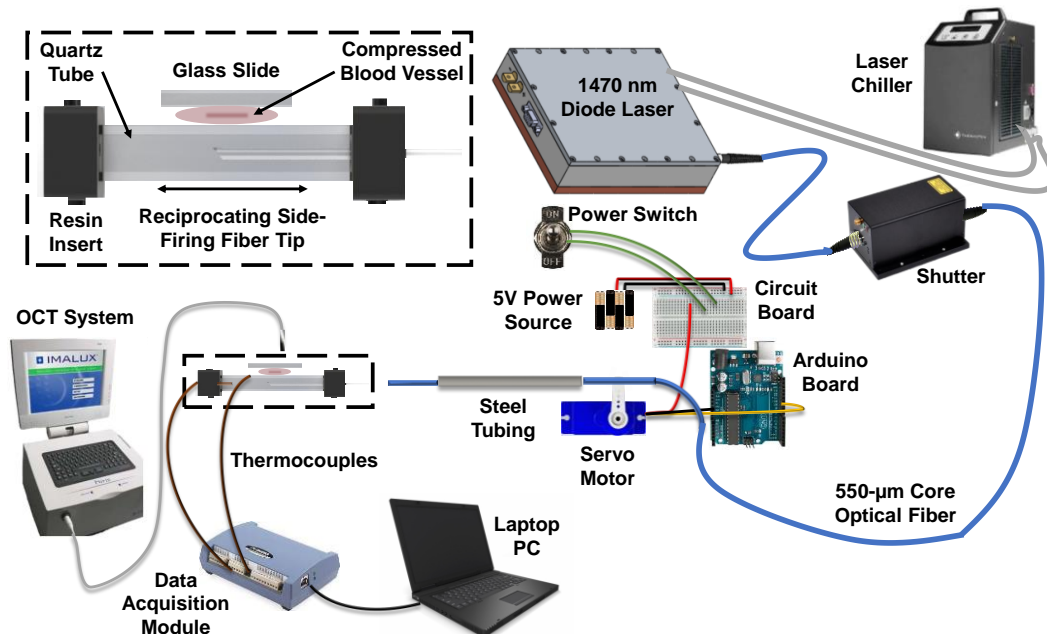


Figure 6.1: The laser was connected to a side-firing fiber. Two mounts (not shown) prevented the fiber from rotating. An Arduino board was pre-programmed to a specific scan length and speed for the servo motor. The fiber was threaded through and locked down onto an arm attached to the servo motor. The servo motor was battery powered, with an external ON/OFF switch. The lower jaw consisted of steel tubing attached to quartz square tubing (25-mm-long with 2.7 x 2.7 mm OD and 1.8 x 1.8 mm ID). Black resin plugs sealed the optical chamber on proximal and distal ends, with small holes on each end for insertion of the bare optical fiber (with jacket removed), and insertion of the micro-thermocouple, respectively. The black plug on the distal end additionally served to absorb stray light in the forward direction. Vessel samples were compressed onto the quartz tubing using a glide slide, simulating a transparent upper jaw.

Vessel burst pressure measurements are conducted as explained in chapter 3. A successful seal exceeded 360 mmHg, or three times systolic blood pressure (120 mmHg), consistent with industry laboratory destructive testing of vessel seals, *ex vivo*.

6.2.2 Optical feedback system

A similar 550- μm -core optical fiber as for the IR laser sealing/cutting experiments, was also used for optical transmission measurements, but the bare distal fiber tip was instead polished flat. A total of 8 blood vessels ($d = 3.1 \pm 0.6 \text{ mm}$) were tested. The IR laser was operated in CW mode at an incident power of 6.5 W, producing a circular beam diameter of 0.560 mm, and yielding an irradiance of 26.4 W/mm^2 or 2640 W/cm^2 , at the vessel surface. The working distance between the fiber tip and tissue surface was kept fixed at 1.3 mm. The tissue was compressed between two acrylic windows to a 0.4 mm thickness. A 1.5-mm-diameter hole was drilled in the center of each acrylic window, to enable the optical signal to be transmitted directly through the tissue to the detector, without additional Fresnel reflection losses.

Figure 6.2 shows the experimental setup. The optical transmission signal was acquired by an InGaAs photodiode detector (PDA400, Thorlabs) connected to an oscilloscope (TDS 2002b, Tektronix, Beaverton, OR). A neutral density filter (not shown) with an optical density of 4.0 (NE40, Thorlabs) was placed between the tissue and photodetector to attenuate the signal and protect the photodetector. An iris (SM1D12C, Thorlabs) with 1.5-mm-diameter opening was also placed in front of the photodetector to reduce contributions from multiple scattered light to the transmission signal (Figure 2). The laser was de-activated once the oscilloscope signal saturated, corresponding to an ablated hole in the tissue. A compact camera (AF4915ZT, Dino-lite, Torrance, CA) recorded video of each experiment.



Figure 6.2: Experimental setup for acquiring the optical transmission signal during continuous-wave laser ablation of compressed porcine renal blood vessels. (Left top inset) Start of formation of a carbon layer on the tissue surface during laser irradiation. (Right top inset) Formation of a hollow crater during irradiation.

6.3 Results

6.3.1 Total fluence

Using the elliptical beam dimensions of 0.06 x 0.08 cm at the tissue surface, scanned over a length of 1.1 cm, it is possible to estimate the total fluence (J/cm^2) delivered to the tissue by the reciprocating beam, for each incident power and irradiation time. An average uncompressed vessel

diameter of about 0.33 cm, and a typical 50% increase in vessel width with compression to 0.50 cm, yields a correction factor of (0.50 / 1.1), or 0.45 [14]. The rectangular beam area for the entire scan length is given by beam width (0.08 cm) times scan length (1.1 cm), or 0.088 cm². Hence, total fluence (F) delivered to the vessel for each laser power group and fluence level is:

$$F = \frac{[(0.45)(41 \text{ W})(20.5 \text{ s})]}{0.088 \text{ cm}^2} = 4298 \text{ J/cm}^2$$

$$F = \frac{[(0.45)(47 \text{ W})(16 \text{ s})]}{0.088 \text{ cm}^2} = 3845 \text{ J/cm}^2$$

$$F = \frac{[(0.45)(53 \text{ W})(10.5 \text{ s})]}{0.088 \text{ cm}^2} = 2846 \text{ J/cm}^2$$

$$F = \frac{[(0.45)(59 \text{ W})(5.5 \text{ s})]}{0.088 \text{ cm}^2} = 1659 \text{ J/cm}^2$$

This large difference in total fluence can be explained by the continual loss of heat through thermal conduction during the longer laser irradiation durations, thus requiring greater total fluence to achieve the temperatures needed for tissue ablation. Note that the thermal conduction of heat during laser irradiation is also desirable as it contributes to thermal sealing of the vessel.

6.3.2 Burst pressure (BP) measurements

Vessel burst pressures (mmHg) were conducted for all vessels sealed and bisected (n=40) at four different laser incident power levels and irradiation times. All vessel cut ends tested (80/80) withstood BPs above three times systolic pressure (360 mmHg), yielding a 100% success rate. The shortest irradiation time was 5-6 s at 59 W. The BP data is summarized in Table 6.1.

Representative images of a blood vessel sample before and after bisection are shown in Figure 6.3AB. Laser irradiation times shorter than 5 s resulted in tissue cutting, but not sealing, due to insufficient thermal conduction and thermal spread during the laser treatment time. Laser incident powers less than 41 W failed to produce a full-thickness cut, due to insufficient irradiance.

Otherwise, there was a strong linear fit to the power/time data points, demonstrating that higher laser incident power enables shorter laser irradiation times, as expected (Figure 6.3C).

Table 6.1: Burst pressures (BP) of both bisected segments (S1/S2) of blood vessels for each incident power and irradiation time.

Incident Laser Power (W)	Irradiation Time (s)	Mean BP (mmHg)
41	20 - 21	S1: 788 ± 374 / S2: 758 ± 320
47	15 - 17	S1: 1046 ± 355 / S2: 1053 ± 320
53	10 - 11	S1: 1199 ± 149 / S2: 875 ± 421
59	5 - 6	S1: 984 ± 351 / S2: 976 ± 350

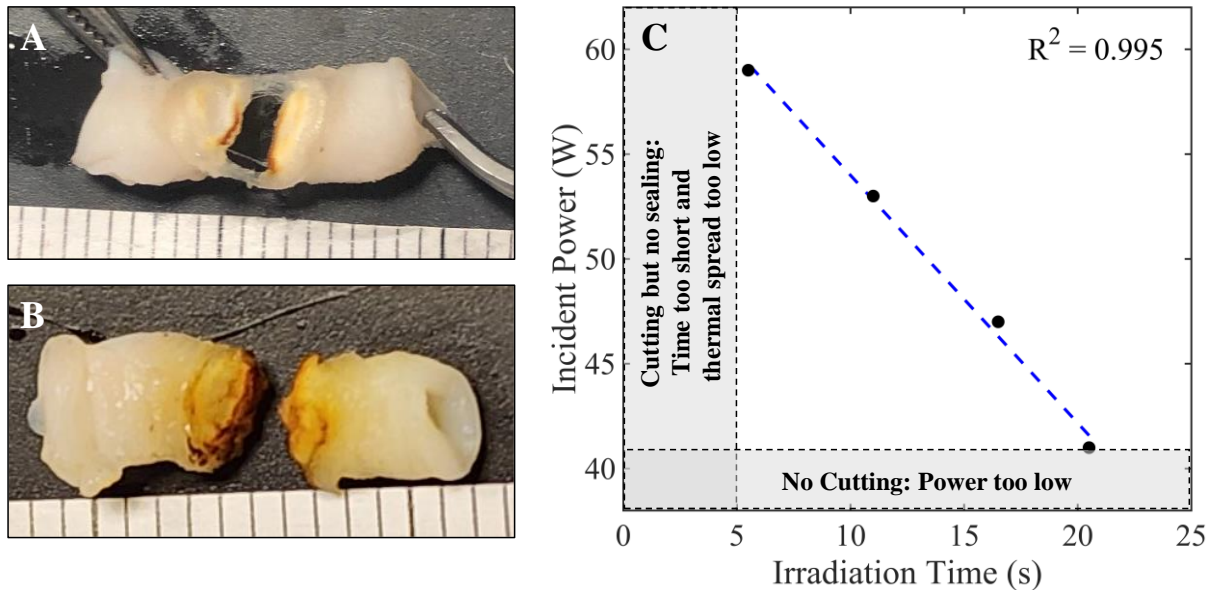


Figure 6.3: (A) Photograph of a vessel after bisection using 59 W for 5 s. A fascia layer is visible and the vessel was easily detached by pulling uniformly from both sides. ($d = 3.2$ mm, BP1: 460 mmHg, BP2: 776 mmHg). (B) Photograph of a vessel after bisection using 59 W for 6 s. A clean cut is shown ($d = 3.5$ mm, BP1: 1160 mmHg, BP2: 372 mmHg). (C) Comparison of laser incident power and irradiation times for each data set. Laser irradiation times shorter than 5 s resulted in tissue cutting, but not sealing, presumably due to insufficient thermal conduction and thermal spread during the laser treatment time. Laser incident powers less than 41 W failed to produce a full-thickness cut, due to insufficient irradiance.

6.3.3 Thermal characterization of quartz jaw

Temperature-time data for micro-thermocouples placed on the external (T_{out}) and internal (T_{in}) surfaces of the quartz chamber was also collected using the shortest irradiation time of 5-6 s and incident power of 59 W. The maximum temperature measured on the internal chamber surface, 77 °C, was lower than on the external surface, 103 °C. Cooling times for the external chamber surface are of interest, since they determine how long the surgeon must wait in between successive activations of the laparoscopic device. The external surface of the quartz chamber cooled to body temperature (37 °C) in 37 s.

6.3.4 Optical Transmission Signal during Blood Vessel Ablation

Optical transmission measurements revealed two distinct phases (Figure 6.4). Phase A is the period between the start of CW laser irradiation, with corresponding dehydration and coagulation of the tissue, and the beginning of carbon formation on the vessel surface. Analysis of the videos showed that the tissue surface discolored due to shrinkage from water evaporation and thermal denaturation. During phase B, tissue carbonization begins to form and grow in size. A rapid increase in optical transmission and eventual saturation of the signal occurs, as the tissue is vaporized and a full-thickness ablation crater forms. The laser was de-activated when the signal saturated. This steep and rapid rise in signal at the photodetector, corresponding to tissue perforation, may serve as a potential optical feedback system during laser bisection of vessels. Appendix A also provides calculations for the ablation velocity, based on these experiments.

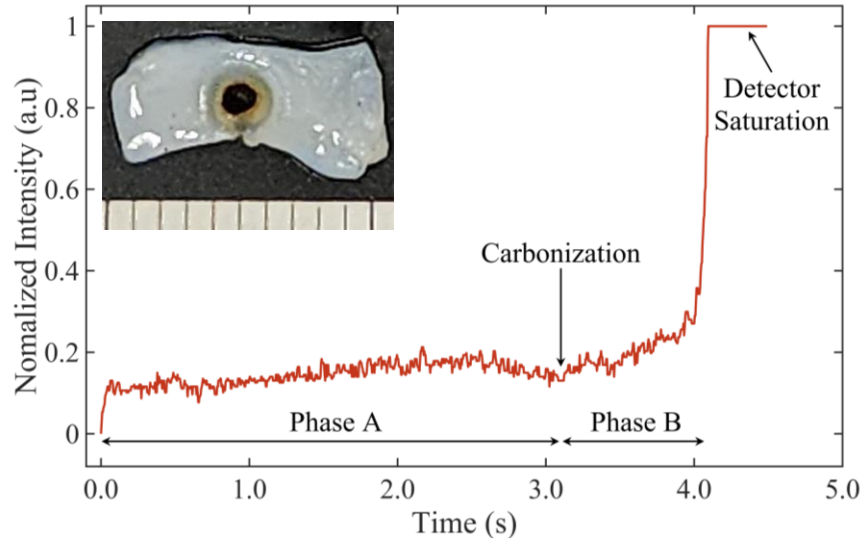


Figure 6.4: Optical transmission signal as a function of time during CW laser tissue ablation and (inset) the representative tissue sample ($d = 3.2$ mm).

6.4 Discussion

6.4.1 Vessel sealing and bisection studies

Previous benchtop studies were performed on a large scale, with bulk optical components unsuitable for integration into standard laparoscopic devices. These previous studies also utilized a two-step process with sequential sealing and then cutting of the vessel, involving a more complex method of translation of the optical components to change the beam focus and laser spot size [30]. This study investigated the feasibility of simultaneous IR laser vessel sealing and bisection of porcine renal arteries in a one-step approach, using a compact quartz optical chamber suitable for integration into the distal end effector jaws of standard 5-mm-OD laparoscopic devices.

It should be noted that previous computer simulations of the laser irradiation distribution through the quartz chamber (chapter 5), showing a Gaussian-like beam profile, with additional steps on the wings, motivated this approach to simultaneous sealing and bisection of vessels, based on the ability to coagulate and seal at the periphery of the beam and ablate or cut in the center of the beam (Figure 6.5). As observed in chapters 4 and 5, laboratory studies also demonstrated

successful sealing of blood vessels at 30 W for 5 s at 1470 nm. These parameters were therefore chosen as a baseline, and the laser power was elevated in steps with different irradiation times, and BPs were measured to confirm success.

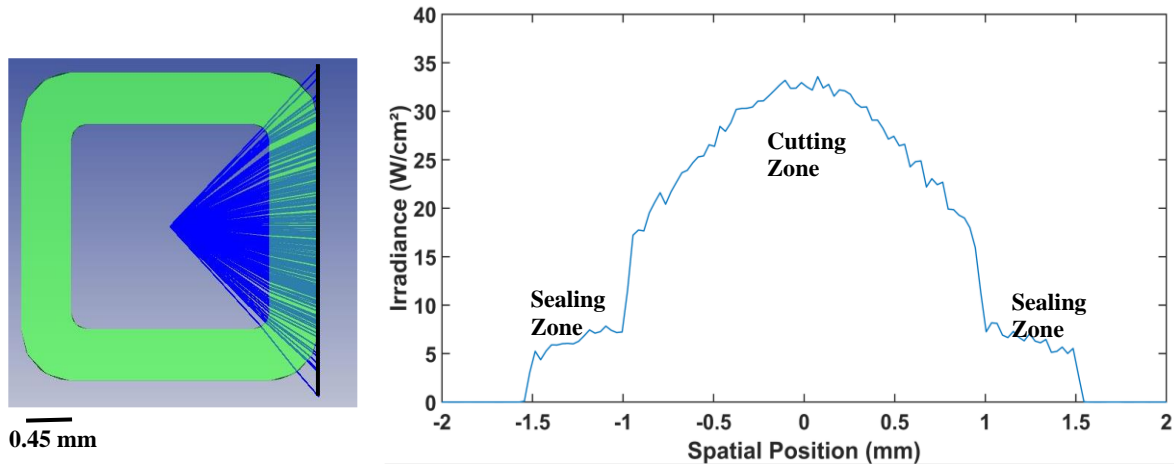


Figure 6.5: Ray tracing showing beam divergence through the quartz chamber and (right column) output beam profile, using Zemax optical software. The location of the detector surface in the simulations is denoted by a vertical black line on the right edge of each optical chamber.

Table 6.1 shows the shortest irradiation times required at each power level to simultaneously seal and bisect the vessel. It should be noted that the irradiation times contain a small range rather than a singular value due to several factors, including variable amount of fat and water content in vessels, different amounts of collagen/elastin levels (C/E ratio) and variable vessel sizes. Larger blood vessels had thicker walls which made it more difficult for the chamber to create equal pressure across the vessel and to efficiently compress it to the desired 0.4 mm thickness to match the optical penetration depth of the 1470-nm laser energy in tissue. These factors also explain in part the large range of BPs measured in Table 6.1.

In this study, the lowest laser irradiation time in each range provided a complete cut, but with a small amount of fascia remaining, easily manually pulled apart with tweezers in the laboratory or the device jaws in a clinical situation (Figure 6.3A). The highest irradiation time within each range provided a complete cut with no remaining fascia strands (Figure 6.3B).

The highest incident power, 59 W, yielded treatment times of 5-6 s, comparable to conventional RF and US devices. For example, a recent study reported energy activation durations of 7.7 s and 7.9 s for US and RF devices, respectively [67].

Peak temperatures and cooling times for the external surface of the chamber are also important, since they determine the safety profile of the device as well as the time the surgeon must wait between successive activations of the laparoscopic device. Peak temperatures measured 103 °C on the outside of the quartz jaw at 59 W and 5-6 s. Furthermore, the external surface of the chamber cooled to body temperature (37 °C) in 37 s. These values also appear promising, when directly compared with values reported for conventional RF and US devices. For example, a recent study reported that median external jaw temperatures were 126 °C for RF devices and 218 °C for US devices [67]. The quartz chamber's cooling time of 37 s also compares favorably with reported mean cooling times of 54 s and 68 s for two different RF devices [68].

One of the limitations in this study was the lack of a fully functional, upper hinged jaw on the device (Figure 6.5). A simple transparent optical window was used instead for compressing the tissue, and crudely simulating the optical and thermal properties of a transparent upper jaw. However, both jaws will be transparent in a final design, so this simple approach is still relevant for the optical and thermal studies. Moreover, the reciprocating fiber scan length and speed were kept constant in this preliminary study, for simplicity, and to prove feasibility of the simultaneous IR laser sealing and cutting technique. Although the parameters programmed were practical and similar to those used in previous studies in chapter 4 and 5, a future goal is to customize scan length to match the compressed vessel width. This approach will ensure that excess laser energy is not transmitted around the sample, which is not only inefficient, but may also potentially result

in safety issues due to higher device jaw temperatures. More efficient, custom scan lengths may also further lower device temperatures and cooling times, as well as laser treatment times.

6.4.2 Optical signal transmission studies

This study also demonstrated the feasibility of using the optical transmittance signal during IR laser tissue ablation as a closed-loop, optical feedback system for immediately deactivating the laser upon successful bisection. Optical transmission analysis during the ablation study revealed slightly variable pre-ablation times (Phase A), due to differences in tissue size, fat content, water content and C/E levels between samples. Consequently, an optical feedback system that deactivates the laser upon ablation is desired. Phase A in Figure 6.4 includes the phenomena of water absorbing laser light, followed by its evaporation and tissue coagulation, which results in the decrease of signal right before the start of phase B. This decrease is associated with a rise in the scattering coefficient of the tissue surface due to thermal coagulation.

Phase B starts with carbonization and ends when the tissue ablation is complete. The start of tissue carbonization was observed as a thin layer of blackened tissue at the surface (Figure 6.2 inset). Carbonization enhances light absorption, leading to a reduction in light transmission. Nevertheless, the creation of carbonized tissue did not lead to a reduction in transmission in the forward direction. Video frames displayed a progression where initially, a limited central area of carbonized tissue was generated. This area then transformed into a growing ring, producing an ablation hole in the tissue center.

Based on these observations, we hypothesize that upon carbonization, the tissue rapidly vaporized, forming a small ablation hole because of significantly increased absorption. As the carbonized zone expanded outward in the form of a growing ring, the hole diameter increased (Figure 6.2). This sequence of events could potentially explain the absence of any observed

decline in light transmission, as reported in previous studies [82]. Consequently, when the tissue is completely vaporized and the hole is complete, the signal saturates, and the laser can be deactivated (Figure 6.4).

6.5 Conclusion

Simultaneous IR sealing and bisection of blood vessels was conducted using a square quartz optical chamber (2.7 x 2.7 x 25 mm outer dimensions) that can be integrated into a standard 5-mm-OD laparoscopic device. The shortest irradiation time was 5-6 s using 59 W of laser power. Peak temperatures on the external chamber surface measured 103 °C, with a time of 37 s to cool to body temperature. Optical transmission measurements showed a rapid increase and saturation of the photodetector signal upon tissue ablation, which could potentially be used as an optical feedback system to confirm vessel bisection during the procedure. A depiction of the proposed laparoscopic prototype, showcasing the transparent quartz optical chamber employed in this study, was presented. Future work will involve design and construction of a complete prototype device for use during *in vivo* studies.

Chapter 7 : FUTURE WORK

7.1 Closed loop feedback and prototype design

The optical transmission signal has proven effective as an optical feedback method in vessel sealing and bisection, indicating the potential for developing a closed-loop system for in vivo studies. In the future, a closed loop system will be further developed and investigated to immediately deactivate the laser upon successful sealing and bisection of vessels. The development of such a system is motivated by several factors. First, implementation of an automated optical feedback system will save valuable operating room time in two ways, one by shortening the laser irradiation time, but also by reducing the cooling time needed in between successive applications as well. Lower peak temperatures in the tissue will also in turn provide an improved safety profile for the device, so accidental contact with adjacent tissue is less likely to result in a burn or undesirable collateral thermal damage.

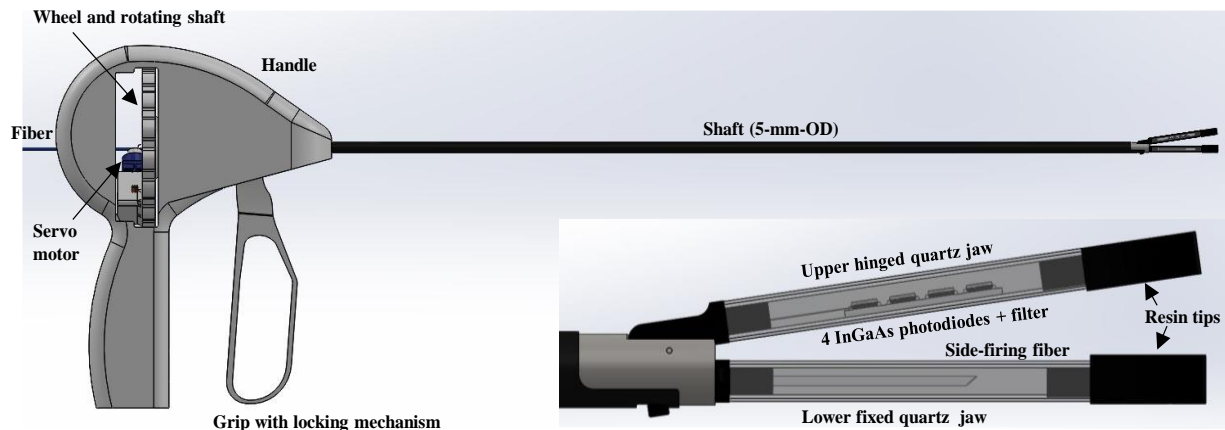


Figure 7.1: Diagram of the proposed laparoscopic device with quartz jaws and optical feedback system. The therapeutic, reciprocating, side-firing, optical fiber is housed in the bottom fixed jaw, while a linear array of four photodiodes and a neutral density filter for diagnostic feedback, is housed in the upper, hinged, active jaw.

Figure 7.1 shows a diagram of a proposed prototype laparoscopic device integrating the transparent quartz optical chamber used in these studies. The upper, movable jaw pivots on a hinge, and is used to compress the vessel. The incorporation of a transparent quartz chamber may enable the addition of photodiodes (PD), for measuring the optical transmission signal and providing optical diagnostic feedback. The quantity of PDs implemented should encompass the complete fiber scan length to ensure vessel bisection. To protect the photodiodes from excessive laser light, an absorptive neutral density filter may be employed. The bottom, fixed jaw provides therapeutic IR laser delivery, also with a transparent quartz chamber housing the reciprocating, side-firing, optical fiber for vessel sealing/bisection. Future efforts will involve construction of functional laparoscopic quartz jaw prototype for clinical *in vivo* studies.

7.2 Jaw cooling

A mechanism will be explored to use a cooling agent inside the laparoscopic jaw during the irradiation to decrease the maximum temperature and cooling time even further. Carbon dioxide (CO₂) can be used for this purpose due to its unique thermodynamic properties. By pressurizing CO₂, it can transition between its gas and liquid states at relatively low temperatures, which is crucial for its application in this context. This property allows CO₂ to absorb heat from its surroundings as it evaporates, thereby cooling the area. This process, known as the transcritical cycle, is a key principle behind the effectiveness of CO₂ in refrigeration and air conditioning systems. One of the key advantages of using CO₂ in this application is its low environmental impact compared to traditional refrigerants. It has a zero ODP (ozone depleting potential) and a GWP (global warming potential) of one (CO₂ is the fluid used for comparison when evaluating the greenhouse effect), making it a more environmentally friendly choice. Furthermore, the colorless, inexpensive, and nonflammable characteristics of CO₂ render it advantageous for this

application, as it ensures minimal distortion in the field of view, facilitates ready availability, and mitigates any potential security risks. [83].

In conclusion, exploring the use of CO₂ as a cooling agent inside the laparoscopic jaw during irradiation could lead to significant improvements in safety, efficiency, and environmental impact. This innovative approach demonstrates the potential for leveraging unique thermodynamic properties of CO₂ in laparoscopic procedures.

7.3 Optical indicator for collagen-elastin content and its relation to burst pressure strength

Burst pressure tests are commonly performed to measure the strength of a vessel seal. Deviations in burst pressure strength can be ascribed to differences in vessel diameter. An additional factor affecting the strength of vessel seals may be intrinsic to the vessels themselves. For example, distensibility of the vessel and response of the vessel wall to arterial pressure waves may transduce different forces to the seal. Independent of seal quality, force response of the vessel wall can lead to inconsistency in burst pressure required for seal failure. As such, distensibility/elasticity of the vessel wall may be an important factor in determining ultimate success of the specific vessel seal. However, there is an absence of methodology to measure elasticity and distensibility of vessels directly in patients. Hence, vessel diameter has been used as the best indirect predictor of vessel seal success. Most vessel-sealing systems have guidelines to prevent their use on vessels over a certain size. However, failures of these devices are observed even when used on vessels well within the size limitation. For example, very few vessels larger than 5–6 mm are routinely sealed using vessel-sealing devices. Therefore, size may not be the best predictor of vessel-sealing success because it does not take the intrinsic vessel elasticity and distensibility into account [84-85].

Blood vessel elasticity/distensibility is intrinsically dependent on vessel wall structure. While the vessel wall comprises various components, collagen and elastin represent key factors in determining blood vessel elasticity. Collagen represents a more rigid structural protein whereas elastin is more flexible. The relative ratio of these two components thus plays a central role in determining blood vessel wall rigidity/elasticity. Thus, the composition of the vessel wall with varying levels of collagen and elastin may, in turn, determine the strength of the seal itself. A few previous studies have reported the use of collagen-elastin ratio (C/E) to predict burst pressure of arterial seals. Arteries with the highest collagen–elastin (C/E) ratio consistently demonstrated significantly higher burst pressures than those arteries with lower C/E ratios, independent of artery diameter.

However, the procedure to measure the C/E ratio is time consuming and expensive. There is currently no real-time optical method. All studies that related C/E ratio with burst pressure strength used a biochemical method to find the collagen-elastin content. However, fluorescence of collagen and elastin, can be used to measure the C/E ratio of the artery. Fluorescence of collagen and elastin was explained in detail in chapter 4. In the future, the fluorescent signal of the sealed vessel will be obtained with the set up shown in Figure 4.2B. The collagen-elastin content and the ratio will be determined using the biochemical method and then the same samples will be correlated to their fluorescence signal. In the biochemical method, following vessel sealing and burst pressure measurements, arteries will be snap-frozen in liquid nitrogen and stored at -80°C . Upon thawing to room temperature, wet weight (ww) will be determined, and the vessel will be divided equally for collagen and elastin analysis. Total collagen will be assessed via tissue hydroxyproline content, following hydrolysis in 6 N HCl, drying, and resuspension. Chloramine and p-Dimethylaminobenzaldehyde (DMBA) solutions will be added to determine hydroxyproline

content, with collagen calculated and expressed as total collagen/mg tissue (ww). Duplicate tissue samples will be used for each assay, with absorbance measured in triplicate [84-85]. It is proposed that fluorescent intensity will increase linearly with collagen-elastin content. Once the relation is established, the fluorescence signal obtained from the optical feedback method could be used to predict burst pressure strength of the seal as well.

Chapter 8 : CONCLUSION

The field of surgical instrumentation has seen remarkable advancements in recent years, particularly in the realm of energy-based devices for blood vessel ligation. Conventional techniques like suture ligation, while effective, are time-consuming and require a high level of skill. Alternative methods utilizing mechanical clips or sutures, though faster, leave foreign objects in the body and disrupt the surgical process by necessitating instrument exchanges. Energy-based devices, such as ultrasonic and radiofrequency technologies, have revolutionized surgical procedures by offering rapid and efficient vessel ligation. However, these devices have limitations, including large thermal damage zones, which restrict their use in delicate procedures performed in confined spaces. The need for quicker cooling times between procedures and the risk of thermal damage to healthy tissue further add to these limitations.

To address these issues, a novel alternative method using near-infrared (IR) lasers for vessel ligation was proposed. The study explored two real-time optical feedback systems along with transparent jaw designs for sealing and bisection of blood vessels. The use of tissue autofluorescence as a real-time optical feedback system showed promising results. The fluorescence signal increased significantly for successful seals compared to failed ones, indicating its potential for use as a feedback mechanism.

Furthermore, the study compared quartz and sapphire materials for use in the optical chamber of the laparoscopic device jaw. Quartz emerged as the superior choice, demonstrating lower Fresnel reflections, lower internal temperatures, and shorter cooling times compared to sapphire. These results suggest that the use of a transparent chamber, particularly one made of

quartz, can improve visibility and enable more accurate visualization and placement of vessels within the device jaws.

The simultaneous IR laser vessel sealing and bisection study using a quartz optical chamber showed promising results. The short irradiation times and rapid cooling to body temperature demonstrate the potential of this approach for use in minimally invasive surgical procedures. Moreover, optical transmission measurements showed a rapid increase and saturation of the photodetector signal upon tissue ablation, which could potentially be used as an optical feedback system to confirm vessel bisection during the procedure. The integration of the quartz chamber into a standard laparoscopic device opens up possibilities for further preclinical studies and eventual clinical applications.

In conclusion, the research presented in this thesis represents a significant step forward in the field of surgical instrumentation. The use of near-infrared lasers for vessel ligation, coupled with real-time optical feedback systems and transparent chamber designs, holds great promise for improving the efficiency and safety of surgical procedures.

Future work will focus on design and construction of a complete prototype device and conducting *in vivo* studies to validate their effectiveness in clinical settings. Additionally, a study will be conducted to investigate the incorporation of a cooling agent within the transparent jaw to expedite the cooling process further. Optical transmission signal has demonstrated its viability as an optical feedback mechanism during vessel sealing and bisection; thus, a closed-loop system will be devised for *in vivo* studies. Furthermore, the capability of tissue fluorescence to measure the collagen-elastin ratio inside the vessel in real time will also be explored. This ratio could be compared to the fluorescence signal before and after sealing the vessel to explore the utilization of the collagen-elastin ratio as an indicator of burst pressure strength.

REFERENCES

1. N. S. Blencowe, R. Waldon, and M. N. Vipond, "Management of patients after laparoscopic procedures." *BMJ*, vol. 360, 2018, Art. no. k120.
2. Dutta, D. K., and Dutta, I., "The Harmonic Scalpel." *Journal of Obstetrics and Gynaecology of India*, 66(3), 209-10 (2016).
3. "Valleylab Ligasure Vessel Sealing System." Avante Health Solutions, avantehs.com/p/valleylab-ligasure-vessel-sealing-system/952.
4. Karande, Vishvanath C. "LigaSure™ 5-Mm Blunt Tip Laparoscopic Instrument." *J. Obstetrics and Gynecology of India*, 65(5), 350–352 (2015).
5. Risselada, M., Ellison, G. W., Bacon, N. J., Polyak, M. M., van Gilder, J., Kirkby, K., and Kim, S. E., "Comparison of 5 surgical techniques for partial liver lobectomy in the dog for intraoperative blood loss and surgical time." *Vet. Surg.* 39(7), 856-862 (2010).
6. Garancini, M., Gianotti, L., Mattavelli, I., Romano, F., Degrate, L., Caprotti, R., Nespoli, A., and Uggeri, F., "Bipolar vessel sealing system vs clamp crushing technique for liver parenchyma transaction." *Hepatogastroenterology* 58(105), 127-132 (2011).
7. Leonardo, C., Guaglianone, S., De Carli, P., Pompeo, V., Forastiere, E., and Gallucci, M., "Laparoscopic nephrectomy using Ligasure system: preliminary experience." *J. Endourol.* 19(8), 976-978 (2005).
8. Ettinger, J. E., Ramos, A. C., Azaro, E., Galvao-Neto, M. P., Mello, C. A., Galvao, M. S., Amaral, P. C., Carlo, A., and Fahel, E., "Staplerless laparoscopic gastric bypass: a new option in bariatric surgery." *Obes. Surg.* 16(5), 638-645 (2006).

9. Stoff, A., Reichenberger, M. A., and Richter, D. F., "Comparing the ultrasonically activated scalpel (Harmonic) with high-frequency electrocautery for postoperative serious drainage in massive weight loss surgery." *Plast. Reconstr. Surg.* 120(4), 1092-1093 (2007).
10. Brolin, R. E. and Cody, R. P., "Impact of technological advances on complications of revisional bariatric operations." *J. Am. Coll. Surg.* 206(3), 1137-1144 (2008).
11. Kurt, Y., Yucel, E., Filiz, A. I., Sucullu, I., and Akin, M. A., "New energy-based devices in laparoscopic splenectomy: comparison of Ligasure alone versus Ligasure and Ultracision together." *Surgical Practice* 16(1), 28-32 (2012).
12. Shabadong, H., Maddah, G., Tavassoli, A., Jangjoo, A., Alvandipour, M., Abdollahi, A., and Noorshafiee, S., "Laparoscopic splenectomy: ligasure or clip ligation?" *Surg. Laparosc. Endosc. Percutan. Tech.* 22(2), 136-138 (2012).
13. Smith, T. L. and Smith, J. M., "Electrosurgery in otolaryngology-head and neck surgery: principles, advances, and complications." *Laryngoscope* 111(5), 769-780 (2001).
14. Lepner, U. and Vaasna, T., "Ligasure vessel sealing system versus conventional vessel ligation in thyroidectomy." *Scand. J. Surg.* 96(1), 31-34 (2007).
15. Pons, Y., Gauthier, J., Ukkola-Pons, E., Clement, P., Roguet, E., Poncet, J. L., and Conessa, C., "Comparison of LigaSure vessel sealing system, harmonic scalpel, and conventional hemostasis in total thyroidectomy." *Otolaryngol. Head Neck Surg.* 141(4), 496-501 (2009).
16. Prokopakis, E. P., Lachanas, V. A., Vardouniotis, A. S., and Velegrakis, G. A., "The use of the Ligasure vessel sealing system in head and neck surgery: a report on six years of experience and a review of the literature." *B-ENT* 6(1), 19-25 (2010).

17. Zarebczan, B., Mohanty, D., and Chen, H., "A comparison of the Ligasure and harmonic scalpel in thyroid surgery: a single institution review." *Ann. Surg. Oncol.* 18(1), 214-218 (2011).
18. O'Neill, C. J., Chang, L. Y., Suliburk, J. W., Sidhu, S. B., Delbridge, L. W., and Sywak, M. S., "Sutureless thyroidectomy: surgical technique." *ANZ J. Surg.* 81(7-8), 515-518 (2011).
19. Kroft, J. and Selk, A., "Energy-based vessel sealing in vaginal hysterectomy: a systematic review and meta-analysis." *Obstet. Gynecol.* 118(5), 1127-1136 (2011).
20. Msilka, S., Deroide G, Kianmanesh R, Iannelli A, Hay J. M., Fingerhut A, and Flamant, Y., "Harmonic scalpel in laparoscopic colorectal surgery." *Dis. Colon. Rectum* 44(3), 432-436 (2001).
21. Rimonda, R., Arezzo, A., Garrone, C., Allaix, M. E., Giraudo, G., and Morino, M., "Electrothermal bipolar vessel sealing system vs. harmonic scalpel in colorectal laparoscopic surgery; a prospective, randomized study." *Dis. Colon. Rectum* 52(4), 657-661 (2009).
22. Adamina, M., Champagne, B. J., Hoffman, L., Ermlich, M. B., and Delaney, C. P., "Randomized clinical trial comparing the cost and effectiveness of bipolar vessel sealers versus clips and vascular staplers for laparoscopic colorectal resection." *Br. J. Surg.* 98(12), 1703-1712 (2011).
23. Tou, S., Malik, A. I., Wexner, S. D., and Nelson, R. L., "Energy source instruments for laparoscopic colectomy." *Cochrane Database Syst. Rev.* 11(5), (2011).
24. Hruby, G. W., Marrufo, F. C., Durak, E., Collins, S. M., Pierorazio, P., Humphrey, P. A., Mansukhani, M. M., and Landman, J., "Evaluation of surgical energy devices for vessel sealing and peripheral energy spread in a porcine model." *J. Urol.* 178(6), 2689-2693 (2007).

25. Lamberton, G. R., His, R. S., Jin, D. H., Lindler, T. U., Jellison, F. C., and Baldwin, D. D., "Prospective comparison of four laparoscopic vessel ligation devices." *J. Endourol.* 22(10), 2307-2312 (2008).
26. Sutton, P. A., Awad, S., Perkins, A. C., and Lobo, D. N., "Comparison of lateral thermal spread using monopolar and bipolar diathermy, the Harmonic scalpel, and the Ligasure." *Br. J. Surg.* 97(3), 428-433 (2010).
27. R. Tanaka et al., "Evaluation of Vessel Sealing Performance Among Ultrasonic Devices in a Porcine Model." *Surgical Innovation.* 22(4), 338-343 (2015).
28. Szyrach MN, Paschenda P, Afify M, Schaller D, Tolba RH "Evaluation of the novel bipolar vessel sealing and cutting device BiCision(R) in a porcine model." *Minim Invasive Ther Allied Technol* 21 402-407 (2012).
29. Leppäniemi, Ari, et al. "Arterial and Venous Repair with Vascular Clips: Comparison with Suture Closure." *Journal of Vascular Surgery*, 26(1), 24-28 (1997).
30. Giglio N.C., Hutchens TC, Perkins WC, Latimer C, Ward A, Nau WH, Fried NM. "Rapid sealing and cutting of porcine blood vessels, ex vivo, using a high power, 1470-nm diode laser." *J Biomed Opt*, (2014).
31. Sing, R. F., et al. "Comparison of Ultrasonic Energy, Bipolar Thermal Energy, and Vascular Clips for the Hemostasis of Small-, Medium-, and Large-Sized Arteries." *Surgical Endoscopy*, 17(8) 1228-1230 (2003).
32. C. M. Cilip et al., "Infrared laser thermal fusion of blood vessels: preliminary ex vivo tissue studies." *J. Biomed. Opt.* 18(5), 058001 (2013).
33. N. C. Giglio et al., "Rapid sealing and cutting of porcine blood vessels, ex vivo, using a high power, 1470-nm diode laser." *J. Biomed. Opt.* 19(3), 038002 (2014).

34. C. M. Cilip et al., "Infrared laser sealing of porcine vascular tissues using a 1470 nm diode laser: preliminary in vivo studies." *Lasers Surg. Med.* 49(4), 366–371 (2017).
35. Giglio, N. C., and Fried N. M., "Real-time, nondestructive optical feedback systems for infrared laser sealing of blood vessels." *Diagnostic and Therapeutic Applications of Light in Cardiology* (2022).
36. Hale, G. M. and Querry, M. R., "Optical constants of water in the 200 nm to 200 μ m wavelength region." *Appl. Opt.* 12, 555-563 (1973).
37. Wang, Ruikang K. "Modelling optical properties of soft tissue by fractal distribution of scatterers." *Journal of Modern Optics*, 47(1) 103-120 (2000).
38. Ash, Caerwyn, et al. "Effect of wavelength and beam width on penetration in light-tissue interaction using comp. methods." *Lasers in Medical Science*, 32(8), 1909-1918 (2017).
39. M. A. Ansari, M. Erfanzadeh, and E. Mohajerani, "Mechanisms of laser-tissue interaction: II. Tissue thermal properties." *J. Laser Med. Sci.* 4, 99–106 (2013).
40. Rustagi, S. et al. "Intercranial human vertebral artery: A histomorphology study" *International journal of current research and review.* IJCRR 5(12), 89-90 (2013).
41. Hope, W. W., Padma, S., Newcomb, W. L., Schmelzer, T. M., Heath, J. J., Lincourt, A. E., Heniford, B. T., Norton, H. J., Martinie, J. B., and Iannitti, D. A., "An evaluation of electrosurgical vessel-sealing devices in biliary tract surgery in a porcine model." *HPB* 12(10), 703-708 (2010).
42. Newcomb, W. L., Hope, W. W., Schmelzer, T. M., Heath, J. J., Norton, H. J., Lincourt, A. E., Heniford, B. T., and Iannitti, D. A., "Comparison of blood vessel sealing among new electrosurgical and ultrasonic devices." *Surg. Endosc.* 23, 90-96 (2009).

43. Sherman, Irwin W., and Vilia G. Sherman. *Biology: A Human Approach*. New York: Oxford UP, Print (1979).
44. J. S. Kennedy, P. L. Stranahan, K. D. Taylor, and J. G. Chandler, "Highburst-strength, feedback-controlled bipolar vessel sealing." *Surg. Endosc.*, vol. 12, no. 6, pp. 876–878 (1998).
45. N. Shigemura, A. Akashi, T. Nakagiri, M. Ohta, and H. Matsuda, "A new tissue-sealing technique using ligasure system for nonanatomical pulmonary resection: Preliminary results of sutureless and stapleless thoracoscopic surgery." *Ann. Thorac. Surg.*, vol. 77, no. 4, pp. 1415–1418 (2004).
46. R. Patrone et al., "The impact of the ultrasonic, bipolar and integrated energy devices in the adrenal gland surgery: Literature review and our experience." *BMC Surg.*, vol. 18, no. Suppl 1, Art. no. 123 (2019).
47. T. Floume, R. A. Syms, A. W. Darzi, and G. B. Hanna, "Real-time optical monitoring of radio-frequency tissue fusion by continuous wave transmission spectroscopy." *J. Biomed. Opt.*, vol. 13, no. 6, Art. no. 064006 (2008).
48. T. Floume, R. A. Syms, A. W. Darzi, and G. B. Hanna, "Optical, thermal, and electrical monitoring of radiofrequency tissue modification." *J. Biomed. Opt.*, vol. 15, no. 1, Art. no. 018003 (2021).
49. L. Su et al., "Laser-induced tissue fluorescence in radiofrequency tissue fusion characterization." *Proc. SPIE*, vol. 19, Art. no. 015007 (2014).
50. L. Su et al., "Raman spectroscopic evidence of tissue restructuring in heat-induced tissue fusion." *J. Biophotonics*, vol. 7, no. 9, pp. 713–723 (2014).

51. Alfano, R. R., “Advances in ultrafast time resolved fluorescence physics for cancer detection in optical biopsy.” *AIP Advances*, 2(1), 011103 (2012).
52. J. Tang, F. Zeng, H. Savage, P. P. Ho, and R. Alfano, “Fluorescence spectroscopic imaging to detect changes in collagen and elastin following laser tissue welding.” *J. Clin. Laser Med. Surg.*, vol. 18, no. 1, 1-8 (2000).
53. L. A. Hardy et al., “Rapid sealing of porcine renal vessels, ex vivo, using a high power, 1470-nm laser, and laparoscopic prototype.” *J. Biomed. Opt.*, vol. 22, no. 5, Art. no. 058002 (2017).
54. N. C. Giglio, H. M. Grose, and N. M. Fried, “Comparison of fiber optic linear beam shaping designs for laparoscopic laser sealing of vascular tissues.” *Opt. Eng.*, vol. 61, no. 2, Art. no. 026112 (2022).
55. G. R. Lamberton et al., “Prospective comparison of four laparoscopic vessel ligation devices.” *J. Endourol.*, vol. 22, no. 10, pp. 2307–2312 (2008).
56. M. N. Szyrach, P. Paschenda, M. Afify, D. Schaller, and R. H. Tolba, “Evaluation of the novel bipolar vessel sealing and cutting device BiCision(R) in a porcine model.” *Minim. Invasive Ther. Allied Technol.*, vol. 21, no. 6, pp. 402–407 (2012).
57. R. Tanaka et al., “Evaluation of vessel sealing performance among ultrasonic devices in a porcine model.” *Surg. Innov.*, vol. 22, no. 4, pp. 338–343 (2015).
58. J. Tang, F. Zeng, H. Savage, P. P. Ho, and R. Alfano, “Fluorescence spectroscopic imaging to detect changes in collagen and elastin following laser tissue welding.” *J. Clin. Laser Med. Surg.*, vol. 18, no. 1, pp. 3–8 (2000).

59. I. Giovannacci et al., “Which are the main fluorophores in skin and oral mucosa? A review with emphasis on clinical applications of tissue autofluorescence.” *Arch. Oral Biol.*, vol. 105, pp. 89–98 (2019).
60. O. D. Smirnova, D. A. Rogatkin, and K. S. Litvinova, “Collagen as in vivo quantitative fluorescent biomarkers of abnormal tissue changes.” *J. Innov. Opt. Health Sci.*, vol. 5, no. 2, Art. no. 1250010 (2012).
61. Y. Wu and J. Y. Qu, “Autofluorescence spectroscopy of epithelial tissues.” *Proc. SPIE*, vol. 11, Art. no. 054023 (2006).
62. T. Damićanin and M. Damićanin, “Using fluorescence spectroscopy to diagnose breast cancer.” in *Applications of Molecular Spectroscopy to Current Research in the Chemical and Biological Sciences*, M. T. Stauffer, Ed. London, U.K.: IntechOpen (2016).
63. P. K. Gupta, S. K. Majumder, and A. Uppal, “Breast cancer diagnosis using N₂ laser excited autofluorescence spectroscopy.” *Lasers Surg. Med.*, vol. 21, no. 5, pp. 417–422 (1997).
64. Y. Sun et al., “Dynamic tissue analysis using time- and wavelength resolved fluorescence spectroscopy for atherosclerosis diagnosis.” *Opt. Exp.*, vol. 19, no. 5, pp. 3890–3901 (2011).
65. R. R. Alfano, “Advances in ultrafast time resolved fluorescence physics for cancer detection in optical biopsy.” *AIP Adv.*, vol. 2, no. 1, Art. no. 011103 (2012).
66. N. C. Giglio and N. M. Fried, “Computational simulations for infrared laser sealing and cutting of blood vessels.” *IEEE J. Sel. Top. Quantum Electron.*, vol. 27, no. 4, Jul./Aug., Art. no. 7200608 (2021).
67. L. Brecht et al., “Implementation of a novel efficacy score to compare sealing and cutting devices in a porcine model.” *Surg. Endosc.*, vol. 32, no. 2, pp. 1002–1011 (2017).

68. C. I. Jimenez, A. Leith, and F. Ringold, “Novel multifunctional robotically assisted bipolar instrument for simultaneous radiofrequency sealing and transection: Preclinical and single center experience.” *BMC Surg.*, vol. 22, no. 1, pp. 1–8 (2022).
69. A. M. Ong et al., “Nerve sparing radical prostatectomy: Effects of hemostatic energy sources on the recovery of cavernous nerve function in a canine model.” *J. Urol.*, vol. 172, no. 4, pp. 1318–1322 (2004).
70. Saeed WM, Fried NM., “A real-time fluorescence feedback system for infrared laser sealing of blood vessels.” *IEEE J Sel Top Quantum Electron.* 29(4):1–7 (2023).
71. The book on the technologies of polymicro; 2011.
72. Yang ST, Matthews MJ, Elhadj S, Cooke D, Guss GM, Draggoo VG, et al., “Comparing the use of mid-infrared versus far-infrared lasers for mitigating damage growth on fused silica.” *Appl Opt.* 2010;49(14):2606–16.
73. Harrington JA. *Infrared fibers and their applications*. Bellingham, WA: SPIE Press; 2004.
74. Busse LE, Florea CM, Frantz JA, Shaw LB, Aggarwal ID, Poutous MK, et al., “Anti-reflective surface structures for spinel ceramics and fused silica windows, lenses and optical fibers.” *Opt Mater Express.* 4(12):2504–15 (2014).
75. Busse LE, Frantz JA, Shaw LB, Poutous MK, Aggarwal ID, Sanghera JS., “Antireflective surface microstructures on optics for laser applications.” *CLEO OSA Tech Digest, SM2M.* 1:1–2 (2016).
76. Taylor CD, Busse LE, Frantz J, Sanghera JS, Aggarwal ID, Poutous MK., “Angle-of-incidence performance of random anti- reflection structures on curved surfaces.” *Appl Opt.* 55: 2203–13 (2016).

77. Phillips CK, Hruby GW, Durak E, Lehman DS, Humphrey PA, Mansukhani MM, et al., "Tissue response to surgical energy devices." *Urology*. 71(4):744–8 (2008).
78. Kim FJ, Chammas Jr., MF, Gewehr E, Morihisa M, Caldas F, Hayacibara E, et al., "Temperature safety profile of laparoscopic devices: harmonic ACE (ACE), ligasure V (LV), and plasma trisector (PT)." *Surg Endosc*. 22(6):1464–9 (2008).
79. Govekar HR, Robinson TN, Stiegmann GV, McGreevy FT., "Residual heat of laparoscopic energy devices: how long must the surgeon wait to touch additional tissue?" *Surg Endosc*. 25(11): 3499–502 (2011).
80. Brecht L, Wallwiener M, Schott S, Domschke C, Dinkic C, Golatta M, et al., "Implementation of a novel efficacy score to compare sealing and cutting devices in a porcine model." *Surg Endosc*. 32(2):1002–11 (2017).
81. Jimenez CI, Lath A, Ringold F., "Novel multifunctional robotically assisted bipolar instrument for simultaneous radiofrequency sealing and transection: preclinical and single center experience." *BMC Surg*. 22(1):37 (2022).
82. Verdaasdonk RM, Borst C, van Gemert MJC, "Explosive onset of continuous wave laser tissue ablation." *Phys Med Biol* 35(8):1129-1144 (1990)
83. Intersam, "CO₂ as a Cooling System." *Intersam*, 21 Oct. 2020, intersam.es/en/co2/. Accessed 10 Mar. 2024.
84. D. Sindram et al., "Collagen-elastin ratio predicts burst pressure of arterial seals created using a bipolar vessel sealing device in a porcine model." *Surg. Endosc.*, vol. 25, no. 8, 2604–2612, (2011).

85. C. A. Latimer, M. Nelson, C. M. Moore, and K. E. Martin, "Effect of collagen and elastin content on the burst pressure of human blood vessel seals formed with a bipolar tissue sealing system." *J. Surg. Res.*, vol. 186, no. 1, 73–80, (2014).

APPENDIX A : PEER REVIEWED JOURNAL ARTICLES

1. **Woheeb M. Saeed**, and Nathaniel M. Fried, “A Real-Time Fluorescence Feedback System for Infrared Laser Sealing of Blood Vessels.” *IEEE Journal of Selected Topics in Quantum Electronics*, vol. 29, no. 4, 1–7, (2023).
2. **Woheeb M. Saeed**, PJ O’Brien, Jude Yoshino, Aiden R. Restelli, Alexandria J. Traynham, Nathaniel M. Fried, “Comparison of Quartz and Sapphire Optical Chambers for Infrared Laser Sealing of Vascular Tissues Using a Reciprocating, Side-Firing Optical Fiber: Simulations and Experiments.” *Lasers in Surgery and Medicine*, vol. 55, no. 10, pp. 886–899, (2023).
3. **Woheeb M. Saeed**, Jude Yoshino, Alexandria J. Traynham, Nathaniel M. Fried, “Simultaneous Sealing and Bisection of Porcine Renal Blood Vessels, Ex Vivo, using a Continuous-wave, Infrared Diode Laser at 1470 nm.” *Lasers in Medical Science*, Accepted.

APPENDIX B : PEER REVIEWED CONFERENCE PROCEEDINGS

1. **Woheeb M. Saeed**, and Nathaniel M. Fried, "Changes in Tissue Fluorescence during Infrared Laser Sealing of Blood Vessels." Diagnostic and Therapeutic Applications of Light in Cardiology, vol. 12355 (2023).
2. Patrick J. O'Brien, **Woheeb M. Saeed**, and N.M. Fried, "A Transparent Laparoscopic jaw Design for Infrared Laser Sealing of Vascular Tissues using a Reciprocating, Side-Firing Optical Fiber." Diagnostic and Therapeutic Applications of Light in Cardiology, vol. 12355 (2023).
3. Aiden R. Restelli, **Woheeb M. Saeed**, and N.M. Fried, "A Novel Flexible Ureteroscope Design Using a Saline Light Guide Channel for Combined Irrigation and Illumination." Advanced Photonics in Urology, vol. 12353 (2023).
4. **Woheeb M. Saeed**, Thomas C. Hutchens, and N. M. Fried, " Comparison of Surfactants for Enhancing Laser-Induced Vapor Bubble Dimensions." Advanced Photonics in Urology, vol. 12353, (2023).
5. **Woheeb M. Saeed**, PJ O'Brien, Jude Yoshino, Aiden R. Restelli, Alexandria J. Traynham, Nathaniel M. Fried, "Quartz versus Sapphire Optical Chambers for use in Infrared Laser Sealing of Blood Vessels." Proc. SPIE, (2024).
6. **Woheeb M. Saeed**, Jude Yoshino, Alexandria J. Traynham, Nathaniel M. Fried, "Simultaneous Infrared Laser Sealing and Cutting of Blood Vessels." Proc. SPIE, (2024).